



Chair of Design of Steels

Doctoral Thesis



Thermomechanical Fatigue Resistant
Dual Hardening Steels

Dipl.-Ing. Matthias Hofinger

May 2020

AFFIDAVIT

I declare on oath that I wrote this thesis independently, did not use other than the specified sources and aids, and did not otherwise use any unauthorized aids.

I declare that I have read, understood, and complied with the guidelines of the senate of the Montanuniversität Leoben for "Good Scientific Practice".

Furthermore, I declare that the electronic and printed version of the submitted thesis are identical, both, formally and with regard to content.

Date 30.04.2020

Signature Author
Hofinger Matthias

Expression of thanks

First and foremost, I want to thank Prof. Dr. mont Ronald Schnitzer, for the possibility to conduct this research and many fruitful discussions. You were always there if needed, no matter how tight your schedule, and always supportive and to be counted on.

I also want to thank Dr. mont Harald Leitner for mentoring my work, who was never shy of expressing critical views and thoughts which are vital for good research, and who provided me with a continuous flow of new ideas and tasks.

Many thanks belong to my colleagues from Böhler Edelstahl, Miloslav Ognianov and Christoph Turk. Turki and Stephanie Sackl I need to thank, for introducing me to the world of applied research at the Department and teaching me to never give up if your results just won't make any sense.

Special thanks I want to express to my research buddies, who helped guide and supported me through the last three years: Max Siller, Hans Kappacher, Candy Ebner and Christina Hofer. You I have to thank for many an invaluable discussion, almost as often on scientific problems as not, and great memories and moments I share with you. You have become friends, not just colleagues and I don't want to imagine my time at the Department without you.

Of course I have to mention the variety of my bureau colleagues and honored members of the Peter-Tunner soup club as well, above all Andreas Landefeld, Anna-Sophie Ebner and Severin Jakob, who helped provide a productive and fun work environment.

Thanks also belong to my colleague at the chair of mechanical engineering Stephan Seisenbacher, who conducted the thermomechanical fatigue tests this work relies on, and to "my" students Maximilian Staudacher, Armin Proyer and Amin Sakic, who performed much of the manual metallographic labour.

The last couple of years at Leoben would not have been the same without the great gaming nights and holidays I was able to share with my LeCiGa-club, Annemarie and Christian Saringer, Philipp Stögner, and Cornelia Tauchner. Although you are responsible for many sleepless nights and consequently very long and exhausting following workdays, I don't want to miss any of them.

Last I want to thank the person who carried me the most through this thesis, I can share my hopes and concerns with and always helps me keep a – at least slightly – positive attitude.
Conny

“Ein Buch muss die Axt sein für das gefrorene Meer in uns.“

Franz Kafka

Table of Contents

Part A

1	Kurzfassung.....	1
2	Abstract	4
3	Introduction.....	5
4	State of the Art	7
4.1	Pressure casting	7
4.2	Thermal fatigue	8
4.3	Precipitation reactions	11
4.3.1	Cluster formation	12
4.3.2	Homogeneous/ heterogeneous precipitation	12
4.3.3	Precipitate growth	12
4.3.4	Ostwald Ripening – LSW theory	13
4.3.5	Dissolution of precipitates	13
4.3.6	Influence of mechanical strain on precipitate behavior	14
4.4	Dual hardening steels	14
4.5	Characterization of precipitates.....	17
4.6	Relation of the current thesis to the state of the Art.....	19
5	Overview of publications.....	20
5.1	Appended papers	20
5.2	Co-authored papers related to this work.....	21
5.3	Conference contributions	21
5.4	Supervised theses	21
6	Experimental procedure	22
6.1	Steels investigated	22
6.2	Characterization of the nanostructure.....	23
7	Results and Discussion	24
7.1	Aim and scope of the investigations.....	24
7.2	Microstructural characterization.....	24
7.3	Characterization of precipitation reactions.....	29
7.4	Hot tensile tests	30
7.5	Thermomechanical fatigue testing	30
7.6	Impact of thermomechanical fatigue on the nanostructure	35
7.7	Thermodynamic Calculations.....	47
8	Outlook and open questions.....	49
9	Novel features.....	51
10	References.....	52

Part B

- Paper I** M. Hofinger, M. Staudacher, M. Ognianov, C. Turk, H. Leitner, R. Schnitzer
Microstructural evolution of a dual hardening steel during heat treatment
Micron 120 (2019) 48–56.
DOI: 10.1016/j.micron.2019.02.004
- Paper II** M. Hofinger, M. Ognianov, C. Turk, H. Leitner, R. Schnitzer
Early Stages of Precipitate Formation in a Dual Hardening Steel
Journal of Heat Treatment and Materials 74 (2019) 293–301.
DOI: 10.3139/105.110390
- Paper III** M. Hofinger, B. Seisenbacher, M. Ognianov, H. Leitner, C. Turk, M. Kapp, R. Schnitzer
Thermomechanical Fatigue Testing of Dual Hardening Tool Steels
steel research int. 3 (2019) 1900423.
DOI: 10.1002/srin.201900423
- Paper IV** M. Hofinger, C. Turk, M. Ognianov, H. Leitner, R. Schnitzer
Precipitation reactions in a Cu-Ni-Al medium carbon alloyed dual hardening steel
Materials Characterization 160 (2020) 110126.
DOI: 10.1016/j.matchar.2020.110126

List of Abbreviations

LCF	Low-cycle Fatigue
APT	Atom probe tomography
TEM	Transmission electron microscopy
(OP)-TMF	(Out-of-phase)-Thermomechanical fatigue
TF	Thermal fatigue
XRD	X-ray diffraction
SEM	Scanning electron microscopy
EDX	Energy dispersive x-ray spectroscopy
EBSD	Electron backscatter diffraction
SANS	Small angle neutron scattering
RDF	Radial distribution function
LOM	Light optical microscope
DSC	Differential scanning calorimetry

Part A

1 Kurzfassung

Die Einsatzbedingungen für Warmarbeitsstähle sind unter anderem gekennzeichnet durch sich zyklisch überlagernde mechanische und thermische Belastungen. Um diesen Bedingungen widerstehen zu können, werden aktuell martensitische sekundärhärtende Stähle eingesetzt, wodurch eine gute Anlassbeständigkeit und Warmhärte realisiert sind. Die dadurch erreichten mechanischen Eigenschaften führen zu einer guten Resistenz gegenüber thermomechanischer Ermüdung. Diese Art der Belastung resultiert in Brandrissen, einem oberflächennahen Netzwerk an Ermüdungsrissen, welche die Werkzeug- und dadurch die Werkstückoberfläche schädigen und den größten Einflussfaktor auf die Lebensdauer darstellen. Im Rahmen dieser Dissertation wurde die Eignung von dualhärtenden Stählen für solche Warmarbeitsanwendungen untersucht. Dualhärtende Stähle nutzen sowohl die Ausscheidung von Sekundärhärtekarbiden wie auch die Bildung von metallischen oder intermetallischen Phasen zur Festigkeitssteigerung. Dieses Legierungskonzept birgt das Potential, eine verbesserte Kombination aus Festigkeit und Zähigkeit zu erreichen.

Für die thermomechanische Ermüdungsprüfung wurde eine Prüfmethode angewandt, welche die komplexen thermischen und mechanischen Belastungsbedingungen während des Einsatzes in Warmarbeitsanwendungen wiedergibt. Um die Resistenz gegenüber thermomechanischer Ermüdung mit einer karbidisch oder dualhärtenden Mikrostruktur korrelieren zu können, wurden vergleichende Ermüdungsversuche an dualhärtenden Stählen und einem Warmarbeitsstahl durchgeführt. Die thermomechanischen Belastungsbedingungen wurden in einem servohydraulischen Prüfstand mit induktivem Heizsystem realisiert. Dabei wurden zylindrische Proben zyklisch erhitzt, während ein definierter Anteil der thermischen Ausdehnung mechanisch unterdrückt wird. Durch die mit steigender Temperatur sinkende Streckgrenze kommt es dabei zur akkumulierten plastischen Deformation im Druckbereich. Dies führt zur kontinuierlichen Verschiebung der Mittelspannung in den Zugbereich, ähnlich der Entstehung von oberflächennahen Zugeigenspannungen im realen Belastungsfall.

In dieser Arbeit wurde die Evolution der dualhärtenden Mikrostruktur während einzelner Wärmebehandlungsschritte sowie die Sequenz der Ausscheidungsbildung charakterisiert. Mit hochauflösenden Untersuchungsmethoden wurde der Einfluss der Belastungsbedingungen auf das Verhalten von Warmarbeitsstählen und dualhärtenden Stählen untersucht, um somit eine Korrelation der Resistenz gegenüber thermomechanischer Ermüdung mit der Mikrostruktur zu ermöglichen. Es konnte gezeigt werden, dass mit zunehmender Prüftemperatur dualhärtende Stähle gegenüber Warmarbeitsstählen einen verbesserten Widerstand gegenüber thermomechanischer Ermüdung aufweisen. Dies konnte auf ihre erhöhte Anlassbeständigkeit zurückgeführt werden. Die überlagerte mechanische Dehnungsamplitude hat keinen Einfluss auf die Vergrößerung und die partielle Auflösung der Sekundärhärteausscheidungen und dadurch bedingte Entfestigung während der Ermüdungsprüfung.

2 Abstract

In hot-work applications, tool materials are subject to complex interacting cyclic mechanical and thermal loading conditions. Current hot-work tool steels consist of a tempered martensitic matrix, strengthened by the precipitation of secondary hardening particles. This allows for a high tempering resistance and red hardness, which in turn ensure resistance to thermomechanical fatigue. This fatigue causes the formation of a network of fine surface cracks, called heat-checks, which are currently the major life-limiting failure mechanism for hot-work tools. In the frame of this thesis, the performance of dual hardening steels was compared to hot-work tool steels in order to evaluate their eligibility for hot-work applications. Dual hardening steels combine the precipitation of secondary hardening carbides with the formation of intermetallic or metallic precipitates, thus, providing high strength levels whilst the amount of embrittling carbides is reduced.

A test method was chosen in order to recreate the complex cyclical thermal and mechanical loading conditions present during hot-work applications on a laboratory scale. Special emphasis was put on the understanding of the influence of these loading conditions on the microstructure of hot-work and dual hardening steels in order to be able to correlate the resistance against thermomechanical fatigue to single and dual hardening. The thermomechanical fatigue tests were carried out by a servo-hydraulic test rig combined with an inductive heating system. In these tests, cylindrical specimens are heated cyclically whilst a certain percentage of the thermal expansion is mechanically suppressed. The decreasing yield strength at increasing temperatures leads to an accumulation of plastic compression, thus, a continuous shift of the mean stress in the tensile region, simulating the formation of residual tensile stresses in the surface region of a pressure casting die.

The microstructural evolution of a dual hardening steel during heat treatment as well as early precipitation reactions during ageing were investigated utilizing electron backscatter diffraction and atom probe tomography. High resolution techniques including transmission electron microscopy were utilized in order to evaluate the influence of the thermomechanical loading conditions on the microstructure of single hardening hot-work tool steels and dual hardening steels. It could be shown that with increasing test temperatures, despite the lower solvus temperatures of the intermetallic phases, the dual hardening steel achieves higher resistance to thermomechanical fatigue compared to the hot-work tool steel due to its increased tempering resistance. The superposition of a mechanical strain amplitude had no effect on the softening caused by the Ostwald ripening and partial dissolution of the secondary hardening precipitates.

3 Introduction

Today, pressure die casting is one of the most important manufacturing processes for different alloys. It realizes increased casting precision and decreased manufacturing times compared to conventional casting methods. The most important influencing parameters on costs per work piece are the cycle time and tool lifetime. The demands are, thus, contradictory in the need for increased tool lifetime combined with increasing loading conditions due to shorter cycle times and higher temperature gradients within the tool.

During pressure casting, the tool surface is heated by the injection of liquid metal whilst the core of the tool stays at intermediate temperatures, typically at 200°C [1]. Thus, the thermal expansion of the tool surface is mechanically restrained during the heating step. In combination with the fact that the yield strength decreases with rising temperatures, this leads to plastic compression. When the solidified work piece is ejected, the tool surface gets cooled, which can lead to a lower temperature compared to the tool core, resulting in tensile stresses which are superimposed by the residual stresses from the localized plastic deformation during the heating step. This process is repeated periodically during each cycle, leading to the accumulation of tensile residual stresses until a fine fatigue crack network is formed. This kind of material damage is called heat-checking or thermal fatigue and is currently the major lifetime limiting factor for hot-work tools in pressure casting applications [2]. Thermal fatigue is classified as Low-Cycle-Fatigue (LCF), with significant amounts of cyclic plastic deformation [3].

Typical steels deployed as pressure casting tools include 5 % Cr hot-work tool steels [4]. These steels consist of a martensitic microstructure, strengthened by nm-sized secondary hardening carbide precipitates. In recent years, efforts have been made in order to utilize dual hardening steels in hot-work applications. These steels have a reduced carbon content compared to hot-work tool steels, which results in a softer martensitic matrix and a reduced amount of secondary hardening carbides, but also less large, embrittling primary carbides [5–7]. The loss in strength is compensated by the addition of suitable amounts of Cu, or (Ni+Al), which form high particle number densities of metallic or intermetallic precipitates. The rapid intermetallic precipitation kinetics allows the intermetallic particles to act as heterogeneous precipitation sites for the secondary hardening carbides, which causes a homogenization and refinement of the nanostructure. The result is a further increase in toughness [8]. However, in hot-work applications, not only room temperature mechanical properties are important, but also strength and toughness at increased service temperatures and the thermal stability of the microstructure.

This thesis aims to investigate the utility of dual hardening steels for hot-work applications. Microstructural investigations are supported by high-resolution techniques such as atom probe tomography (APT) and transmission electron microscopy (TEM) to characterize the precipitation behavior and acquire microstructure-property relationships for these complex alloying systems. In a further step, a test method recreating the loading conditions present under

pressure casting applications is evaluated and adopted for high-alloyed hot-work and dual hardening steels. Out-of-phase thermomechanical fatigue (OP-TMF) tests are carried out and the results interpreted with respect to the nm-sized secondary hardening precipitates. Separate influences of plastic mechanical strain amplitudes and cyclic thermal loadings are investigated.

The following pages will give a summary of the state of the art, describe the investigated steels and outline the most important findings with regard to the appended publications.

4 State of the Art

4.1 Pressure casting

During pressure casting applications, tools are subject to overlapping cyclic thermal and mechanical loading conditions. Material properties needed to achieve high lifetimes in these operating conditions include high red hardness, hot toughness, tempering resistance, oxidation resistance, hot wear resistance and resistance against thermomechanical fatigue [2, 4]. When liquid material is injected into a die, the surface temperature of the tool increases rapidly to temperatures exceeding 600°C, depending on the injected material. The core of the tool, where additional cooling may be applied, stays at intermediate temperatures of about 200°C [1]. Thus, the thermal expansion ε_{th} of the tool surface is suppressed by the cooler core, which in combination with the decreasing yield strength leads to plastic compressive deformation of the tool surface. The thermal stresses σ_{th} can be described by [9]:

$$\sigma_{th} = -E * \varepsilon_{th} = -E(T) * \alpha_{th} * (T_1 - T_2)/(1 - \nu) \quad (1)$$

The thermal stresses σ_{th} depend on the (temperature dependent) Young's Modulus $E(T)$, coefficient of thermal expansion α_{th} , temperature difference between tool surface and core T_1 and T_2 , and the poisson's ratio ν . For steel, ($E = 210$ GPa [10] and α_{th} of appr. $12 \cdot 10^{-6} \text{ K}^{-1}$ [11]) this results in thermal stresses of about 2.5-3.5 MPa / K.

At the end of the casting cycle, the tool surface is cooled, which leads to the formation of tensile residual stresses in the surface region. The repeated casting process leads to the continuous accumulation of deformation, and thus increase of tensile residual stresses, until a fine surface crack network, called heat-checks, is formed. An exemplary heat-checking pattern on a surface and cross-section are shown in Figure 1. This fatigue behavior is called thermal fatigue (TF) and marks the most significant cause for pressure casting die failure [2, 12].

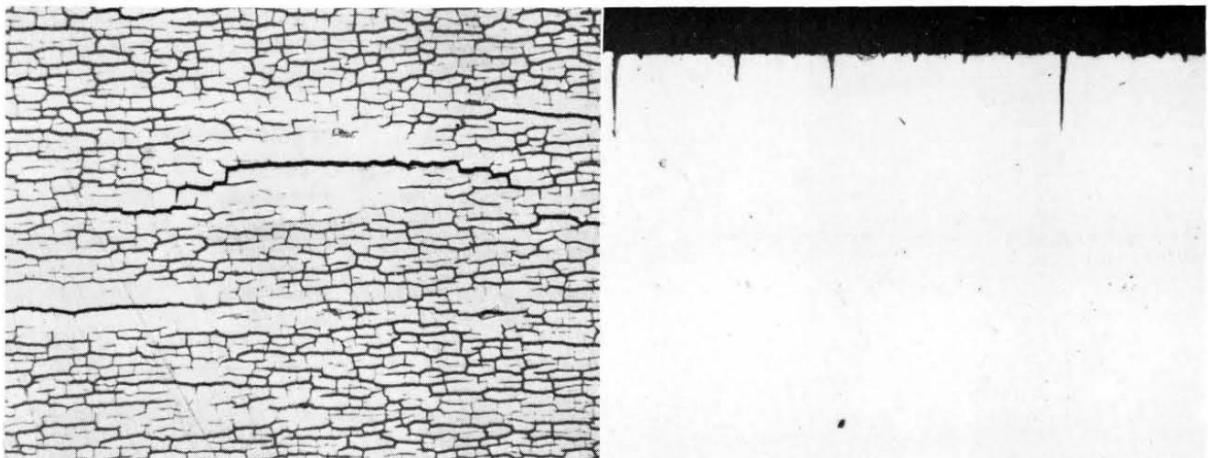


Figure 1: Exemplary heat-checking pattern on surface and cross-sections after thermal cycling [13].

4.2 Thermal fatigue

Thermal stresses can be induced by thermal gradients (position dependent temperature fields), time dependent temperature fields or combinations of materials with different coefficients of thermal expansions, see Figure 2. According to Spera [3], TF belongs to the regime of LCF, which occurs under mechanical loads between the materials yield strength and tensile strength, i.e. with cyclic plastic deformation and relative low cycle number until fracture, in the regime of 10^4 [3]. Spera's classification of TF and TMF is depicted in Figure 3. During pressure casting as described above, the load profile includes variable temperatures, which has to be clearly distinguished from isothermal fatigue, which occurs at increased but constant temperatures. TF is further divided into internal and external constraints. In the case of internal constraints, no external loads are present, which is the case if site dependent temperature distributions or combinations of materials/microstructure constituents with different coefficients of thermal expansion are present, see Figures 2 a) and b). In the case of TMF, time-dependent temperature fields in combination with the constraint of thermal expansion (for example temperature variations within fixed clamping devices) are present. This leads to external loads acting on the material as shown in Figure 2 c) [3].

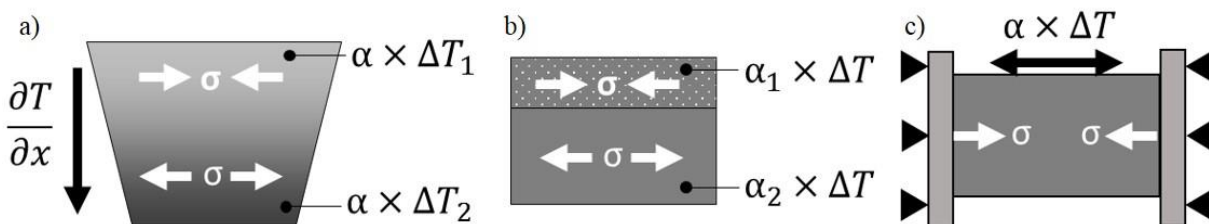


Figure 2: Conditions leading to the formation of thermal stresses. a) Position dependent temperature fields, b) combination of materials with different coefficients of thermal expansion, c) time dependent temperature fields under constraint of thermal expansion (adapted from [14]).

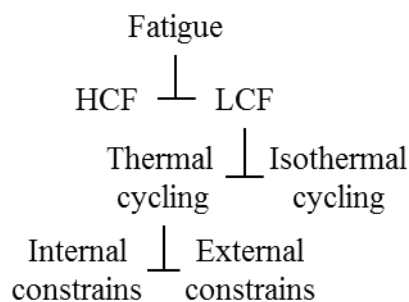


Figure 3: Classification of thermal fatigue according to Spera (adapted from [3]).

Especially tempering resistance and hot yield strength are of utmost importance for resistance against TF [13]. Influencing factors on resistance against thermal fatigue further include thermal and cyclic softening behavior, development of residual stresses and the microstructure.

A high thermal conductivity reduces temperature gradients and a low coefficient of thermal expansion (and in theory, Young's Modulus) directly reduce thermal stresses [1, 9, 15]. A high tensile strength improves the TF lifetime in the case of low strain ranges, whereas ductility is more important in the case of high strain ranges, where high strength can have a negative influence on the lifetime [14, 16].

In the case of OP-TMF testing, a phase shift between the thermal and external mechanical loading is used. Referring to the conditions during pressure casting, the surface region experiences compressive stresses during the heating period, which is represented by a phase shift of 180° between thermal and mechanical loading. Thus, OP-TMF is the most commonly used test setup to recreate the loading conditions endured by hot-work tools during application [17]. Other frequently applied TF test methods include alternating immersion of specimens in a bath of molten Al and water [18–22], induction heating of hollow, internally cooled cylinders [23–28], and surface heating via laser irradiation [1, 29]. TMF testing by inductive heating of clamped specimens whilst a defined percentage of the thermal expansion is mechanically suppressed yields the advantage of being able to monitor stress and strain evolution during the lifetime [30, 31]. The constraint factor K_{TM} describes the ratio between the mechanical strain ε_{mech} and thermal strain ε_{th} , i.e. the proportion of the thermal expansion being mechanically suppressed:

$$K_{TM} = \frac{\varepsilon_{mech}}{\varepsilon_{th}} \quad (2)$$

Figure 4 depicts the schematic evolution of the stress and temperature during OP-TMF. In Figure 4 a) the first cycles are shown. As a certain percentage of the thermal expansion is mechanically suppressed, compressive stresses are induced, until the hot compressive yield strength is reached and plastic deformation occurs. When the temperature is decreased, formation of tensile stresses is obtained [1, 32, 33]. This process is repeated during each cycle, which leads to the stress evolution shown in Figure 4 b).

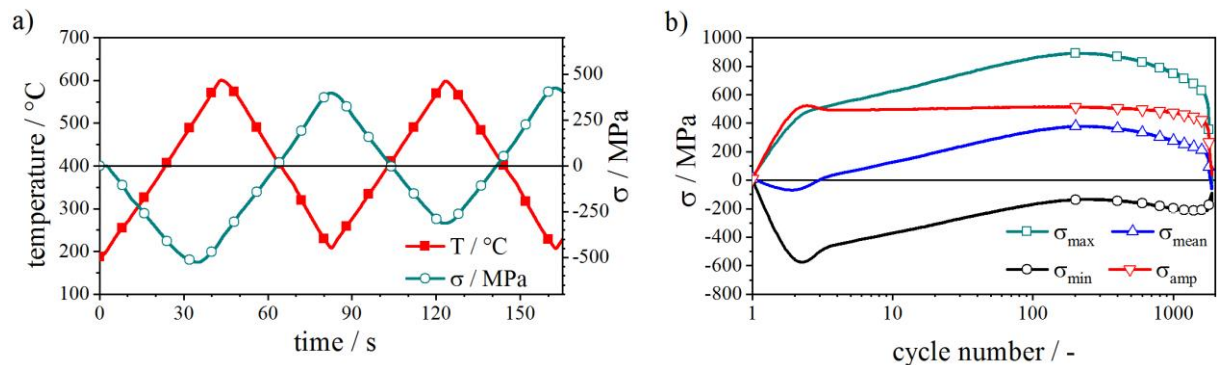


Figure 4: a) Course of the stress and temperature during the first TMF cycles. b) Stress evolution until failure under OP-TMF conditions.

In order to describe the cyclic plastic behavior of a material, fatigue tests with a constant strain level can be used. If the stress amplitude needed to achieve this strain increases with increasing cycle numbers, the material experiences cyclic hardening. This is usually caused by an increasing dislocation density due to the plastic deformation. If the amplitude decreases, cyclic softening via annihilation of dislocations or the formation of persistent slip bands is dominating [34]. At increased temperatures, further processes such as creep, recovery, recrystallization, coarsening or dissolution of precipitates can occur and contribute to the cyclic softening [35]. Due to the high stress levels, low cycle numbers are achieved, which in combination with short cycle times caused by rapid heating and cooling rates leads to creep damage usually being negligible under OP-TMF conditions [36]. For precipitation hardened alloys, the cyclic hardening/ softening behavior can depend on the stress amplitude. At low stress amplitudes, cyclic hardening is observed. With increasing stress levels, coherent precipitates can be cut and coarse slip occurs, resulting in cyclic softening [37].

During TF testing, the highest compressive stresses, and thus the most severe plastic deformation occurs in the first cycle [38]. The heat-checking density follows a sigmoidal evolution, rapidly levelling off into a plateau. The stabilized plateau depends on the heating rate, but is not influenced by the maximum testing temperature or initial hardness [28, 39, 40]. The maximum surface temperature does however have a significant influence on the TF lifetime of hot-work tool steels. For temperatures below 650°C, stable conditions are met after initial cyclic isotropic softening. For maximum surface temperatures exceeding 650°C, continuous softening occurs [1]. A high initial hardness increases TF lifetime, as the initial hardness ranking between different heat treatment conditions of an alloy stays the same during fatigue testing [41]. Materials with higher hardness develop high number densities of short cracks, whereas lower hardness values lead to small numbers of long cracks. The softening during TF further increases the crack number density [42]. The crack length for hot-work tool steels can be correlated with the depth of decarburization, whereas maraging steels soften due to overaging, and thus develop a high number density of short cracks [20].

By increasing the austenitization temperature, TF resistance can be increased due to a higher particle number density of secondary hardening precipitates, which increases the tempering resistance. However, the loss of toughness caused by the growth of austenite grains becomes the major contributing factor at higher temperatures, decreasing TF lifetime [43].

Surface oxidation can accelerate the formation and growth of fatigue cracks, as cracks preferentially initiate in the oxide layer [44, 45]. Testing under reduced O₂ partial pressure results in the change of global to localized oxidation. The cycles until crack initiation can be severely influenced by varying the O₂ partial pressure [21, 46–48]. The formation of a porous oxide layer allows a flux of O (or Al, in the case of immersion in molten Al) to the crack tip. The volume increase caused by the oxide formation at the crack surface adds to the tensile stresses at the crack tip. Furthermore, the difference in the coefficient of thermal expansion between the material and oxide layer introduces additional thermal stresses [42].

The oxidation behavior or formation of intermetallic compounds due to reactions between the tool material and cast melt can be influenced by the application of coatings [48]. However, brittle surface layers with misfits between the coefficient of thermal expansion to the substrate can lead to delamination effects and accelerated fatigue crack initiation [49], whereas positive effects can be achieved if the coating system is adapted to the application [50, 51]. For nitrided surfaces, the formation of a diffusion zone is preferential to a compound layer. The compound layer acts as a brittle surface layer, whereas the diffusion zone induces compressive residual stresses, which counteract crack initiation and increase the surface hardness [52].

Due to the high temperatures, softening occurs not only during heating under compression, but also during the cooling step under tensile loads. The major influencing step is however the heating period [17]. Not only the coarsening of secondary hardening precipitates, but also a decrease in the dislocation density contributes to softening [53–55]. In austenitic stainless steels, the dislocation arrangement is independent of in-phase or out-of-phase TF loading conditions [47]. In maraging steels and Ni base alloys, coarsening of the intermetallic precipitates is the major contribution factor to softening and accelerates crack formation and propagation [20, 35, 42]. Softening effects are divided into “temperature-time” induced and “plastic strain-number of cycle”; the sole time-temperature equivalent approach underestimates the amount of softening. For 5 % Cr hot-work tool steels, during the first 100 TF cycles, the plastic straining is the main contributing mechanism, leading to dislocation rearrangement and annihilation. At increasing cycle numbers, the temperature-time induced softening continuously becomes more dominant, caused by the coarsening of secondary hardening carbides [55–57]. Thermal stable ODS particles are, despite high operating or testing temperatures, not subject to coarsening, and therefore reduce the amount of cyclic softening as they act as stable dislocation obstacles [58, 59].

4.3 Precipitation reactions

By forming nm-sized, homogeneously distributed precipitates, a material can effectively impede dislocation movement, and thus increase its strength. In order to realize precipitation, the matrix element must have a decreasing solubility for the precipitate forming elements with decreasing temperature. During a solution heat treatment, followed by rapid cooling (quenching), a super-saturated matrix is formed. Subsequent ageing at intermediate temperatures causes the second phase to precipitate. The increase in strength is influenced by the size and average distance between these precipitates, their distribution, chemistry and crystallography [60, 61]. The formation of precipitates is typically divided into three steps:

1. Nucleation / cluster formation
2. Precipitate growth
3. Coarsening (Ostwald Ripening)

4.3.1 Cluster formation

In order to form thermodynamic stable clusters, a nucleation barrier has to be overcome. This energy barrier is caused by the different energetically contributions, including free volume energy, the surface energy of the new phase and elastic strain contributions. To reach a thermodynamic stable state, a cluster has to reach a critical size. A graphical description of the different energy contributions and the critical cluster size is shown in Figure 5.

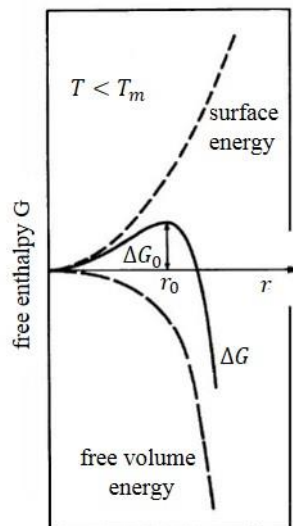


Figure 5: Free energy of a cluster as a function of cluster size r at a given temperature (adapted from [61]).

4.3.2 Homogeneous/ heterogeneous precipitation

Homogeneous precipitation only takes place if no sites for heterogeneous precipitation are available. In the case of heterogeneous precipitation, lattice defects (i.e. dislocations, grain and phase boundaries, ...) are used in order to reduce the surface energy needed to form a stable precipitate. However, if the surface energy between the precipitate phase and the matrix is very small compared to the free volume energy, homogeneous and heterogeneous precipitation can occur simultaneously, which is assumed to be the case for NiAl in ferrite. Precipitate phases can also form metastable transition phases, like the Guinier-Preston zones in Al-Cu alloys, or Cu in ferrite, which require a reduced activation energy barrier to be overcome, and thus facilitate precipitation.

4.3.3 Precipitate growth

Growth of precipitates can take place simultaneously during ongoing precipitation. The growth rate is limited by the diffusion and the rate at which the atoms cross the interface between matrix and precipitate phase. During the early stages, crossing of the interface is likely to be the velocity-determining step, whereas the diffusion rate becomes predominant at larger precipitate sizes. The diffusion controlled growth of spherical precipitates can be described by [62]:

$$r = \alpha * (Dt)^{1/2} \quad (3)$$

The particle radius r depends on the matrix super saturation α , and shows a square root dependence on time t and exponential dependence on temperature via the diffusion coefficient D . Growth takes place as long as the matrix remains super saturated and is characterized by an increasing volume fraction of the precipitate phase. Once the matrix reaches its saturated state, further ageing results in coarsening (Ostwald ripening).

4.3.4 Ostwald Ripening – LSW theory

During coarsening, the precipitate phase fraction does not increase. The main driving force for precipitate coarsening is the reduction of the interfacial free energy by reducing the overall interface area. Small particles have a larger ratio of surface area to volume. Thus, larger particles grow at the expense of smaller ones. If the rate determining step is again lattice diffusion, the coarsening rate is given by [63, 64]:

$$\bar{r}_t^3 - \bar{r}_0^3 = 8D\sigma(V_m')^2 C_m t / 9RT \quad (4)$$

Where \bar{r}_0 and \bar{r}_t are the average particle radius at time 0 and time t , D is the diffusion coefficient, σ the interfacial free energy of the precipitate/ matrix interface, V_m' the molar volume of the precipitate phase per mole of the diffusate, C_m the concentration of the solute in the matrix, T the temperature and R the gas constant. Thus, at any given temperature, precipitates with a higher difference in concentration of alloying elements between precipitate and matrix experience higher thermal stability and lower coarsening rates. The coarsening rate further rises with increasing particle size [65].

When applied to continuous heating or cooling, Equation (4) changes to [66]:

$$\bar{r}_t^3 - \bar{r}_0^3 = \frac{t c_1}{T} \exp\left(\frac{-Q_s}{RT}\right) \quad (5)$$

Where c_1 is a kinetic constant and Q_s the activation energy for the process of coarsening.

4.3.5 Dissolution of precipitates

Dissolution of precipitates is driven by the free energy change of formation and can occur well below the solvus temperature of the equilibrium phase. Due to the curvature of the interface between a particle and the matrix, the precipitate experiences an external pressure, reducing its Gibbs energy, which is more pronounced for small particles compared to large ones. This effect is called the Gibbs-Thompson effect. Thus, the solvus temperature of particles depends on their size and form (radius of curvature) and differs from the equilibrium condition. As a consequence, at a certain temperature precipitates in the aged condition might be dissolved

whilst overaged particles remain stable dislocation barriers [67–69]. The dissolution of particles during continuous heating or cooling can be described by [67]:

$$f = f_0 \left\{ 1 - \frac{2}{r_0^2} \int_{t_1}^{t_2} \alpha D_m dt \right\}^{3/2} \quad (6)$$

According to Equation 6, the volume fraction f of a precipitate phase depends on the initial volume fraction f_0 and particle radius r_0 , the matrix super saturation α , and the element bulk diffusivity D_m .

4.3.6 Influence of mechanical strain on precipitate behavior

The superimposition of cyclic mechanical stresses and constant thermal loads has been observed to influence coarsening and dissolution reactions. Repeated subgrain boundary movement or the cutting by dislocations is able to affect the thermal stability of carbides [70]. At certain constant temperatures, softening caused by carbide coarsening is only observed in the presence of mechanical loading conditions. Compared to unloaded annealing, the addition of a mechanical strain amplitude is able to significantly increase the mean carbide size [53, 54, 71]. Under creep conditions (constant mechanical and thermal loads), the coarsening rate, however, only depends on the temperature and is not influenced by the applied mechanical load [72].

Under isothermal cyclic loading conditions, precipitation hardenable Al-Cu alloys show initial hardening followed by softening. The amount of softening increases with increasing precipitation size. Thus, the precipitated particles are dissolved when a certain dislocation density is reached [73–75]. The lifetime under thermal fatigue conditions can be improved by a solution annealing and artificial ageing heat treatment, or even overageing of the precipitates [76–78]. These improvements can be caused by an increased toughness, which plays an important role under fatigue conditions, as well as the increased thermal stability of larger, overaged precipitates [67].

However, the current literature yields no information on the influence of combined cyclic mechanical strain and variable temperatures, as predominant under TMF conditions, on precipitate behavior.

4.4 Dual hardening steels

The first investigations on dual hardening steels were conducted in the late 70s of the 20th century [79, 80]. Investigated alloys contained Ni as well as Al in order to form intermetallic precipitates of NiAl in addition with 0.3 wt% C. However, these alloys lacked typical special carbide forming elements such as Cr, Mo or V. The alloying concept was developed in order to increase the fatigue strength of quenched and tempered martensitic steels. In later years, the

potential of dual hardening steels to combine high strength achieved by high particle number densities of precipitates with good levels of fracture toughness was discovered [5, 6].

Another advantage of the dual hardening alloying concept is its performance under cyclic loading conditions. The combination of coherent NiAl and semi-coherent M_2C carbides results in a homogeneous deformation behavior, avoiding limitation of the dislocation movement to a few preferred slip bands [81]. The absence of Ti and therefore possibility to form embrittling Ti(C,N) inclusions, in addition to an increased yield strength, allows these dual hardening steels to achieve higher fatigue resistance compared to Ti-alloyed maraging steels [82]. This led to their further development and service in aeronautical applications, i.e. as turbine shafts. More recently, their potential usability for hot-work applications has been discovered [8, 83, 84]. In order to achieve high lifetimes under hot-work loading conditions, red hardness and tempering resistance are of utmost importance [13, 85]. Both are most affected by the thermal stability of the secondary hardening precipitates. In a X38 CrMoV 5-3 hot-work tool steel, MC carbides show the lowest coarsening rate up to temperatures of 650°C. At 680°C, significant coarsening of MC carbides occurs as well as dissolution of M_2C carbides [86]. Intermetallic NiAl-particles are stable in a 13Cr-8Ni-2.5Mo-2Al martensitic stainless PH steel at ageing temperatures of up to 620°C [87], possessing an equilibrium solvus temperature of up to 650°C according to thermodynamic calculations with MatCalc 6 ME_Fe1.2.

The intermetallic phases utilized in dual hardening steels must, in addition to a high thermal stability, consist of non-carbide forming elements. Due to its high affinity to form Ti(C,N), intermetallic phases including Ti (for example Ni_3Ti , which is frequently used in C free maraging steels) have not been used in dual hardening alloys thus far [84]. As TiC forms during the solidification process, Ti is not available for precipitation hardening by a solution annealing and ageing heat treatment. However, simulation guided alloy design concepts conclude the combination of MC, Cu and Ni_3Ti to achieve the best combination of mechanical properties [88, 89]. Despite the high affinity of Ti to form TiC during solidification, Ni_3Ti precipitates were detected in investigated test alloys [88, 89]. Mo-rich carbides, usually Mo_2C , show less rapid formation kinetics compared to Mo containing intermetallic phases. This fact might open up the possibility for them to be used for the precipitation of Mo containing intermetallic phases, such as the μ -Phase $(Fe,Co)_7Mo_6$ or Laves-Phase Fe_2Mo , if these experience faster precipitation kinetics compared to the Mo_2C carbides.

Up to now, intermetallic phases utilized in dual hardening steels either contain Ni and Al - forming the intermetallic compound NiAl - or Cu [84, 90–93]. Due to the coherency to the ferritic iron matrix, NiAl exhibit rapid precipitation kinetics, forming homogeneously distributed spherical precipitates [94–96]. The NiAl particles possess an ordered B2 (CsCl) structure [97]. Mn is preferably incorporated in the NiAl precipitates [98], where it substitutes either Al [99] or Ni [83].

The precipitation of Cu from supersaturated ferrite undergoes a multi-step process. Through the formation of a coherent bcc CuFe cluster, Cu achieves rapid precipitation kinetics. The inclusion of high amounts of Fe further reduces the nucleation barrier [100, 101]. These bcc precipitates undergo a martensitic transformation into a 9R structure, before transforming into their equilibrium fcc structure [100, 102–105]. The final Cu particles contain a negligible amount of iron. In 15-5PH maraging steels, CuFe clusters form between 200°C and 400°C during continuous ageing with a heating rate of 15 Kmin⁻¹. At 500°C the precipitates reach their equilibrium composition [106, 107].

If sufficient alloying contents for the precipitation of both NiAl and Cu are present, the sequence of precipitation depends on the ratio of Cu/Al and Cu/Ni [108]. If a high ratio of Cu/Al and Cu/Ni (between 0.5 in [109] and 2.8 in [110]) is present, precipitation starts with CuFe clusters. During further ageing, these clusters and their interface to the iron matrix enrich in the solute elements Ni, Al and Mn [107, 111–113]. Subsequently, heterogeneous precipitation of NiAl takes place [108, 109, 112, 114, 115]. If the alloying ratio of Cu/Ni and Cu/Al is low (0.3 in [116]), precipitation starts with NiAl clusters, which via enrichment in Cu [117] cause heterogeneous precipitation of Cu at the NiAl interfaces [108]. Table 1 provides an overview of investigated alloying contents and ratios of Cu/Ni and Cu/Al and the reported precipitation sequence. The alloy investigated in [118] additionally contains Ti, which alters the precipitation sequence by introducing Ni₃Ti. The addition of Cu is able to retard the coarsening of the NiAl particles. The inclusion of Cu in the NiAl precipitates is expected to decrease the misfit to the iron matrix, and thus causes a change in the coarsening mechanism [119].

Table 1: Overview of alloying ratios of Cu/Al and Cu/Ni and reported sequence of precipitation in various publications.

Ni wt%	Al wt%	Cu wt%	Cu/Ni wt%/wt%	Cu/Al wt%/wt%	Cu/Ni at%/at%	Cu/Al at%/at%	sequence	
0.8	0.3	2.0	2.7	6.7	2.5	2.8	Cu	[110]
0.8	0.03	1.4	1.7	40.3	1.5	17.1	Cu	[111]
2.8	0.7	2.1	0.7	3.1	0.7	1.3	Cu	[114]
4.0	1.5	3.0	0.8	2.0	0.7	0.8	Cu	[115]
2.8	0.7	1.3	0.5	1.9	0.5	1.0	Cu	[112]
2.8	0.6	1.3	0.5	2.2	0.5	0.9	Cu	[109]
10.3	1.1	1.9	0.2	1.7	0.2	0.7	NiAl / Cu before Ni ₃ Ti	[118]
2.6	0.6	2.5	1.0	4.2	0.9	1.8	N/A	[120]
4.0	1.5	3.0	0.8	2.0	0.7	0.8	N/A	
5.0	2.0	1.5	0.3	0.8	0.3	0.3	NiAl	[116]

In dual hardening steels, the NiAl and Cu particles can act as heterogeneous precipitation sites for secondary hardening alloy carbides, resulting in a size refinement and homogenization of the carbide distribution [83, 91, 121–123]. The homogeneous carbide distribution causes the combination of high strength and toughness of dual hardening steels [8]. The formation of iron carbides is not affected by NiAl [124] or Cu alloying, moreover cementite acts as precipitation site for Cu [125].

Segregation of Cr and Mo and precipitation of M_2C at the interface between the NiAl or Cu particles and the iron matrix counteracts coarsening and leads to a thermal stabilization effect. The growth kinetics of M_2C carbides are unaffected by the presence of NiAl [87, 122, 123]. However, in [126], the high number density of fine NiAl particles is assumed to impinge the growth of large tubular Mo_2C carbides by disturbing both growth and diffusion, resulting in areas with small spherical carbide clusters. These fine clusters dissolve upon further ageing, when the NiAl begin to coarsen. After prolonged ageing times, NiAl have been reported to promote the dissolution of carbides in favor of the formation of reverted austenite [124, 127].

4.5 Characterization of precipitates

Precipitates are the most relevant microstructural constituent with respect to red hardness and tempering resistance, and thus resistance against thermal fatigue. During thermal cycling, microstructural constituents with different coefficients of thermal expansion induce additional thermal stresses and can lead to crack initiation. Due to that, primary or secondary carbides can have a significant influence on the fatigue life. As their size ranges from a few hundred nm to μm , different characterization methods are utilized for their characterization and quantification. These include x-ray diffraction (XRD), scanning electron microscopy (SEM) including energy dispersive x-ray spectroscopy (EDX) and electron backscatter diffraction (EBSD). The characterization of secondary hardening precipitates with a size in the range of a few nm requires methods with a higher resolution, such as small angle neutron scattering (SANS), transmission electron microscopy (TEM) or atom probe tomography (APT) [93, 128].

Due to its near atomic resolution in combination with the ability to detect any chemical element with the same probability, APT is a very powerful tool to investigate precipitation reactions in complex alloying systems [129]. However, especially when investigating small precipitates and their interface to the surrounding matrix, ion trajectory effects have to be considered. These effects are caused by phases with different evaporation fields and can lead to local magnification of individual microstructure constituents [130, 131]. The determination of the exact chemical composition of carbides is furthermore impaired by increased amounts of multiple detection events within these carbides [132].

The analysis of APT data is very sensitive to user defined parameters [133], especially when applied to clusters search or to identify early stages of precipitation. In order to provide the

reader with the possibility to assess data quality and suitability to compare and correctly interpret different results, a detailed and complete report of all relevant parameters and methods used for measurement, reconstruction, data mining and data evaluation is necessary [133]. Various algorithms and data evaluation methods exist. Most of them are based on the fact that within a cluster or precipitate, the concentration of or the mean distance between the precipitating elements differs from that within the matrix. The maximum separation method defines a maximum separation distance (d_{\max}) between two solute atoms which belong to a cluster and a minimum number of solute atoms needed to form a cluster N_{\min} [134, 135]. Other species of elements incorporated in these clusters are accessed by the introduction of a grid spacing with the envelope method [136]. Advantages of the maximum separation method are ease of automation, the possibility to analyze clusters down to 1.5 nm radius and independence of cluster morphology [134]. One of the main disadvantages is the inability to identify clusters if the solute atoms do not show strong segregation. This method is furthermore sensitive to the local detection efficiency of the atom probe and, as many others, to user defined parameters [133, 134, 137]. An approach for a reasonable estimation of d_{\max} is described in [134] by plotting the number of clusters of a solute atom versus d_{\max} , as shown in Figure 6. The choice of N_{\min} depends on d_{\max} . A good estimation can be made by plotting the distribution of clusters as a function of the amount of solute atoms within a cluster for a defined d_{\max} [134]. In another approach the number of clusters is compared to a random solid solution of the same bulk composition [138].

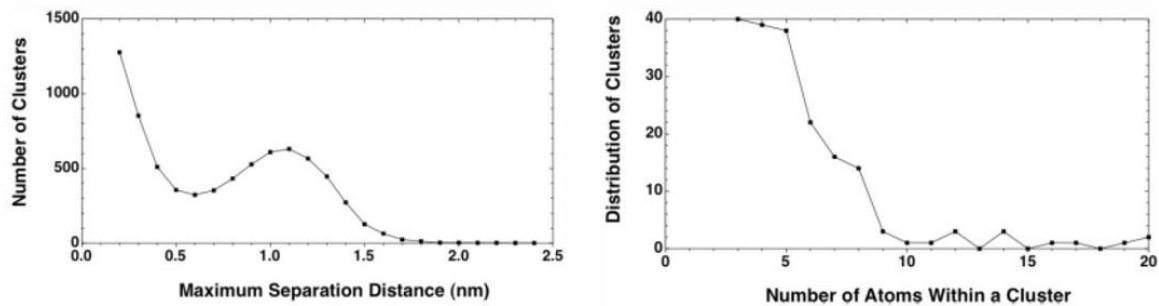


Figure 6: Suggested procedure for the estimation of d_{\max} and N_{\min} for the maximum separation method (according to [134]). In this example, a reasonable choice for d_{\max} and N_{\min} are 0.6 nm and 10-11, respectively.

The calculation of the Pearson coefficient μ marks another way to determine the level of segregation, which is independent of the sampled volume. The Pearson coefficient is based on the normalized frequency distribution analysis χ^2 , where the number of solute atoms in a defined volume element is compared to a random distribution [139].

The isosurface method is a compositional analysis technique. Inside a precipitate, the concentration of solute atoms is greater compared to the concentration within the matrix.

Precipitates are identified by a certain concentration threshold $c^{\text{threshold}}$. The isosurface method can identify precipitates independent of composition and morphology. Clusters down to a radius of 0.45 nm can be detected [140]. The selection of the user defined $c^{\text{threshold}}$ is required to produce stable results, so that small changes do not have a significant influence on the number density and size of precipitates [134]. Disadvantages include sensitivity to user defined parameters, the often unclear interpretation of the position of the interface (especially during early stages of precipitation), local magnification effects and the convolution of precipitates located in close proximity to one another. The radial distribution function (RDF) or pair correlation function determines the number of atoms in spherical shells centered around a selected solute element in the analyzed volume. The normalized RDF divides the local concentration by the average bulk concentration of that element. A value of one represents a random distribution, greater than one is indicative of clustering and below one of repulsive behavior of the selected solute atoms [141, 142]. The RDF analysis offers a high level of sensitivity, which irrespective of the limitations in APT detector efficiency and spatial resolution enables the determination of the early stages of cluster formation.

4.6 Relation of the current thesis to the state of the Art

This thesis aims to gain understanding on the impact of combined thermal and mechanical loading conditions on single and dual hardening nanostructures in order to expand the usage of complex alloying systems. It is built upon in-depth understanding of the loading conditions present under TF conditions, their recreation on the laboratory scale and separation of the individual influencing factors. By comprehending, and thus mitigating predominant damaging mechanisms, the author aims to increase the sustainability of the investigated alloying systems. Further characterization of dual hardening steels, including carbide evolution and precipitation reactions during heat treatment as well as evaluation of their performance under the aforementioned loading conditions, is carried out.

The current literature focuses on the macroscopic damage behavior during TMF, however frequently overlooking the contributions of nm-sized microstructural constituents. The characterization of those is often solely carried out in equilibrium or in different heat treatment conditions. The author therefore aims to shed light on the connection between TMF behavior and the nanostructure by combining TMF loading conditions with high resolution characterization techniques.

Ultimately, the goal is to expand the field of application of dual hardening steels towards hot-work applications. Until now, steels are commonly divided into C-free maraging steels, utilizing the precipitation of intermetallic phases, or high-carbon tool steels, limited to the precipitation of primary and secondary hardening carbides. This thesis tries to prove that steel design does not have to be restricted to one aspect or the other but can harness the positive effects of both.

5 Overview of publications

5.1 Appended papers

The appended papers can be found in part B of this thesis.

- Paper I** M. Hofinger, M. Staudacher, M. Ognianov, C. Turk, H. Leitner, R. Schnitzer
Microstructural evolution of a dual hardening steel during heat treatment
Micron 120 (2019) 48–56.
DOI: 10.1016/j.micron.2019.02.004
- Paper II** M. Hofinger, M. Ognianov, C. Turk, H. Leitner, R. Schnitzer
Early Stages of Precipitate Formation in a Dual Hardening Steel
Journal of Heat Treatment and Materials 74 (2019) 293–301.
DOI: 10.3139/105.110390
- Paper III** M. Hofinger, B. Seisenbacher, M. Ognianov, H. Leitner, C. Turk, M. Kapp, R. Schnitzer
Thermomechanical Fatigue Testing of Dual Hardening Tool Steels
steel research int. 3 (2019) 1900423.
DOI: 10.1002/srin.201900423
- Paper IV** M. Hofinger, C. Turk, M. Ognianov, H. Leitner, R. Schnitzer
Precipitation reactions in a Cu-Ni-Al medium carbon alloyed dual hardening steel
Materials Characterization 160 (2020) 110126.
DOI: 10.1016/j.matchar.2020.110126

Contributions of the author: The author of this thesis carried out the planning, conception and writing of all papers. The material was supplied by voestalpine BÖHLER Edelstahl GmbH and Aubert & Duval. All microstructural investigations, including both experiments and data evaluation, were carried out and interpreted by the author of this thesis. Following published results were produced externally:

Paper III: Thermomechanical fatigue testing was performed at the Chair of Mechanical Engineering, Montanuniversität Leoben, Austria.

Benjamin Seisenbacher, Miloslav Ognianov, Christoph Turk, Harald Leitner, Gerald Winter, Maximilian Staudacher, Marianne Kapp and Ronald Schnitzer are gratefully acknowledged for

their contribution to the papers. The author thanks Erwin Povoden-Karadeniz for the thermodynamic calculations which are mentioned later in this thesis. Christina Hofer and Irmgard Weißensteiner are thanked for their assistance with the EBSD measurements and Andreas Landefeld for performing the TEM investigations.

5.2 Co-authored papers related to this work

B. Seisenbacher, M. Hofinger, G. Winter, F. Grün

Material behaviour of a dual hardening steel under thermomechanical loading

Fatigue & Fracture of Engineering Materials & Structures 98 (2019) 104.

DOI: 10.1111/ffe.13147

5.3 Conference contributions

Hofinger M., Ognianov M., Turk C., Leitner H., Schnitzer R. (2018) Thermomechanische Ermüdungsprüfung an dualhärtenden Stählen, Oral presentation, 64th Metallkunde-Kolloquium, 09.-11.04.2018, Lech am Arlberg.

Hofinger M., Staudacher M., Turk C., Ognianov M., Leitner H., Kapp M., Schnitzer R. (2018) Metallographische Präparationsmethoden zur umfassenden mikrostrukturellen Charakterisierung dualhärtender Stähle, Oral presentation, 15. Metallographie-Tagung, 19.-21.09.2018, Leoben.

Hofinger M., Ognianov M., Turk C., Leitner H., Schnitzer R. (2019) Frühe Stadien der Ausscheidungsbildung eines dualhärtenden Stahls, Oral presentation, ASMET Werkstofftechnik & 31. Härtereitagung, 28.-29.03.2019, Wien.

Hofinger M., Seisenbacher B., Ognianov M., Leitner H., Turk C, M. Kapp, Schnitzer R. (2019) Thermomechanical Fatigue Testing of Dual Hardening Tool Steels, Oral presentation, Tooling 2019 conference & exhibition, 12.-16.05.2019, Aachen.

5.4 Supervised theses

Staudacher M. (2018) Präparationsmethoden dualhärtender Stähle. Bachelor Thesis, Montanuniversität Leoben.

Sakic A. (2019) Charakterisierung des Warmarbeitsstahles W360. Bachelor Thesis, Montanuniversität Leoben.

Proyer A. (2019) Kissinger-Analyse von Cu- und NiAl- Ausscheidungen in einem dualhärtenden Stahl. Bachelor Thesis, Montanuniversität Leoben.

Schretter L. (2019) APT investigation of the low carbon dual-hardening steel ML340. Bachelor Thesis, Montanuniversität Leoben

6 Experimental procedure

The following chapter gives a brief overview of the different investigated alloys and performed heat treatments. It furthermore contains information on the TEM and APT measurements performed on TMF tested specimens. Further details about the experimental procedures can be found in the appended papers in part B of this thesis.

6.1 Steels investigated

The chemical compositions of the alloys investigated in the frame of this thesis are given in Table 2. The hot-work tool steel is a martensitic 5 % Cr hot-work tool steel which was investigated as a reference to the dual hardening alloys. Due to its higher C content of 0.5 wt% compared to the dual hardening alloys, it comprehends of a dislocation-rich and strongly distorted, and thus stronger martensite with increased hardness. The elements Cr, Mo and V increase its hardenability and form secondary hardening carbides, leading to a high tempering resistance. The dual hardening alloy additionally contains Ni and Al next to C, Cr, Mo and V. Due to its high V content and the precipitation of VC carbides and intermetallic NiAl particles, it reaches a significant secondary hardness increase upon ageing. The Co-alloyed steel was originally developed for turbine shafts in aeronautical applications. Despite not being designed to be deployed in hot-work applications and withstand TMF conditions, it uses a dual hardening mechanism, and is thus included in this study. The high Co content is expected to achieve good tempering resistance and hot hardness, whilst the high Ni content of 13 wt% shifts the martensite finish temperature below room temperature. The triple hardening alloy is used as a plastic mold steel and utilizes three different precipitates: the precipitation of VC carbides, intermetallic NiAl and metallic Cu particles. The high contents of Mn and S form MnS, which cause its good machinability.

The hot-work tool steel was austenitized at 1050°C for 30 min, air cooled to room temperature and annealed three times for 2 h at either 570°C or 620°C. The dual hardening alloy was solution annealed at 990°C for 30 min, oil quenched to room temperature and aged three times for 3 h at 585°C. The Co-alloyed steel was solution annealed at 900°C for 1 h, oil quenched to room temperature and subsequently cooled to -80°C for 1 h. The cryogenic heat treatment step was followed by a tempering step at 200°C for 8 h. The ageing was either performed at 495°C for 5 h or 515°C for 15 h. The triple hardening alloy was solution annealed at 900°C for 30 min, oil quenched to room temperature and aged for 6 h at 580°C.

Table 2: Chemical compositions of the investigated steels.

		Fe	C	Cr	Mo	V	Ni	Al	Si	Mn	Cu	S	Co
Hot-work	wt%	90.95	0.50	4.50	3.00	0.60	/	/	0.20	0.25	/	/	/
	at%	89.90	2.30	4.78	1.73	0.65	/	/	0.39	0.25	/	/	/
Dual hardening	wt%	86.53	0.37	3.00	2.50	0.85	4.80	1.50	0.20	0.25	/	/	/
	at%	84.68	1.68	3.15	1.42	0.91	4.47	3.04	0.39	0.25	/	/	/
Co-alloyed	wt%	74.42	0.23	3.30	1.50	0.25	13.00	1.50	/	/	/	/	5.80
	at%	73.57	1.06	3.50	0.86	0.27	12.23	3.07	/	/	/	/	5.43
Triple hardening	wt%	91.19	0.13	0.35	/	0.06	3.50	1.20	0.30	2.00	1.20	0.13	/
	at%	89.49	0.59	0.37	/	0.06	3.27	2.44	0.59	2.00	1.03	0.22	/

6.2 Characterization of the nanostructure

For the TEM investigations of fatigue tested specimens, focused ion beam milling with a FEI Versa 3D HIVAC microscope was performed. The milled lamellae were transferred with an Omniprobe and welded on a lift-out grid. A final milling was then conducted with voltage down to 2 kV in an area of 5 x 5 μm . The investigations were conducted with a Jeol JEM-2200FS TEM.

The APT measurements of fatigue tested specimens were conducted with a LEAP 3000 X HR in laser mode at 60 K in order to reduce the amount of early specimen fracture caused by the coarse precipitates. Specimens were prepared by electro polishing. For both the TEM and APT investigations, special emphasis was put on the exact location of the measurements. Specimens were taken from within the central 5 mm of the longitudinal axis of the TMF samples in order to assure exact knowledge of the predominant temperature during the fatigue testing.

7 Results and Discussion

7.1 Aim and scope of the investigations

The goal of this thesis was to understand the influence of combined thermal and mechanical loading conditions on the nanostructure. Following issues were tackled by this thesis:

- What loading conditions cause the heat-checking in pressure casting applications and how can these conditions be recreated on a laboratory scale under defined and well known parameters?
- How does TMF influence the nanostructure and vice versa? How can the nanostructure be altered in order to increase a materials resistance against TMF?
- How do dual hardening steels perform under the described TMF loading conditions compared to commonly used hot-work tool steels?
- How is the microstructure of the investigated dual hardening alloys composed? How does it evolve during the performed heat treatments, and how is it affected during application?
- Which intermetallic phases can be utilized in dual hardening steels? Can carbide forming elements, such as Ti, Mo and V, be used for the precipitation of intermetallic phases and how do carbides and intermetallic phases compete?

The following pages summarize all findings and aim to provide answers to these questions with respect to the published papers which are appended to this thesis in part B.

7.2 Microstructural characterization

In order to gain understanding of the microstructure-property relationships, a thorough characterization of the microstructure is necessary. During cyclic heating and cooling of a material, different coefficients of thermal expansion of individual microstructural constituents can lead to local stress peaks, and thus accelerate crack initiation [143]. The evaluation of different etching methods in order to visualize the entirety of the microstructural constituents of the dual hardening steel, including primary and secondary carbides, showed that etching with V2A-pickle and polishing with colloidal silica suspension lead to the best results for investigations with the light optical microscope (LOM) and SEM, respectively. The carbide evolution during heat treatments was characterized in detail by the acquisition of EBSD spot-pattern, as is exemplary shown in Figure 7 (**Paper I**). The detected carbides are summarized in Table 3 (**Paper I**). By increasing the austenitization temperature from 990°C to 1200°C, the peak hardness can be increased and the μm -sized primary and secondary carbides dissolved, resulting in a coarsening of the prior austenite grains.

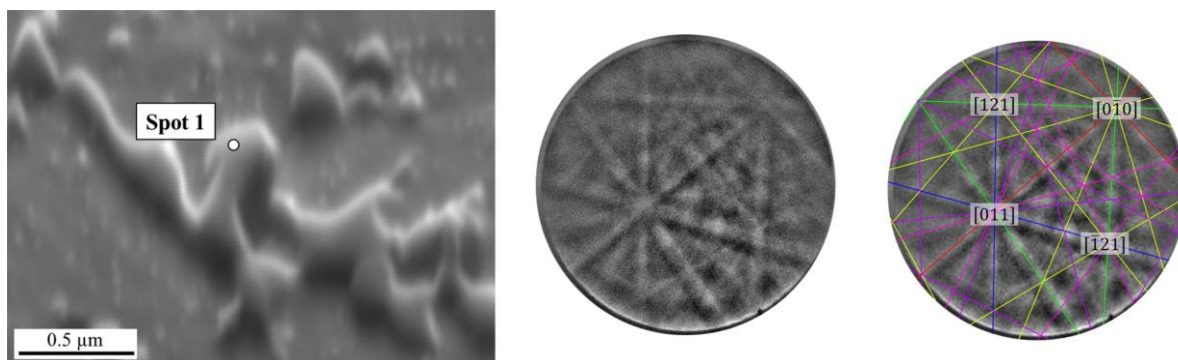


Figure 7: Characterization of carbides with the use of EBSD spot-pattern. From left to right: secondary electron SEM micrograph, pattern obtained at spot 1 and indexed solution for MC carbide (adapted from **Paper I**).

Table 3: Overview of the applied heat treatments and carbides present in each condition in the dual hardening alloy (**Paper I**).

Heat treatment condition	Carbide types
As received	MC, M ₂ C, M ₆ C
Carbide dissolution	MC, M ₂ C, M ₆ C
Austenitized and aged	MC, M ₆ C

In none of the investigated heat treatment conditions of the hot-work tool steel (except in the quenched state), retained austenite or carbides could be detected with phase analysis by XRD. The maximum carbide volume fraction measured by quantitative SEM image analysis yielded 0.25 vol%.

High resolution analysis of the dual hardening alloy and the hot-work steel in the aged conditions are performed in the frame of **Paper III**. The 5 % Cr hot-work tool steel exhibits a high particle number density of fine carbides, depicted in Figure 8 a). The plate-like or spherical carbides reach a mean core carbon content of roughly 30 at% C, significantly enriched in Mo and V and are assumed to be M₂C carbides, which is shown in Figure 8 b). The dual hardening alloy shows an increased particle number density of precipitates, including spherical NiAl precipitates and plate like carbides in combination with larger, planar M₂C carbides, which is shown in Figure 9.

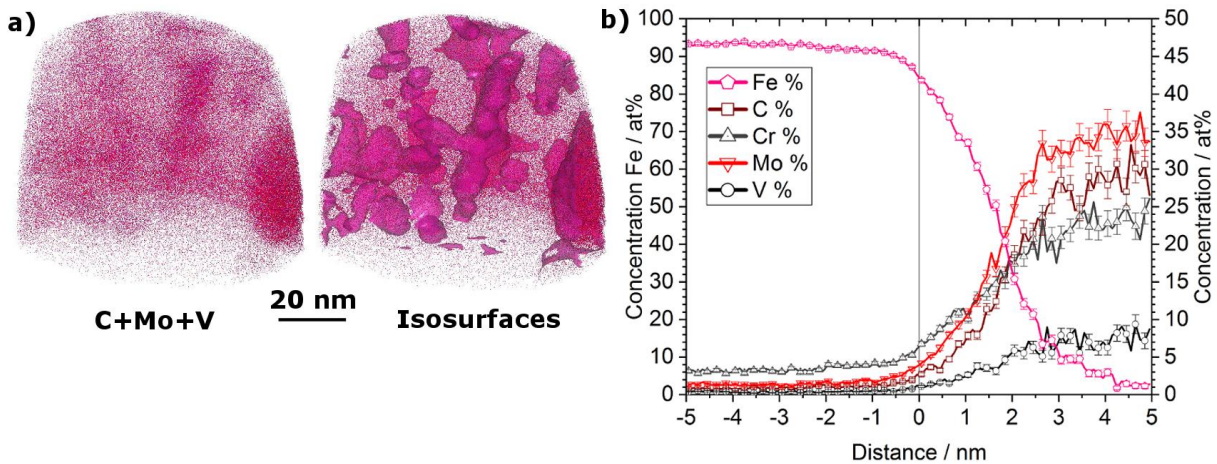


Figure 8: APT measurement of hot-work tool steel annealed three times at 620°C for 2 h. a) From left to right: atom map of (C+Mo+V), isoconcentration surfaces of 5 at% (Mo+V). b) Proximity histograms according to isosurfaces, zero distance on the abscissa corresponds to the carbide/matrix interface, positive values are inside the carbides (adapted from **Paper III**).

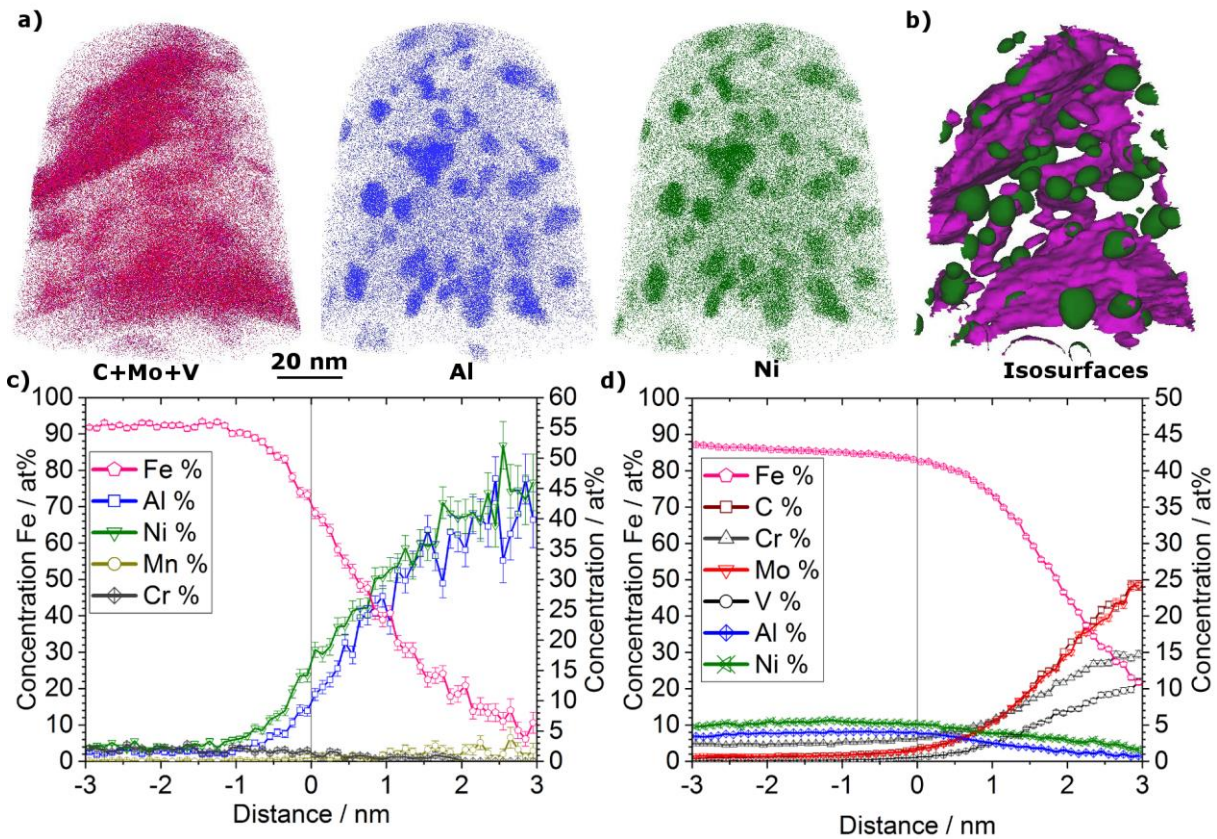


Figure 9: APT measurement of the dual hardening steel aged three times for 3 h at 585°C. a) From left to right: atom maps of (C, Mo, V), Al and Ni. b) Isoconcentration surfaces of 25 at% (Ni+Al) in green and 5 at% (Mo+V) in pink. c) Proximity histogram according to (Ni+Al) isosurfaces. d) Proximity histogram according to large plate-like (Mo+V) isosurface. Zero distance on the abscissa corresponds to the precipitate/matrix interface, positive values are inside the precipitate (**Paper III**).

An APT measurement of the Co-alloyed steel aged at 515°C for 15 h is shown in Figure 10. The NiAl particles exhibit a high particle number density of homogeneously distributed spherical particles. The measurement also shows a region enriched in Ni, without a significant amount of Al. Figure 10 c) shows the concentration profile of the cylinder in Figure 10 b) through this area, which most likely marks reverted austenite [144]. Carbides are visible in plate-like structures, including M_7C_3 , Figure 10 d) and M_2C , Figure 10 e).

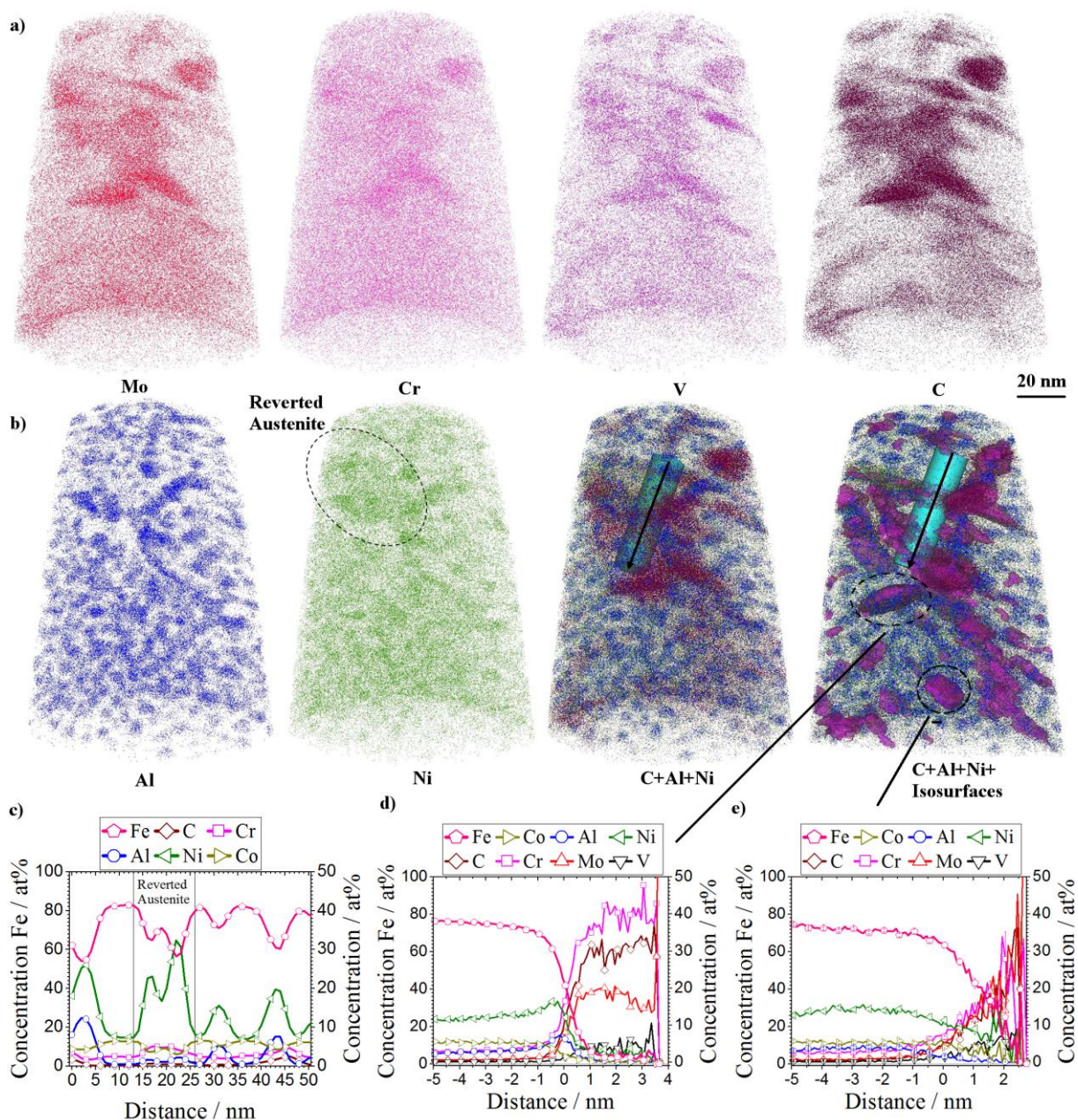


Figure 10: APT measurement of the Co-alloyed steel aged for 15 h at 515°C. a) From left to right: atom maps of Mo, Cr, V and C. b) Atom maps of Al, Ni, (C+Al+Ni) and (C+Al+Ni) + isosurfaces of 5 at% (Mo+V). c) Concentration profile of the cylinder in b) with a volume of 15x15x50 nm³. The vertical lines mark the Ni enriched reverted austenite. d) And e) proximity histograms of the marked isosurfaces, positive values are inside the precipitates.

An APT measurement of the triple hardening steel aged for 6 h at 580°C is shown in Figure 11. The alloy exhibits a high particle number density of Cu-NiAl co-precipitates, as well as plate-like VC carbides, preferentially located at the interfaces of the intermetallic particles to the iron matrix. It is interesting to note that by APT analysis, 0.06 at% V are detected, which is a suitable amount to form the observed VC precipitates. In Figure 11 c) and d) a concentration profile through a co-precipitate of the three different precipitates is shown. Whilst the VC carbides exhibit the smallest number density and mean particle size, they also incorporate significant amounts of iron. The Cu and NiAl precipitates tend to overlap, which is indicative of their assisted precipitation process as described in chapter 4.4. The NiAl are furthermore enriched in Mn.

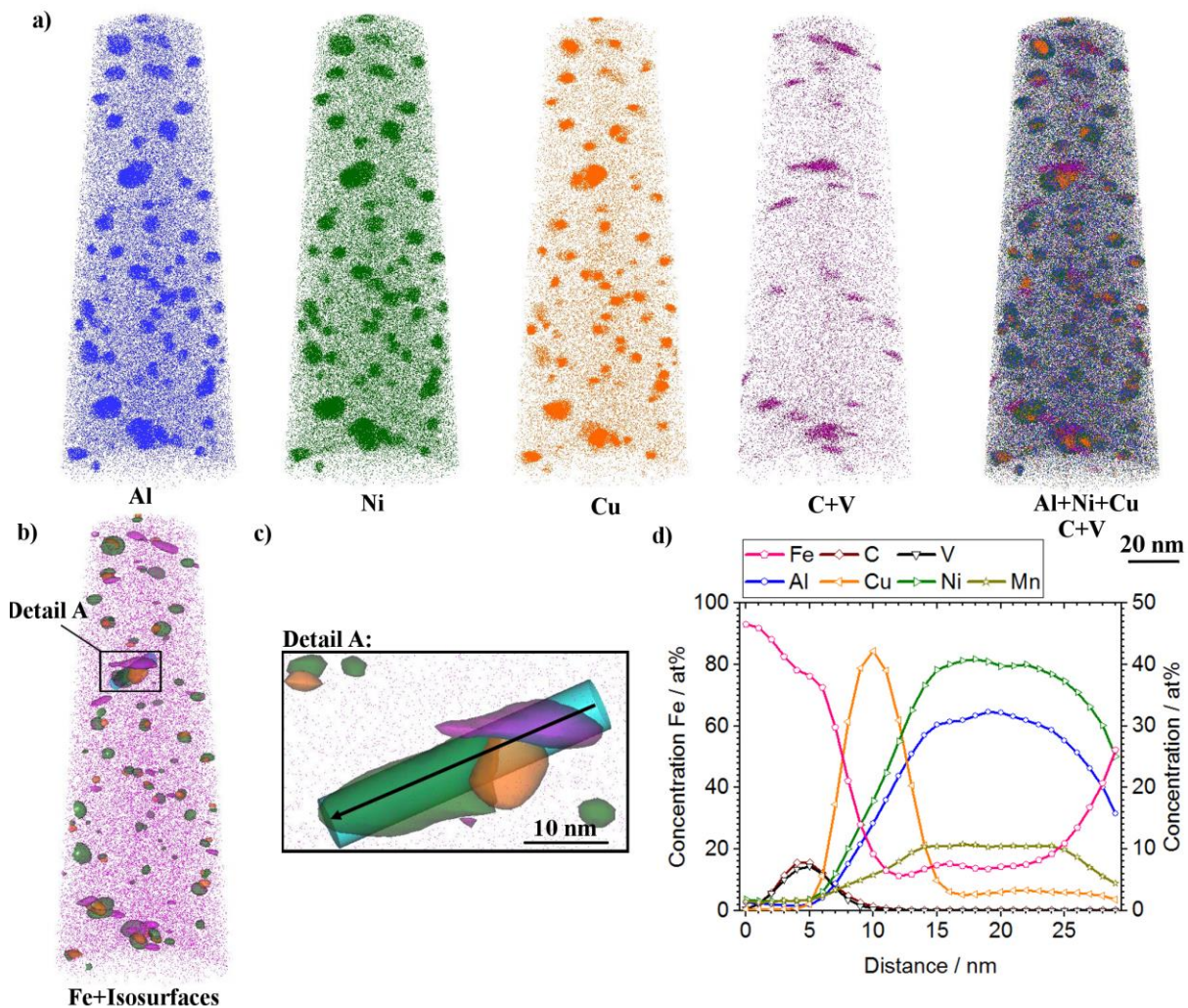


Figure 11: APT measurement of the triple hardening steel, aged at 580°C for 6 h. a) From left to right: atom maps of Al, Ni, Cu, (C+V) and (Al+Ni+Cu+C+V). b) Atom map of 30% of the detected Fe atoms, isosurfaces of 50 at% (Ni+Al) in green, 20 at% Cu in orange and 5 at% (C+V) in pink. c) Enlarged view of Detail A. d) Concentration profile along the cylinder (5.3x5.3x30 nm³) in Detail A.

7.3 Characterization of precipitation reactions

The microstructural evolution of the triple hardening steel during continuous heating is investigated in **Paper II** and **Paper IV** by means of differential scanning calorimetry (DSC) and APT. It could be shown that the precipitation of the NiAl and Cu particles starts heterogeneously at grain boundaries (**Paper II**). However, the homogeneous precipitation in the iron matrix begins with the formation of Cu clusters, enriched in Ni, Al and Mn, as can be derived from the RDF in Figure 12 (**Paper IV**). Upon further ageing, Cu shows the strongest segregation behavior. At temperatures between 580°C and 620°C, the NiAl formation stops. At 580°C, enrichment of C and V at distinct distances from the Cu segregations could be determined with the RDF, showing heterogeneous VC precipitation at the Cu particles. During continuous heating, no NiAl were formed, which precipitate at intermediate temperatures after increased holding times. Hence the precipitation sequence was determined to be Cu-VC-NiAl.

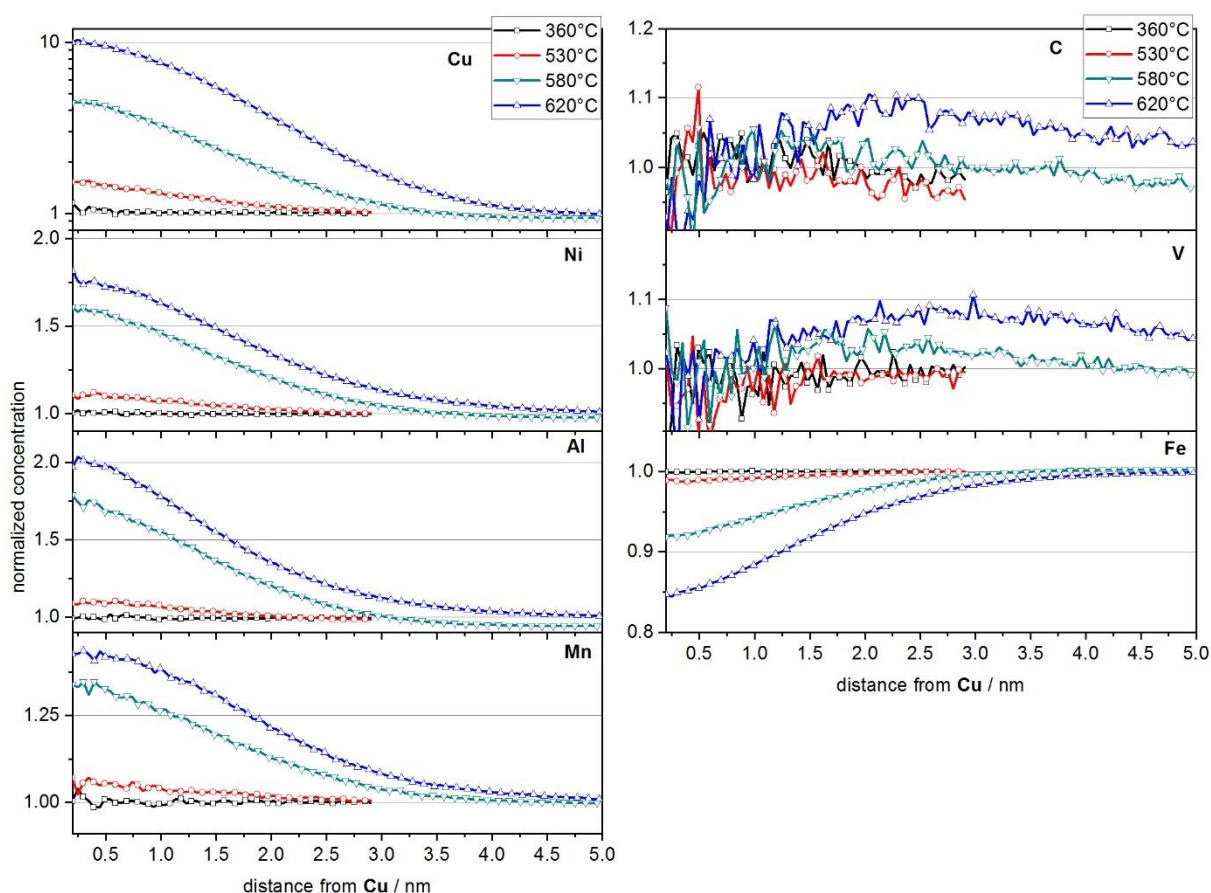


Figure 12: Radial distribution functions centered around Cu for continuous heating with 20 Kmin^{-1} to 360°C, 530°C, 580°C and 620°C. Note different ordinate scaling. The Cu-Cu ordinate is scaled logarithmically (**Paper IV**).

The precipitation reactions in the Co-alloyed steel were studied by means of APT and DSC. Carbon clusters or possibly the formation of transition carbides are detected at an ageing temperature of 360°C. At 610°C, both NiAl particles and secondary hardening carbides are present. The largest precipitates of both species show clear signs of heterogeneous precipitation

at martensite lath boundaries. A high particle number density of NiAl precipitates within the matrix was observed as well, similar to the observations made for the dual hardening steel (**Paper III**).

7.4 Hot tensile tests

Hot tensile tests were performed on the triple hardening steel, the hot-work tool steel and the dual hardening steel and the results are shown in Figure 13. Due to its lower alloying content, the triple hardening steel shows significant lower hot yield strength even at lower temperatures. The hot-work tool steel achieves the highest hot yield strength, however experiencing a significant drop between 620°C and 640°C. The yield strength of the dual hardening alloy shows a lower temperature dependence in this regime.

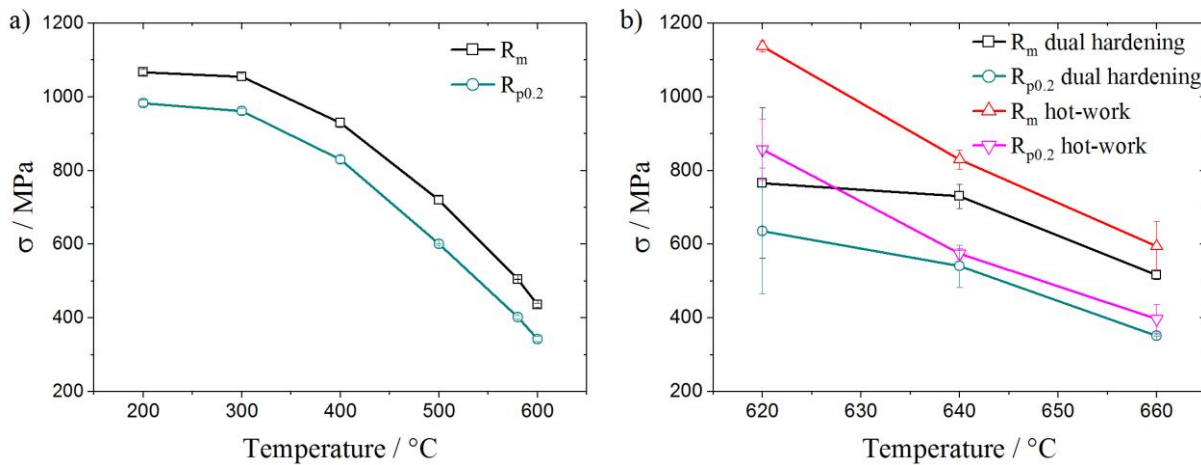


Figure 13: Hot tensile tests of a) triple hardening steel and b) dual hardening steel and hot-work tool steel.

7.5 Thermomechanical fatigue testing

As mentioned earlier, one of the main focuses of this thesis was the characterization of the resistance of a material against the thermal fatigue conditions present during pressure casting and the evaluation of a suitable test method in order to compare different alloys. According to the literature, the dominating temperature-mechanical loading conditions a tool is subjected to during pressure casting are best described by out-of-phase thermomechanical fatigue. This fatigue test setup allows for testing under reproducible and well-known loading conditions. A TMF test rig, originally designed to examine Al alloys and cast iron [31], was chosen for the performed investigations. Figure 14 shows the sample design used for the TMF testing. The specimens are fixed in water-cooled clamping devices and the temperature is measured with K-type thermocouples at three points at the surface of the specimen. Heating is performed by a high frequency induction system. The heating rate was set to 10 Ks^{-1} , as higher heating rates result in increasing undesired temperature gradients within the specimens [145]. The minimum

temperature was set to 200°C for all TMF tests, and the maximum temperature ranged from 580°C to 660°C. A phase shift of 180° between the thermal and mechanical loading was used, as is shown in Figure 15 (**Paper III**). The constraint factor K_{TM} (see Equation 2) was altered in order to achieve the same strain amplitude of 0.3% for each test, independent of the maximum test temperature, and varied between -0.83 and -0.95 . An initial parameter study was performed on the triple hardening steel. The main findings have been published elsewhere [30]. An additional borehole in the center was used to place a central thermocouple and measure the radial temperature distribution. However, as no significant radial temperature deviations were detected, the additional borehole and thermocouple were not applied at the TMF tests of the dual hardening steel, hot-work steel and Co-alloyed steel. The fatigue tests show the highest plastic compression within the first cycle. At testing temperatures equivalent to the ageing temperature of the triple hardening steel, a stable behavior is observed, whereas significant cyclic softening occurs if the maximum test temperature is increased from 580°C to 600°C. Solution annealed samples of the triple hardening steel show a rapid age hardening response during the starting procedure. The crack formation is assisted by the surface oxidation, and intercrystalline crack propagation is unaffected by nonmetallic MnS or TiN inclusions. The surface crack network forms as an arrangement of parallel cracks oriented perpendicular to the mechanical loading condition, which is caused by the one-dimensional constraint of the thermal expansion [30].

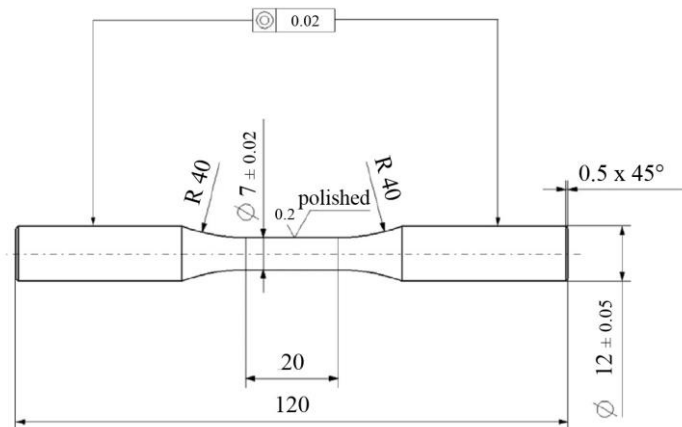


Figure 14: Geometry of TMF samples, dimensions in mm (**Paper III**).

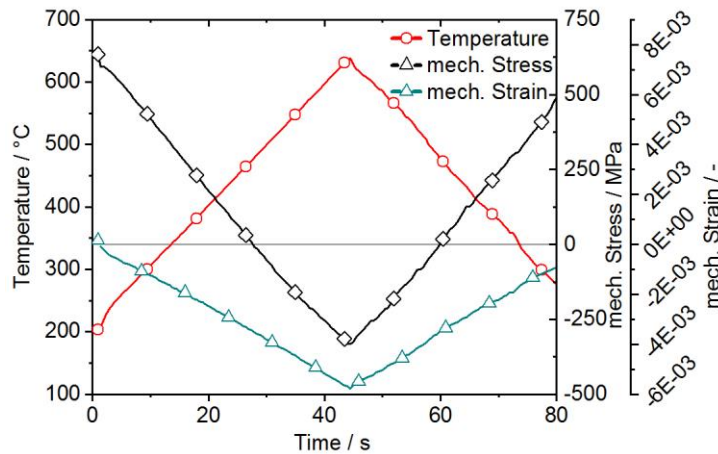


Figure 15: Course of the temperature as well as mechanical strain and stress during OP-TMF testing. A phase shift of 180° between thermal and mechanical loading was used (**Paper III**).

TMF tests performed at 580°C and 600°C on the hot-work tool steel lead to no plastic deformation due to the alloys high hot yield strength, and thus lifetimes exceeding 10^6 cycles. For all alloys except the triple hardening steel, the maximum test temperature was hence set to 620°C , 640°C and 660°C , which unfortunately led to a reduced precision of the temperature distribution. The hot-work tool steel reaches a higher stress amplitude in the first cycles, which is attributed to its higher hot yield strength at 620°C . However, the dual hardening alloy shows a decreased amount of softening, assumed to be caused by its increased tempering resistance, and reaches a higher lifetime. The stress evolution of three exemplary fatigue tests is shown in Figure 16. These findings are discussed in detail in **Paper III**.

The investigated alloys show a high dependence of the TMF lifetime on the maximum test temperature in the range between 620°C and 660°C . As mentioned before, these alloys show no plastic strain amplitude at maximum test temperatures of 600°C , up to a constraint factor K_{TM} of -1 (100% of the thermal expansion is mechanically suppressed). Figure 17 shows the dependence of the lifetime on the maximum test temperature between 620°C and 660°C . The results are obtained with a constant strain amplitude of 0.3%, which was achieved by an alternation in the constraint factor K_{TM} as mentioned before. Thus, the reduced lifetime is assumed to be caused by the increasing thermal softening. At temperatures below 620°C , the hot-work tool steel achieves the highest lifetime. However, at increasing test temperatures, the hot-work tool steel shows the most severe drop in lifetime and is subsequently surpassed by the dual hardening alloy. This is attributed to the increased tempering resistance of the dual hardening alloy, which will be described in more detail in chapter 7.6. It is furthermore interesting to note that the Co-alloyed steel achieves the shortest lifetimes, but experiences the most significant reduction in lifetime between 640°C and 660°C in contrast to the hot-work tool steel and dual hardening steel, which show the most severe drop between 620°C and 640°C . Especially at increased temperatures, no clear trend of the influence of the performed annealing temperature on the TMF lifetime can be determined.

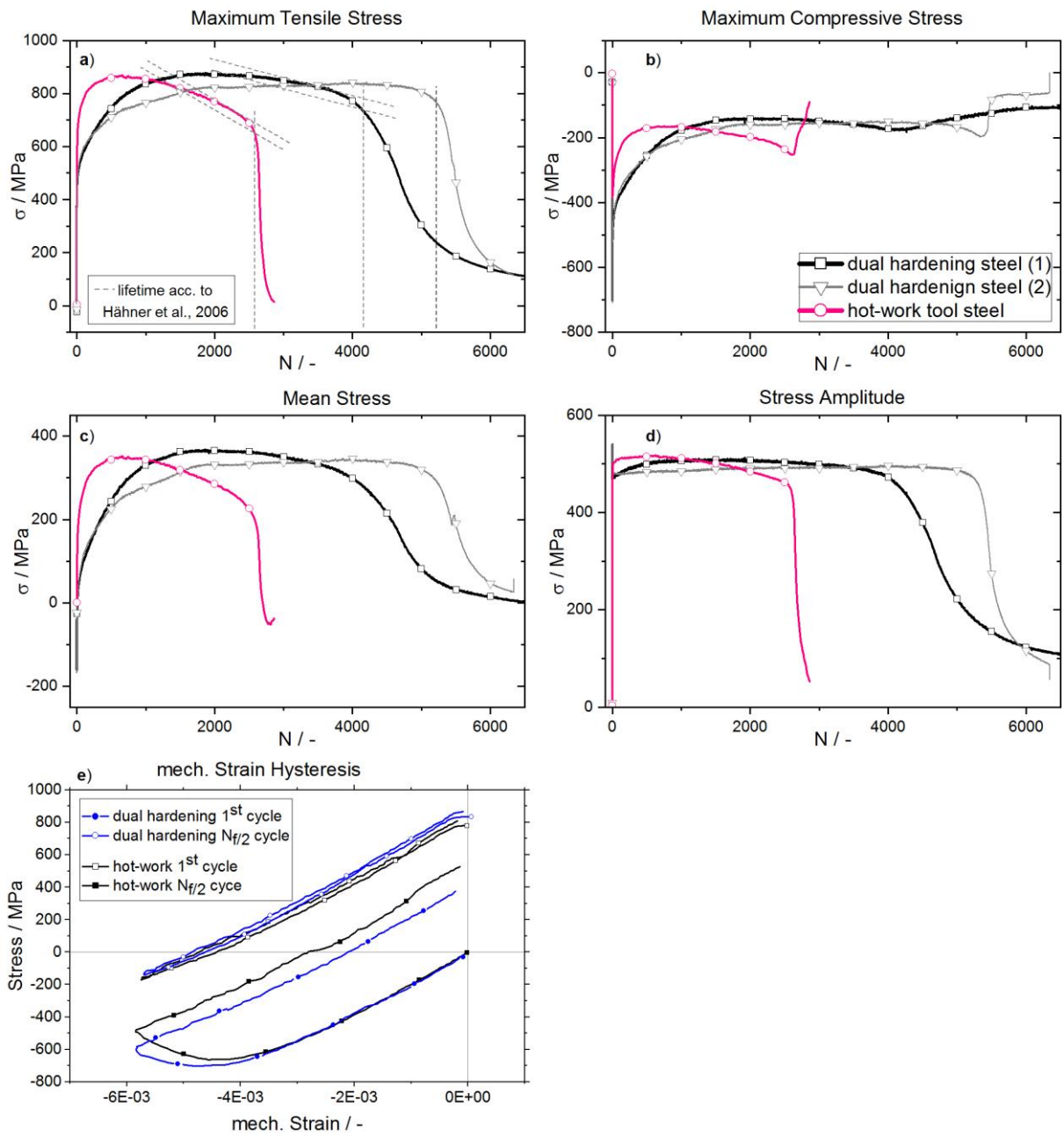


Figure 16: Development of stresses during OP-TMF testing at a T_{\max} of 640°C. a) Maximum tensile stress, b) maximum compressive stress, c) mean stress, and d) stress amplitude of each cycle. e) Mechanical stress-strain hysteresis loop for the first and $N_{f/2}$ cycle of the TMF tests of the dual ahrdening steel and hot-worwk tool steel (adapted from **Paper III**).

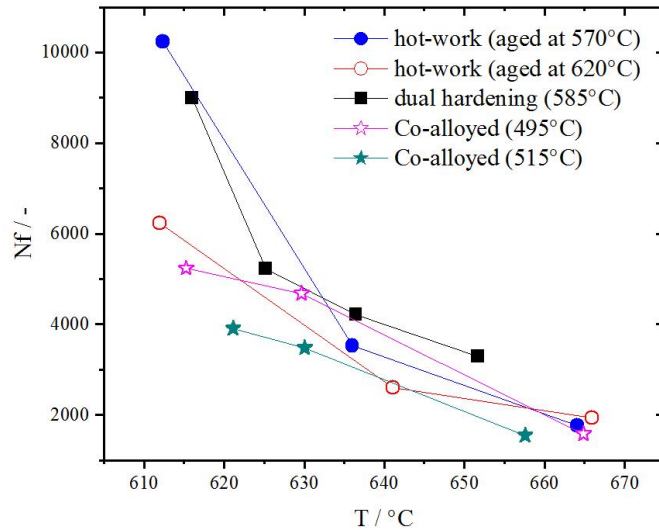


Figure 17: TMF lifetime of investigated hot-work and dual hardening steels as function of the mean maximum test temperature.

Furthermore, additional zero-stress thermal cycling ($K_{TM} = 0$) was performed with the same test rig for the same number of cycles as the respective TMF tests at the same temperatures (9189 cycles for the dual hardening steel and 10305 cycles for the hot-work tool steel). The measured hardness distribution along the longitudinal specimen axis is shown in Figure 18 and compared to the hardness distribution of the TMF tested samples. The hardness values are relativized by the initial hardness after heat treatment (655 HV1 for the hot-work tool steel and 620 HV1 for the dual hardening steel). The differences between the dual hardening steel zero-stress and TMF between 7 mm and 15 mm can be attributed to deviations in the temperature distribution during the testing and the plastic deformation. The differences at zero distance are well within the scatter of the initial hardness after the conducted heat treatment. It is concluded that the superimposed mechanical strain amplitude has no influence on the softening of the investigated alloys.

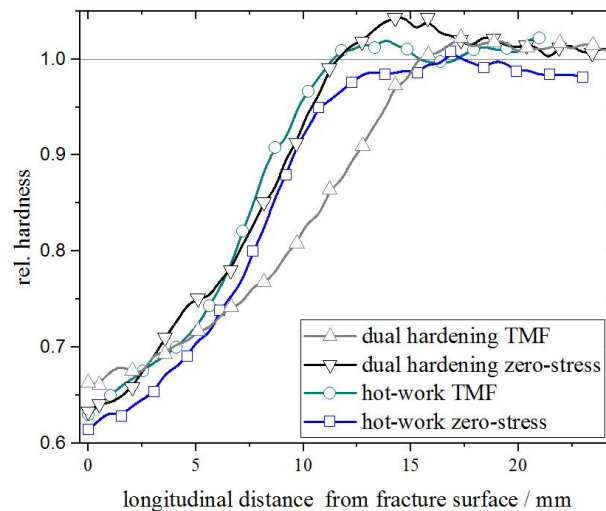


Figure 18: Hardness distribution, relativized by the initial hardness after heat treatment, along longitudinal axis of TMF specimens and zero-stress thermally cycled specimens.

Several simplifications are made by the used TMF test setup. Firstly, the influences of the coefficient of thermal expansion and thermal conductivity are neglected as no temperature gradients are used. Secondly, the oxidation behavior differs from that during a real casting processes. From microstructural investigations, it is obvious that the entire crack surface is oxidized and fatigue cracks preferentially nucleate underneath thick oxide layers. The sequence of formation is not entirely clear, however assumed to occur as follows: during the heating step, the specimen surface is covered by an oxide layer in the thickness of a view nm, thus, the occurrence of annealing colors can be seen. The plastic deformation causes the formation of fine surface cracks, which lead to locally increased strains in distinct locations close to the crack. The higher strains result in a cracking of the brittle oxide layer, allowing for more oxygen to react with the iron surface. Thus, the thick oxide layer forms in the patterns observed in Figure 19 (**Paper III**). The magnitude of the influence of different oxidation behaviors on the TMF lifetime and performance under real pressure casting conditions can, at this stage, not be clearly distinguished.

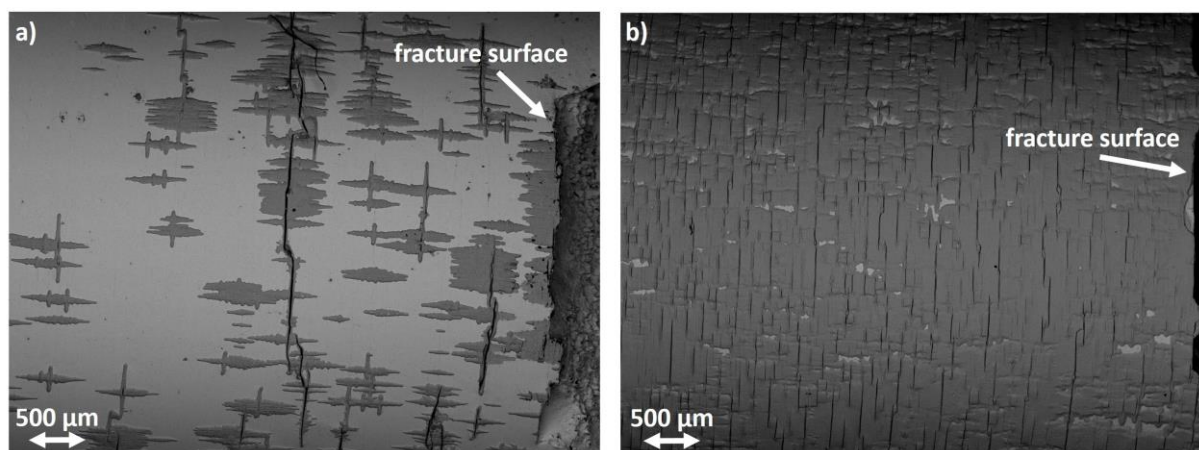


Figure 19: Back-scattered SEM micrograph of the specimen surface of a) dual hardening steel and b) hot-work tool steel after TMF testing. In proximity to large fatigue cracks, a thick oxide layer has formed (**Paper III**).

7.6 Impact of thermomechanical fatigue on the nanostructure

The following conclusions and mainly unpublished results of the impact of the TMF testing on the nanostructure are intended to be published in an additional publication in a SCI journal.

The TMF testing has a significant impact on the alloys nanostructures. The microstructure consists of high annealed and deformed martensite, dependent on the exact temperature distribution during the TMF testing. As there exist already several studies focusing on this topic, as is discussed in chapter 4.2, detailed investigations on this scale will not be part of this thesis. However, the impact on the secondary hardening precipitates is of major interest and has, until now, not been studied in detail.

At first, the influence of a superimposed mechanical strain amplitude is addressed. In order to separate the influence of the thermal and mechanical loading, zero-stress thermal cycling was performed for the same cycle numbers as the respective TMF measurements. On these zero-stress thermal cycled samples, no macroscopic material damage such as the development of a thick oxide layer or fatigue crack initiation could be observed.

APT measurements of the dual hardening alloy after TMF testing and the zero-stress thermal cycling are shown in Figures 20 and 21, respectively. It is obvious that in both conditions, the intermetallic particles as well as the secondary hardening carbides have undergone coarsening, leading to a significantly reduced particle number density. Due to the low particle number density, no quantification of the size distribution or particle number density from the APT and TEM measurements is possible, and will thus not be attempted. The detected spherical carbides in both conditions are mostly VC, which are known to possess good thermal stability [86]. The carbide shown in Figure 21 after the zero-stress thermal cycling exhibits variations in the Mo, V and C content, which is depicted in the concentration profile along the z-axis of the cylinder in Figure 21 d). It is assumed that this carbon enrichment consists of merged VC and Mo₂C carbides. The intermetallic NiAl particles possess a reduced solvus temperature and lower differences between the precipitate and matrix concentration of Ni and Al compared to the VC carbides. These facts should, according to the LSW-theory, lead to more rapid coarsening rates of the NiAl precipitates [63, 64]. It is, thus, interesting to note that the NiAl particles are present in similar particle number densities and size ranges as the VC carbides.

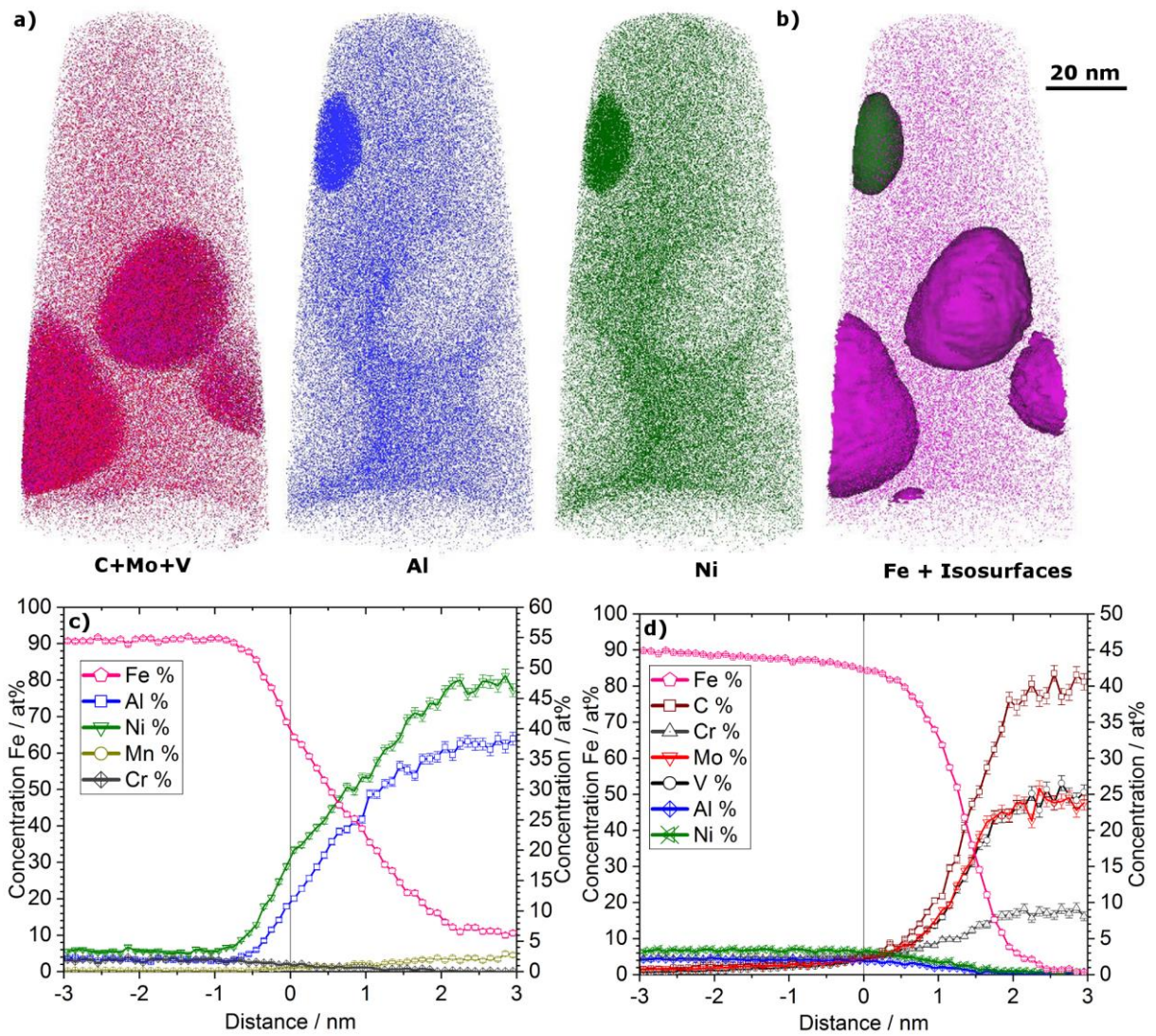


Figure 20: APT measurement of the dual hardening alloy TMF tested at 640°C. a) From left to right: atom maps of (C + Mo + V), Al and Ni. b) Isoconcentration surfaces of 25 at% (Ni + Al) in green and 5 at% (Mo + V) in pink. c) Proximity histogram according to (Ni + Al) isosurface. d) Proximity histogram according to (Mo + V) isosurfaces. Zero distances on the abscissa corresponds to the precipitate/ matrix interface; positive values are inside the precipitate (Paper III).

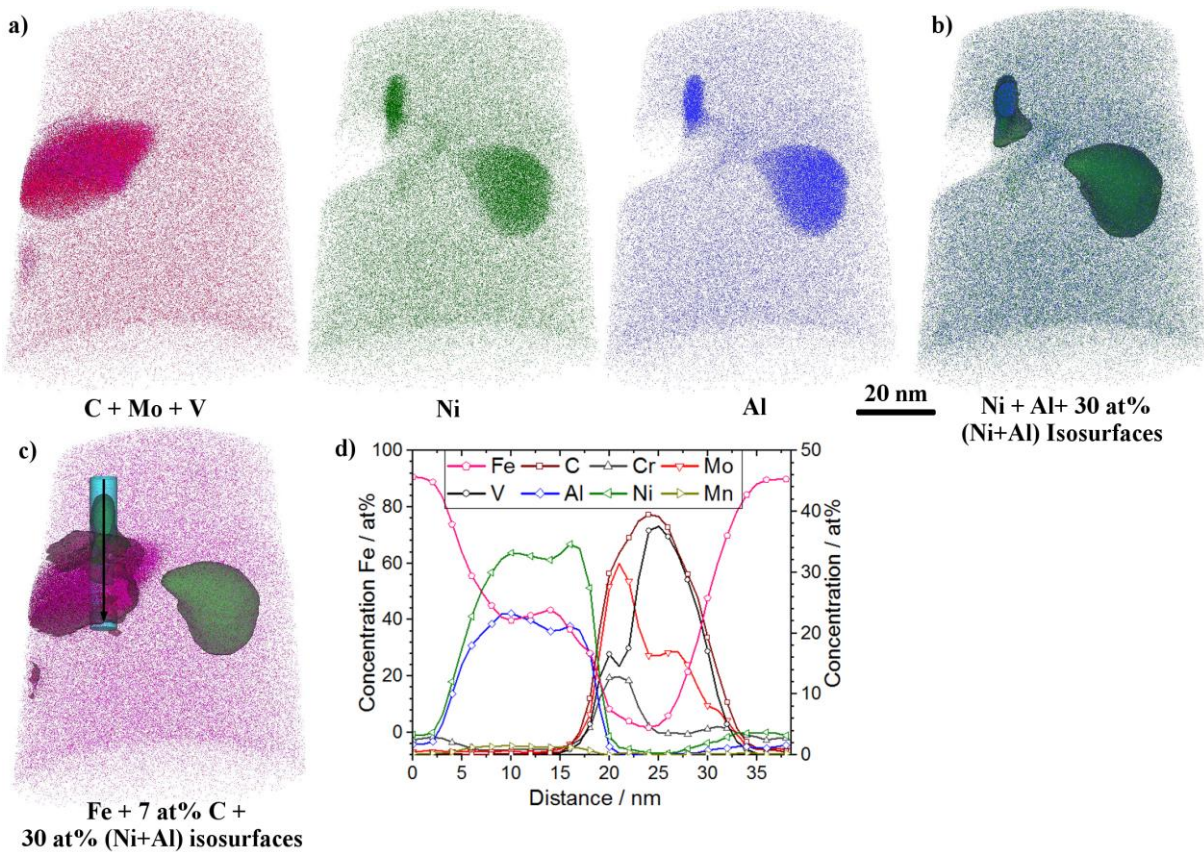


Figure 21: APT reconstruction of dual hardening steel after zero-stress thermal cycling. a) From left to right: atom maps of (C + Mo + V), Ni and Al. b) Atom map of Ni and Al, isosurfaces of 30 at% (Ni + Al) in green. c) Fe atom map, isosurfaces of 30 at% (Ni + Al) in green and 7 at% C in wine red. d) Concentration profile along the cylinder depicted in c) with a volume of $7 \times 7 \times 38 \text{ nm}^3$.

TEM investigations performed in the TMF tested and zero-stress thermal cycled conditions are shown in Figure 22. The TEM micrographs reveal a martensitic microstructure with a high dislocation density in both conditions. Furthermore, a small amount of coarse carbides is visible. Due to their cigar like morphology, these carbides are believed to be Mo_2C [83]. Higher magnifications reveal spherical particles in a size range of a few tens of nm homogeneously distributed in the matrix, which can be seen interacting with the dislocations. Correlating the TEM observations with the APT measurements in Figures 20 and 21, it is clear that the spherical particles mark NiAl precipitates and VC carbides.

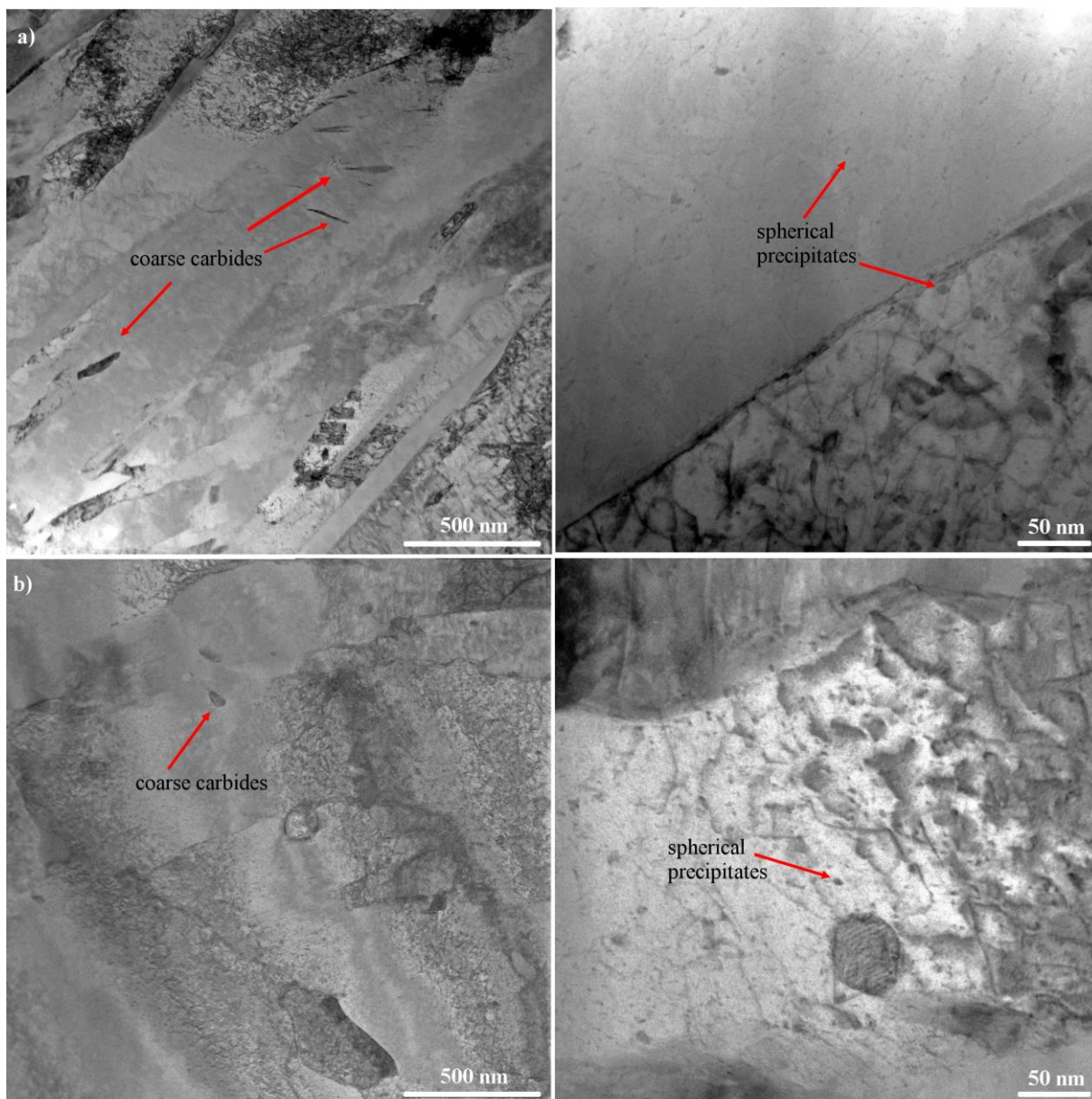


Figure 22: TEM micrographs of the dual hardening alloy. a) TMF tested and b) zero-stress thermal cycled. In both conditions, a martensitic microstructure and coarse carbides are visible. The micrographs on the right reveal spherical particles in a size range of a few tens of nm.

From the performed APT measurements, the evolution of the chemical composition of the matrix as a function of the maximum TMF testing temperature and in the zero-stress thermal cycled condition was determined and is shown in Figure 23. The matrix C content shows a decrease from the heat treated to the TMF tested conditions, which is independent of the maximum test temperature, whereas the contents of the carbide forming elements Cr, Mo and V stay constant. This indicates that the carbides undergo coarsening and an equilibrium is reached already at 620°C. In contrast, the Al and Ni contents rise with increasing test temperature, which is a clear sign that the NiAl particles not only coarsen, as is visible in Figure 20, but NiAl particles are also dissolved during the high temperature regime of the TMF

cycle. Thermodynamic calculations with MatCalc 6 ME_Fe1.2 calculated a solvus temperature of the NiAl in the dual hardening alloy of 632°C, whilst literature claims thermal stable NiAl precipitates at ageing temperatures of up to 620°C [87]. However, the solvus temperature of small NiAl particles is reduced compared to the equilibrium condition [67] due to the Gibbs-Thompson effect. This might lead to the partial dissolution of small NiAl precipitates, whilst large particles undergo Ostwald ripening and remain stable up to the maximum TMF test temperatures of 660°C.

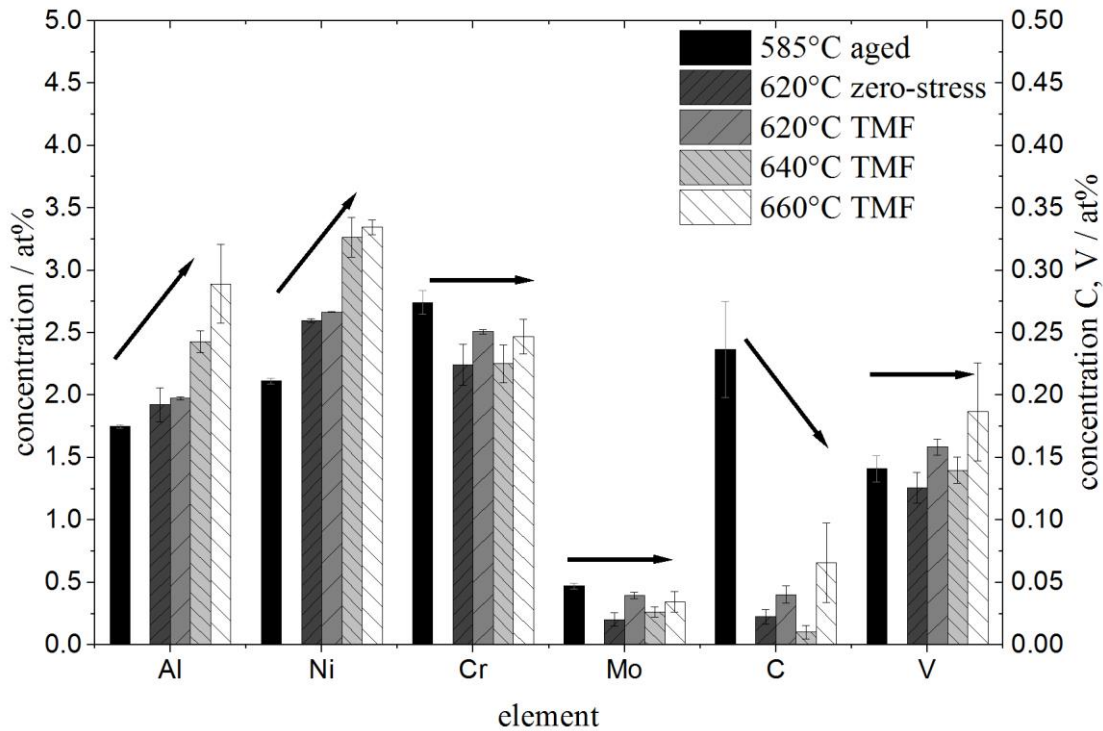


Figure 23: Matrix concentration of alloying elements in the dual hardening steel in the heat treated condition and dependent on the maximum TMF test temperature as obtained by the APT measurements. The error bars indicate the standard deviation between at least three individual APT measurements.

From the high resolution analysis, no influence of a superimposed mechanical strain amplitude on the Ostwald ripening or dissolution of precipitates can be observed. The hardness measurements on TMF tested and zero-stress thermal cycled samples depicted in Figure 18 show no influence on the softening. It is therefore concluded that the mechanical strain amplitude has no influence on the coarsening or dissolution of the secondary hardening precipitates and correlated softening under the applied TMF conditions. The zero-stress thermal cycling leads to no mechanical damaging of the samples, and thus no fatigue. The fatigue crack initiation, caused by the mechanical loading is, however, accelerated through the thermally caused softening.

The results show that the coarsening behavior of the NiAl particles under the TMF loading conditions is overestimated by classical theory. Considering the equations described previously in chapter 4.3, the small average particle radius, high solubility of Ni and Al in the iron matrix

and the lower solvus temperature compared to the secondary hardening carbides indicate the intermetallic precipitates as the precipitate phase experiencing more rapid coarsening rates. The experimental results contradict these expectations. Two possible explanations are attempted in the following: The NiAl exhibit a reduced interfacial energy, and thus have a reduced driving force for the coarsening process due to their coherence to the iron matrix. The growth and coarsening of the NiAl is furthermore retarded by the presence of carbides [122]. In the same way, the presence of NiAl particles leads to a size refinement of the secondary hardening carbides, and thus decelerates the carbide coarsening rate in the dual hardening alloy [83, 122, 126].

The second theory assumes that due to the cyclic thermal loading, the NiAl precipitates undergo coarsening at intermediate temperatures and during the upper end of the temperature cycle are subject to dissolution as described in chapter 4.3.5. As the temperature decreases again, this results in a supersaturated solid solution. The NiAl are known to experience very rapid precipitation kinetics in Fe [96]. Thus, possibly a dynamic equilibrium between coarsening, dissolution and re-precipitation could be present, which results in the small NiAl particles visible in Figures 20 and 21 and seemingly retarded coarsening rate.

The hot-work tool steel after TMF testing and after the zero-stress thermal cycling is shown in Figures 24 and 25, respectively. The secondary hardening carbides have undergone coarsening as well. The carbides contain a high core Fe content of up to 10 at%, whilst the enrichment in Mo indicates a Mo_2C carbide. In Figure 25, a small planar C enrichment is visible, exhibiting a high V content, and is thus assumed to be a coarsening resistant VC carbide which remains stable even though its close proximity to the coarse Mo_2C . Similar to the observations made for the dual hardening alloy, no influence of the mechanical strain amplitude on the nanostructure can be determined.

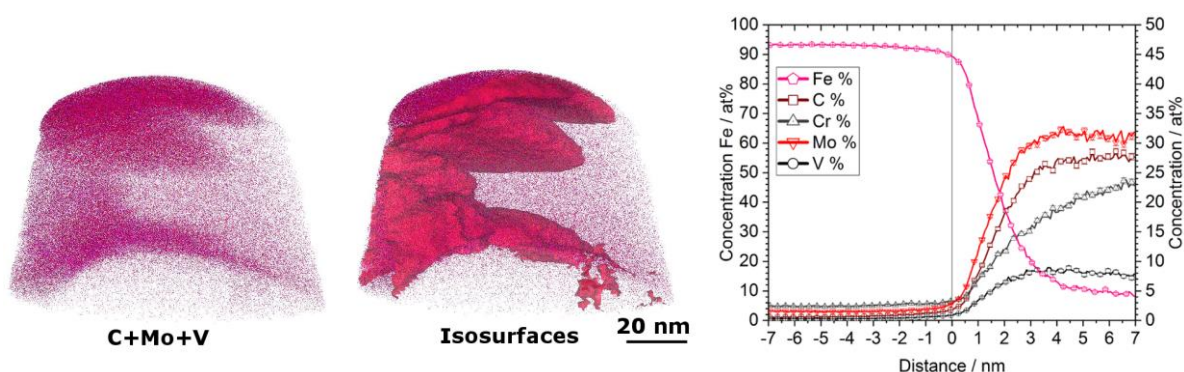


Figure 24: APT measurement of hot-work tool steel after TMF testing. From left to right: atom map of (C + Mo + V), isoconcentration surfaces of 5 at% (Mo + V), proximity histogram according to isosurfaces. Zero distance on the abscissa corresponds to the carbide/matrix interface, positive values are inside the precipitate (adapted from **Paper III**).

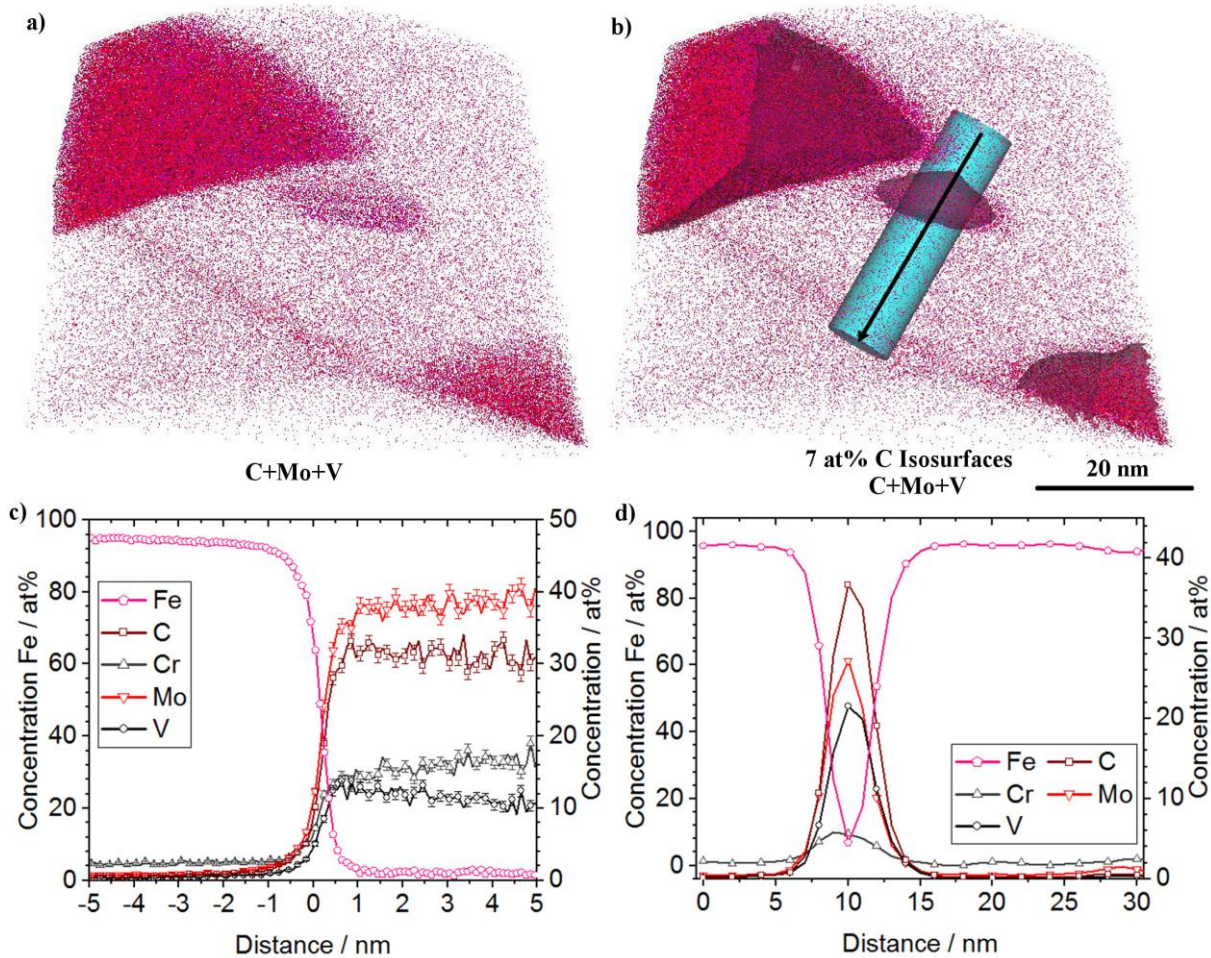


Figure 25: APT reconstruction after zero-stress thermal cycling of the hot-work tool steel. a) Atom map of (C + Mo + V). b) Isoconcentration surfaces of 7 at% C, zero distance marks the isosurface/matrix interface, positive values inside the Isosurface. c) Proximity histogram of the large Isosurface on the upper left in b). d) Concentration profile along the cylinder shown in b) with a volume of $9 \times 9 \times 30 \text{ nm}^3$.

A TEM micrograph of the hot-work steel after TMF testing is depicted in Figure 26 and shows a martensitic microstructure with a high particle number density of coarse carbides along with a $M_{23}C_6$ carbide. Due to their cigar-like shape, the carbides are suspected to be M_2C carbides in accordance to the APT measurements. Furthermore, higher magnifications reveal spherical VC carbides in a size range of a few tens of nm. Comparing the TEM micrograph of the hot-work steel to the dual hardening steel in Figure 22 reveals an increased amount of coarsened carbides, presumably Mo_2C , in the hot-work steel.

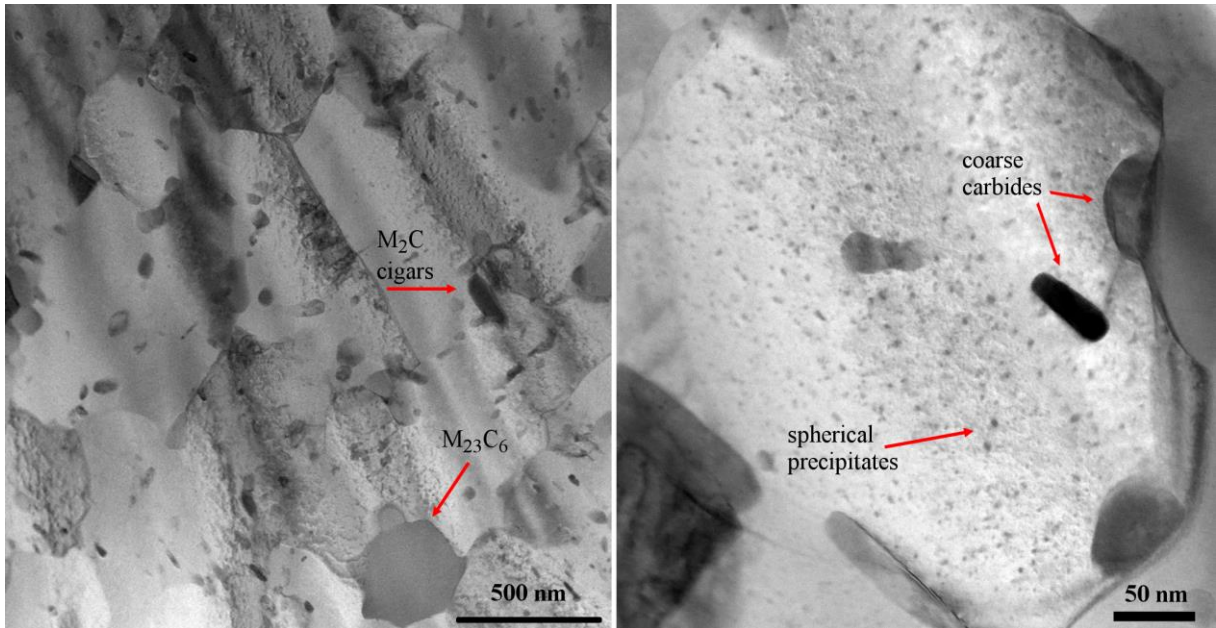


Figure 26: TEM micrographs of the hot-work tool steel after TMF testing. Besides large $M_{23}C_6$, coarse cigar shaped M_2C and spherical VC precipitates are visible.

The chemical evolution of the matrix of the hot-work tool steel is shown in Figure 27. It shows a constant decrease of the carbide forming elements C, Cr, Mo and V from the aged to the TMF tested conditions. Thus, the carbides first grow, leading to a further matrix depletion, followed by the coarsening observed by APT and TEM. The matrix concentration seems independent of the maximum TMF test temperature.

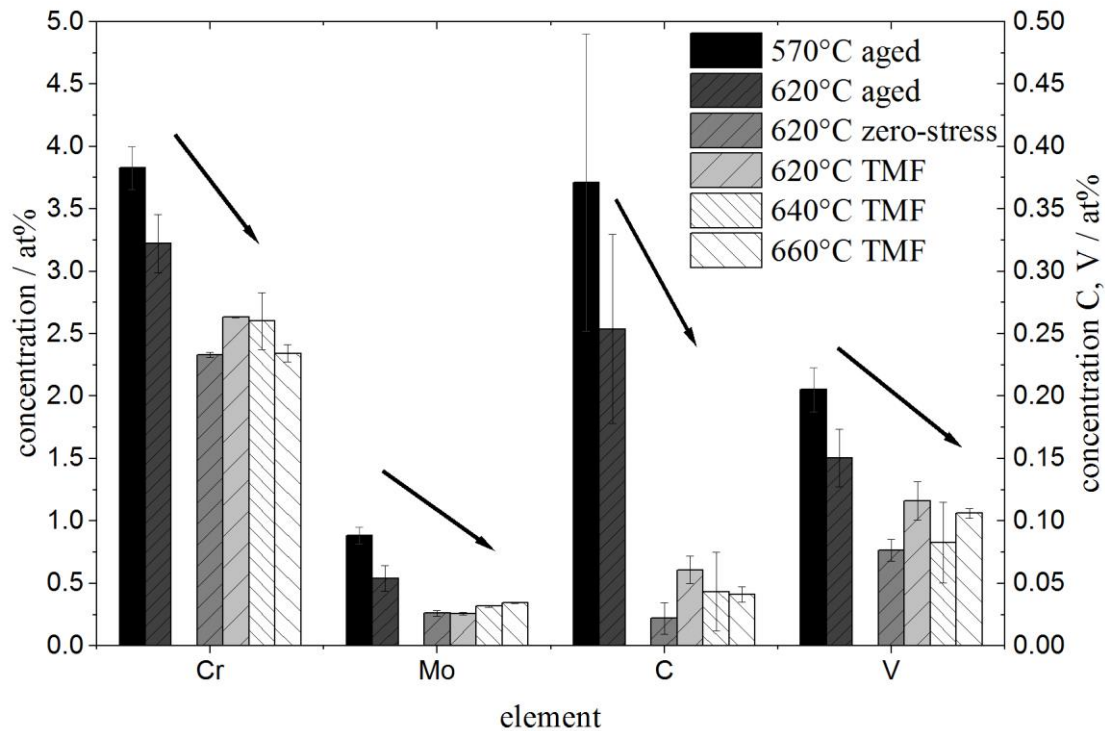


Figure 27: Matrix concentration of alloying elements in the heat treated condition and dependent on the maximum TMF test temperature as obtained by the APT measurements of the hot-work steel. The error bars indicate the standard deviation between at least three individual APT measurements.

The reduced matrix concentration of Cr, Mo and V in the heat treated condition in the dual hardening alloy compared to the hot-work tool steel is assumed to be caused by the assisted, and thus accelerated carbide precipitation in the dual hardening alloy. The associated reduced mean particle size of the secondary hardening carbides retards the carbide coarsening rate compared to the hot-work tool steel [Lifshitz and Slyozov 1961; Wagner 1961]. The higher alloying ratio of V/Mo in the dual hardening alloy is expected to be a further contributing factor to the retarded carbide coarsening rate. As a consequence, the dual hardening alloy achieves an increased tempering resistance under TMF loading conditions, and thus higher TMF lifetimes compared to the hot-work tool steel.

The Co-alloyed steel shows a different behavior, as can be seen in Figures 28 and 29. The carbides and intermetallic particles undergo coarsening as well and the matrix alloying content of the carbide forming elements reaches a constant level same as in the dual hardening steel. But whereas the matrix Al content stays approximately the same, the matrix shows a depletion of Ni after the TMF testing. This is caused by the formation of reverted austenite, which is visible in the large Ni enriched volume lacking significant amounts of Al in Figure 28. The formation of reverted austenite accelerates the dissolution of the NiAl particles [144], which leads to the decreased TMF resistance of the Co-alloyed steel compared to the dual hardening alloy as shown in Figure 17.

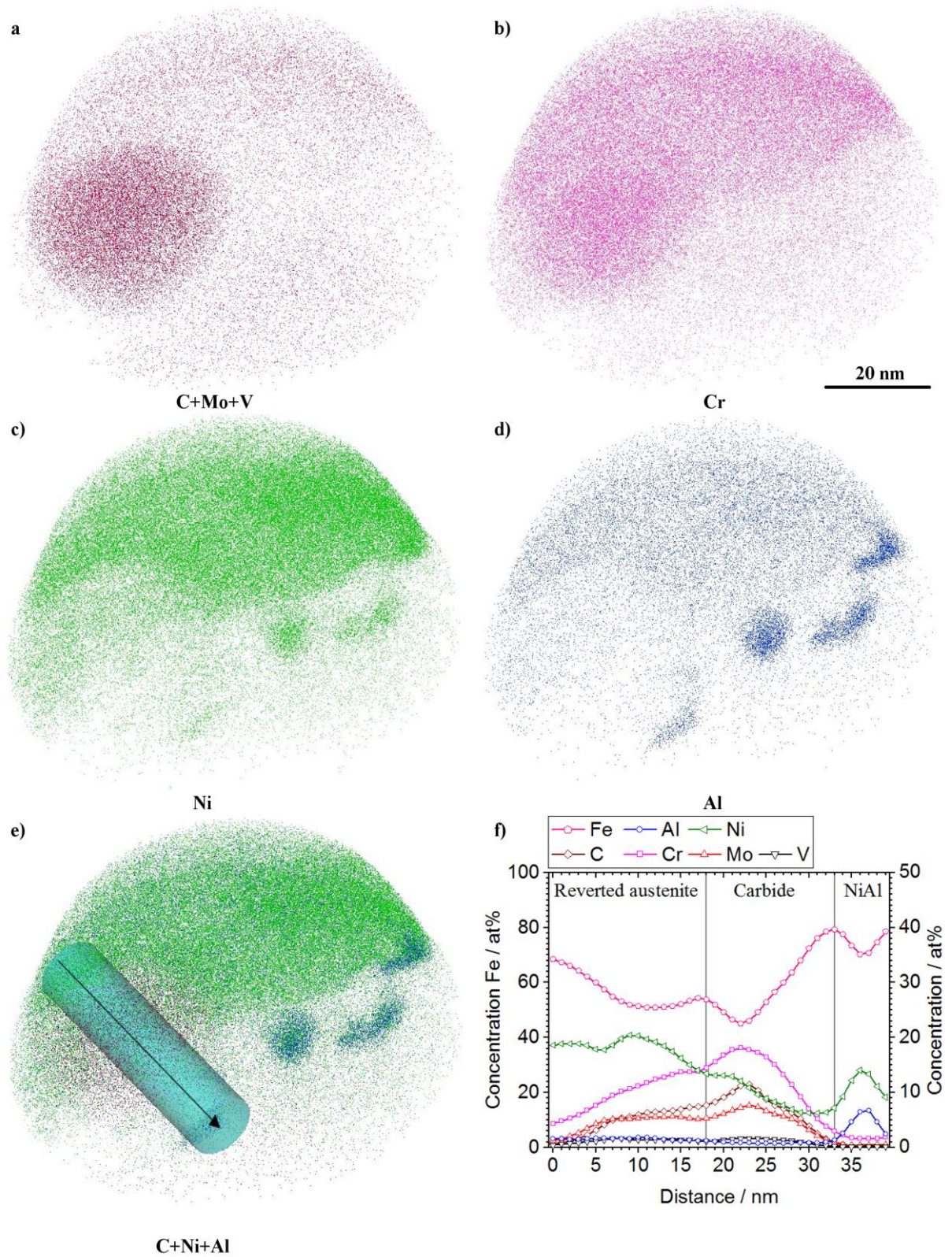


Figure 28: APT reconstruction of the Co-alloyed steel TMF tested at 620°C. Atom maps of a) (C + Mo + V), b) Cr, c) Ni and d) Al. e) Atom map of (C + Ni + Al) and cylinder ROI with a volume of 10x10x40 nm³. f) Concentration profile along the z-axis of the cylinder in b), showing the composition of the reverted austenite, carbide and NiAl particle.

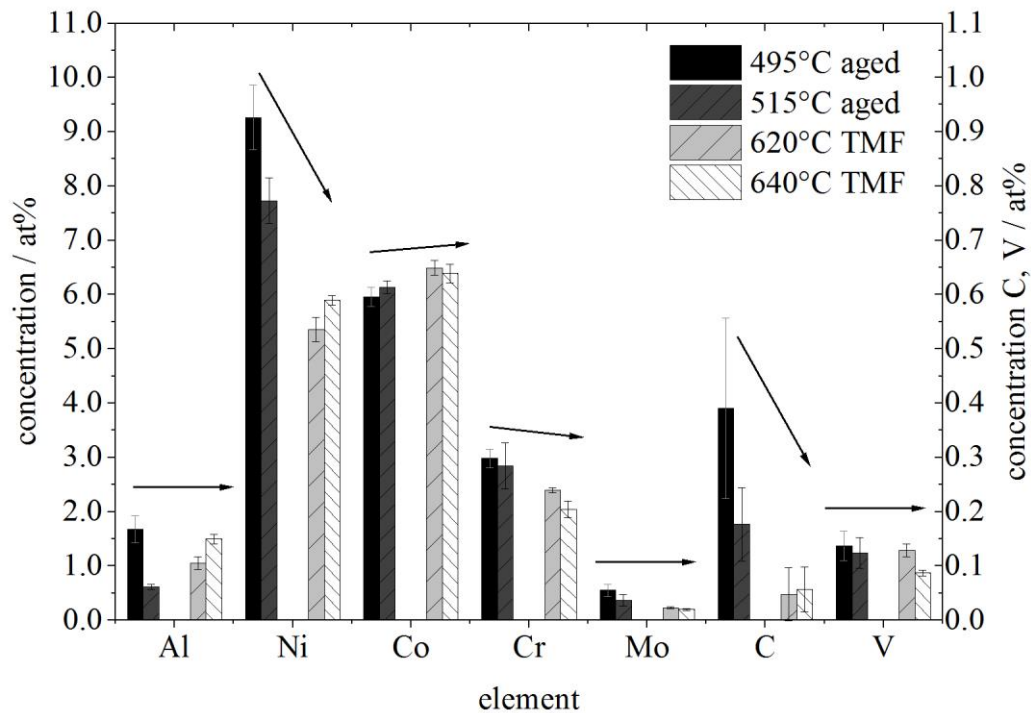


Figure 29: Matrix concentration of alloying elements of the Co-alloyed steel obtained by APT as a function of ageing temperature and maximum TMF temperature. The error bars mark the standard deviations between three individual APT measurements.

A direct comparison of the precipitates in the heat treated and TMF tested conditions between the dual hardening steel, the hot-work tool steel and the Co-alloyed steel is shown in Figure 30. Despite the NiAl being subject to partial dissolution, the dual hardening alloy achieves higher particle number densities of fine, spherical precipitates compared to the hot-work tool steel, which contains a large number of coarse cigar-shaped M_2C carbides. The higher particle number density, caused by the retarded coarsening rate described above, is assumed to be the main reason for the increased tempering resistance of the dual hardening steel. This ultimately leads to the increased TMF lifetimes in Figure 17, even though the hot-work tool steel possesses a higher hot yield strength. The observed formation of reverted austenite in the Co-alloyed steel, caused by its high Ni content, accelerates the dissolution of the intermetallic NiAl particles, and is thus assumed to lead to the lower TMF lifetime of the Co-alloyed steel shown in Figure 17.

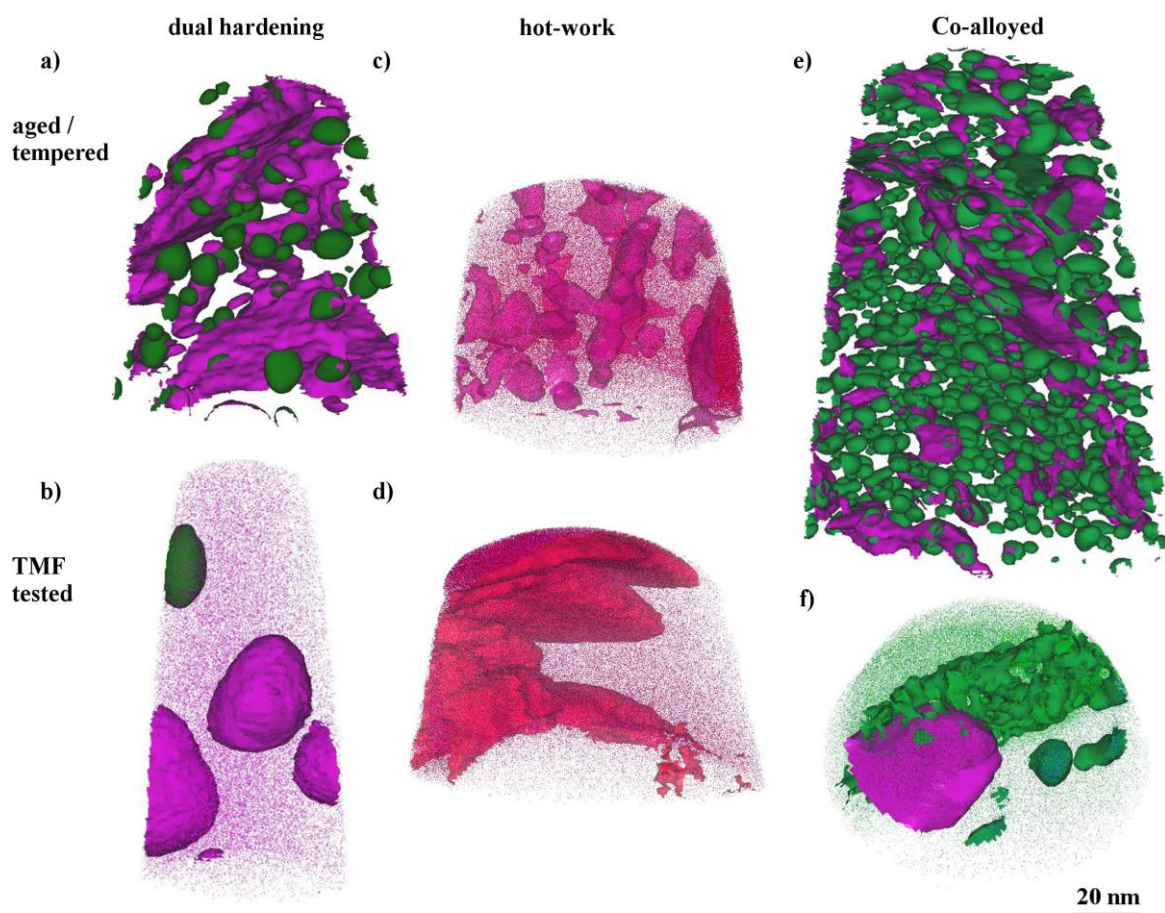


Figure 30: Comparing APT measurements of the a) dual hardening alloy heat treated and b) TMF tested, c) hot-work tool steel aged and d) TMF tested (adapted from **Paper III**) and e) Co-alloyed steel aged and f) TMF tested. In green: 25 at% (Ni + Al) isosurfaces, pink/red 5 at% (Mo + V) isosurfaces

7.7 Thermodynamic Calculations

Current dual hardening steels are limited to the use of NiAl or Cu precipitates in addition to secondary hardening carbides as strengthening particles. Thermodynamic calculations were performed with the software MatCalc in order to assess to suitability of further intermetallic phases. Most of the intermetallic phases used in maraging steels comprise of the elements Ti, V and/or Mo, which have a high affinity towards carbon. Especially Ti is known to form Ti(C,N) during the solidification process. Calculations were performed with MatCalc 6.0 and an adapted ME_Fe1.1 database. Three different maraging steels (C250, T250 and N15K10M5F5) were calculated with the addition of 0.1 wt% C, 0.2 wt% C and 0.4 wt% C. The calculations proofed that Ti-containing intermetallic phases are unsuitable for the application in dual hardening steels. However, intermetallic phases containing Mo and V (such as μ -Phase and Laves-Phase) show promising results when the carbon content does not exceed 0.1-0.2 wt%.

Calculations of the dual hardening alloy with different alloying ratios of Ni/Al, Cr/Mo/V and variations of the Si and Mn content yielded following results:

- The alloy contains B2-NiAl, MC, M_6C and $M_{23}C_6$ carbides as well as metastable Mo_2C .
- Mn is preferentially incorporated in the NiAl precipitates. The solvus temperature of the NiAl is increased by additional alloying with Mn and Si to up to 650°C. Substitution of Al by up to 3 at% Mn does not lead to the formation of NiMn.
- A reduction of the carbon content and the substitution of parts of V with Cr or Mo leads to the highest reduction of the VC solvus temperature, increasing the temperature regime suitable for the solution annealing process.
- The equilibrium calculations prefer the formation of Laves-phase versus Mo_2C . However, no Laves-phase has been detected in the dual hardening steel, which is why it is assumed that Mo_2C experience faster precipitation kinetics, and are thus the preferentially formed precipitate phase.

8 Outlook and open questions

During this thesis, a comprehensive study of the micro- and nanostructure and its evolution of dual hardening steels was performed. The characterization and recreation of the load profile present during pressure die casting was achieved via the use of a thermomechanical fatigue test rig, and the influence of these loading conditions on the nanostructure was revealed. Overall, the dual hardening alloying concept shows promising results concerning the implementation in hot-work applications. Although many issues were addressed and solved in this thesis and the appended papers, a number of open questions remains to be tackled by future researchers.

During the thermomechanical fatigue testing, the intermetallic phases show a decreased amount of Ostwald ripening compared to the secondary hardening carbides, but an increased amount of dissolution with increasing maximum temperatures. How these mechanisms exactly contribute to the dual hardening steels improved tempering resistance remains partially unclear. Further fatigue tests could possibly shed some light on the coarsening and dissolution kinetics as well as possible differences in the softening rate between the dual hardening steel and hot-work tool steel as well as between TMF and the zero-stress thermally cycled specimens, and thus help to determine possible effects of the mechanical strain amplitude on coarsening rates.

Thermodynamic calculations showed that slight variations in the chemical composition of the dual hardening steel are able to increase the solvus temperature of the intermetallic NiAl particles, which is expected to further increase the dual hardening steels tempering resistance, and thus the thermomechanical fatigue lifetime. The addition of low amounts of Si and Mn is able to increase the NiAl solvus temperature to up to 650°C. Higher alloying contents of C and V are not recommended due to the increasing austenitization temperature needed to dissolve sufficient amounts of VC carbides.

In the utilized thermomechanical fatigue test setup, the dual hardening alloy achieved increased lifetimes due to its increased tempering resistance. However, several other mechanisms possibly contribute to the lifetime. One of these is the difference in the oxidation behavior. Under real service conditions, the formation of intermetallic phases between the tool material and liquid metal is known to be a contributing factor, which can be influenced by the alloy composition of the tool. To study and possibly mitigate the influence of sample and crack surface oxidation on the thermomechanical fatigue lifetime, testing under inert gas atmosphere could generate further insights and understanding in this aspect. In the case of the highest maximum temperatures, increasing longitudinal temperature deviations were observed. These had a significant influence on the cyclic softening behavior, even if these variations were as small as $\pm 5^\circ\text{C}$, which is well within the boundaries suggested by Hähner et al. [145]. In the case of the highest temperatures of 660°C, the optimization of the induction coil geometry or test setup might improve the reproducibility of future thermomechanical fatigue tests of hot-work tool steels and dual hardening steels.

Furthermore, the coefficient of thermal expansion and thermal conductivity are neglected in the test setup but have a major influence on the development of thermal stresses, and thus fatigue lifetime. Future studies should therefore include the determination and comparison of these properties.

9 Novel features

The following points are believed to be the novel findings of this thesis and the main contributions to the field of research:

- The precipitation sequence in the investigated dual hardening steels is decoded. During continuous heating, the precipitation reactions are Cu-VC-(NiAl) and NiAl-VC in the absence of Cu. Heterogeneous precipitation of the secondary hardening carbides is evident at interfaces between the metallic/intermetallic particles and the iron matrix.
- The thermal and mechanical load profile present during pressure die casting can be recreated with the utilized thermomechanical fatigue test rig. The exact test temperature and its distribution have the greatest influence on the material behavior and achieved lifetime under the thermomechanical fatigue loading conditions. The most severe plastic deformation occurs in the first cycle. Plastic compression during the heating step leads to a continuous shift of the mean stress into the tensile region. The thermomechanical fatigue testing leads to the formation of a fatigue crack network and sample failure.
- During thermomechanical fatigue testing, the secondary hardening particles undergo coarsening and partial dissolution. The coarsening rate of the NiAl particles is overestimated by classical theory. The dual hardening steel possesses an increased particle number density of secondary hardening precipitates compared to the hot-work tool steel. This is true in the heat treated state as well as after the thermomechanical fatigue testing. The dual hardening alloy, thus, achieves increased lifetimes under thermomechanical loading conditions compared to the hot-work tool steel due to its increased tempering resistance. The retained austenite formed in the Co-alloyed steel accelerates the dissolution of the NiAl precipitates and leads to the Co-alloyed steels reduced lifetime under thermomechanical loading conditions.
- During the performed thermomechanical fatigue testing, the thermal loading causes the overageing and dissolution of the precipitates; a superimposed mechanical strain amplitude does have no influence. The mechanical loading causes the fatigue crack initiation and growth, which is accelerated by the thermally caused Ostwald ripening of the secondary hardening precipitates and correlated softening.

10 References

- [1] I. Siller, Temperaturwechselprüfung von Warmarbeitsstählen mittels gepulster Laserstrahlung. Dissertation, Leoben, 2003.
- [2] G.A. Roberts, G. Krauss, R. Kennedy, Tool steels, fifth. ed., ASM International, Materials Park, OH, 2010.
- [3] D.A. Spera, D.F. Mowbray, Thermal Fatigue of Materials and Components, ASTM International, West Conshohocken, PA, 1976.
- [4] J.R. Davis, Tool materials, first print, ASM International, Materials Park, Ohio, 1995.
- [5] K.J. Handerhan, W.M. Garrison, N.R. Moody, A comparison of the fracture behavior of two heats of the secondary hardening steel AF1410, *Metallurgical Transactions A* 20 (1989) 105–123.
- [6] W.M. Garrison, R. Strychor, A preliminary study of the influence of separate and combined aluminum and nickel additions on the properties of a secondary hardening steel, *Metallurgical Transactions A* 19 (1988) 3103–3107.
- [7] W.M. Garrison, M.S. Bhat, An approach to developing an alternative hot work die steel, *MTA* 19 (1988) 1751–1760.
- [8] D. Delagnes, F. Pettinari-Sturmel, M.H. Mathon, R. Danoix, F. Danoix, C. Bellot, P. Lamesle, A. Grellier, Cementite-free martensitic steels: A new route to develop high strength/high toughness grades by modifying the conventional precipitation sequence during tempering, *Acta Materialia* 60 (2012) 5877–5888.
- [9] R. Bürgel, H.J. Maier, T. Niendorf, Zyklische Festigkeit und Verformung, in: H.J. Maier, T. Niendorf, R. Bürgel (Eds.), *Handbuch Hochtemperatur-Werkstofftechnik*, Springer Fachmedien Wiesbaden, Wiesbaden, 2015, pp. 189–243.
- [10] M. Spittel, T. Spittel, Mechanical and physical properties of alloys and metals, in: M. Spittel, T. Spittel, H. Warlimont, H. Landolt, R. Börnstein, W. Martienssen (Eds.), *Numerical data and functional relationships in science and technology: New series*, Springer, Berlin, 2016, pp. 87–113.
- [11] P. Beiss, Iron and steel: Thermophysical properties, in: P. Beiss, V. Behrens, H. Landolt, R. Börnstein, W. Martienssen, O. Madelung (Eds.), *Numerical data and functional relationships in science and technology: New series*, Electronic version, Springer, Berlin, 2003, pp. 448–459.
- [12] J. Sjöström, J. Bergström, Thermal fatigue in hot-working tools, *Scandinavian Journal of Metallurgy* 34 (2005) 221–231.
- [13] L.-Å. Norström, M. Svensson, N. Öhrberg, Thermal-fatigue behaviour of hot-work tool steels, *Metals Technology* 8 (1981) 376–381.
- [14] R. Ebner, S. Marsoner, I. Siller, W. Ecker, Thermal fatigue behaviour of hot-work tool steels: Heat check nucleation and growth, *International Journal of Microstructure and Materials Properties* 3 (2008) 182.

- [15] Q. Zhou, X. Wu, N. Min, Y. Min, Effect of Si on thermal fatigue of SDH3 hot work die steel, in: ASMET (Ed.), Tool 2012, ASMET - The Austrian Society for Metallurgy and Materials, Leoben, 2012, pp. 365–373.
- [16] D. Delagnes, F. Rézaï-Aria, C. Levallant, A. Grellier, Influence of temperature and initial hardness on fatigue behaviour and life of a 5%Cr hot work tool steel, in: F. Jeglitsch (Ed.), Tool steels in the next century: Proceedings of the 5th International Conference on Tooling, September 29th - October 1st, 1999, University of Leoben, Leoben, Austria, Inst. für Metallkunde und Werkstoffprüfung Montanuniversität Leoben, Leoben, 1999.
- [17] J. Bergström, F. Rézaï-Aria, High temperature fatigue of tool steels, in: M. Rosso (Ed.), Tooling materials and their applications from research to market: Proceedings of 7th International Tooling Conference; Politecnico di Torino, Torino, Italy, 2 - 5 May 2006, Politecnico Di Torino, Torino, 2006, pp. 545–554.
- [18] D. Klobčar, J. Tušek, Thermal stresses in aluminium alloy die casting dies, *Computational Materials Science* 43 (2008) 1147–1154.
- [19] D. Klobčar, J. Tušek, B. Taljat, L. Kosec, M. Pleterski, Aging of maraging steel welds during aluminium alloy die casting, *Computational Materials Science* 44 (2008) 515–522.
- [20] D. Klobčar, J. Tušek, B. Taljat, Thermal fatigue of materials for die-casting tooling, *Materials Science and Engineering: A* 472 (2008) 198–207.
- [21] M. Salem, P. Lamesle, G. Dour, S. Le Roux, F. Rézaï-Aria, Interaction between aluminizing, oxidation and thermal fatigue in aluminium die casting tool, in: ASMET (Ed.), Tool 2012, ASMET - The Austrian Society for Metallurgy and Materials, Leoben, 2012, pp. 357–364.
- [22] F.S. Gobber, A.G. Pisa, D. Ugues, M. Rosso, Design of a Test Rig for the Characterization of Thermal Fatigue and Soldering Resistance of the Surfaces of Tool Steels for High-Pressure Die-Casting Dies, *steel research international* 272 (2019) 1900480.
- [23] A. Persson, J. Bergström, C. Burman, Evaluation of heat checking damage in die casting, in: F. Jeglitsch (Ed.), Tool steels in the next century: Proceedings of the 5th International Conference on Tooling, September 29th - October 1st, 1999, University of Leoben, Leoben, Austria, Inst. für Metallkunde und Werkstoffprüfung Montanuniversität Leoben, Leoben, 1999, pp. 167–184.
- [24] F. Medjedoub, S. Le Roux, G. Dour, F. Rézaï-Aria, Effect of local stress on the heat-checking morphology in high temperature tool steels under thermal fatigue: Transition from multi-axiality to uniaxiality, *Mechanics of Materials* 69 (2014) 159–172.
- [25] E. Paffumi, K.-F. Nilsson, Z. Szaraz, Experimental and numerical assessment of thermal fatigue in 316 austenitic steel pipes, *Engineering Failure Analysis* 47 (2015) 312–327.

-
- [26] S. Le Roux, F. Rézaï-Aria, Application of Image Analyses to Heat-Checking Characterisations under Thermal Fatigue Solicitations of High Temperature Tool Steels, in: F. Simancik (Ed.), Proceedings of the 10th International Tool Conference: TOOL, 10th International TOOL Conference 04th to 07th October 2016, Bratislava, Slovakia, ASMET - The Austrian Society for Metallurgy and Materials, Leoben, 2016, pp. 302–313.
- [27] A. Persson, S. Hogmark, J. Bergström, Simulation and evaluation of thermal fatigue cracking of hot work tool steels, *International Journal of Fatigue* 26 (2004) 1095–1107.
- [28] S. Le Roux, F. Medjedoub, G. Dour, F. Rézaï-Aria, Image analysis of microscopic crack patterns applied to thermal fatigue heat-checking of high temperature tool steels, *Micron* 44 (2013) 347–358.
- [29] V. Fantini, L. Serri, P. Bianchi, Laser thermal shock and fatigue testing system, in: L.H.J.F. Beckmann (Ed.), *Lasers in Material Processing*, SPIE, 1997, pp. 538–545.
- [30] B. Seisenbacher, M. Hofinger, G. Winter, F. Grün, Material behaviour of a dual hardening steel under thermomechanical loading, *Fatigue & Fracture of Engineering Materials & Structures* 98 (2019) 104.
- [31] M. Riedler, H. Leitner, B. Prillhofer, G. Winter, W. Eichlseder, Lifetime simulation of thermo-mechanically loaded components, *Meccanica* 42 (2007) 47–59.
- [32] M. Azadi, G.H. Farrahi, G. Winter, W. Eichlseder, Fatigue lifetime of AZ91 magnesium alloy subjected to cyclic thermal and mechanical loadings, *Materials & Design* 53 (2014) 639–644.
- [33] M. Nagasawa, K. Kubota, Y. Tamura, H. Yokoo, Prediction of life to thermal fatigue crack initiation of die casting dies, in: F. Jeglitsch (Ed.), *Tool steels in the next century: Proceedings of the 5th International Conference on Tooling*, September 29th - October 1st, 1999, University of Leoben, Leoben, Austria, Inst. für Metallkunde und Werkstoffprüfung Montanuniversität Leoben, Leoben, 1999.
- [34] S. Suresh, *Fatigue of Materials*, second ed., Cambridge University Press, Cambridge, 2012.
- [35] Y. Kadioglu, H. Sehitoglu, Thermomechanical and Isothermal Fatigue Behaviour of Bare and Coated Superalloys, *Journal of Engineering Materials and Technology* (1996) 94–102.
- [36] M. Azadi, G.H. Farrahi, G. Winter, P. Huter, W. Eichlseder, Damage prediction for uncoated and coated aluminum alloys under thermal and mechanical fatigue loadings based on a modified plastic strain energy approach, *Materials & Design* 66 (2015) 587–595.
- [37] M.D. Bambach, W. Bleck, H.S. Kramer, M. Klein, D. Eifler, T. Beck, H. Surm, H.-W. Zoch, F. Hoffmann, A. Radulescu, Tailoring the Hardening Behavior of 18CrNiMo7-6 via Cu Alloying, *steel research international* 87 (2016) 550–561.

-
- [38] F. Qayyum, M. Shah, O. Shakeel, F. Mukhtar, M. Salem, F. Rezai-Aria, Numerical simulation of thermal fatigue behavior in a cracked disc of AISI H-11 tool steel, *Engineering Failure Analysis* 62 (2016) 242–253.
- [39] F. Medjedoub, G. Dour, S. Le Roux, P. Lamesle, M. Salem, P. Hairy, F.R. Aria, Experimental conditions and environment effects on thermal fatigue damage accumulation and life of die-casting steel X38CrMoV5 (AISI H11), *International Journal of Microstructure and Materials Properties* 3 (2008) 336.
- [40] S. Le Roux, F. Medjedoub, G. Dour, F. Rézai-Aria, Role of heat-flux density and mechanical loading on the microscopic heat-checking of high temperature tool steels under thermal fatigue experiments, *International Journal of Fatigue* 51 (2013) 15–25.
- [41] A. Persson, Strain-based approach to crack growth and thermal fatigue life of hot work tool steels, *Scandinavian Journal of Metallurgy* 33 (2004) 53–64.
- [42] D. Klobčar, L. Kosec, B. Kosec, J. Tušek, Thermo fatigue cracking of die casting dies, *Engineering Failure Analysis* 20 (2012) 43–53.
- [43] J. Sjöström, J. Bergström, Thermal fatigue testing of chromium martensitic hot-work tool steel after different austenitizing treatments, *Journal of Materials Processing Technology* 153-154 (2004) 1089–1096.
- [44] D. Mellouli, N. Haddar, A. Köster, H.F. Ayedi, Thermal fatigue failure of brass die-casting dies, *Engineering Failure Analysis* 20 (2012) 137–146.
- [45] A. Nagesha, M. Valsan, R. Kannan, K. Bhanusankararao, V. Bauer, H. Christ, V. Singh, Thermomechanical fatigue evaluation and life prediction of 316L(N) stainless steel, *International Journal of Fatigue* 31 (2009) 636–643.
- [46] P. Lamesle, M. Salem, S. Le Roux, G. Dour, F.R. Aria, Oxidation and Corrosion Effects on Thermal Fatigue Behaviour of Hot Work Tool Steel X38CrMoV5 (AISI H11), *Materials Science Forum* 595-598 (2008) 789–796.
- [47] H.-J. Christ, Effect of environment on thermomechanical fatigue life, *Materials Science and Engineering: A* 468-470 (2007) 98–108.
- [48] M. Salem, S. Le Roux, G. Dour, P. Lamesle, K. Choquet, F. Rézai-Aria, Effect of aluminizing and oxidation on the thermal fatigue damage of hot work tool steels for high pressure die casting applications, *International Journal of Fatigue* 119 (2019) 126–138.
- [49] A. Persson, S. Hogmark, J. Bergström, Thermal fatigue cracking of surface engineered hot work tool steels, *Surface and Coatings Technology* 191 (2005) 216–227.
- [50] F. Holler, F. Üstel, C. Mitterer, D. Heim, Thermal cycling and oxidation behaviour of hard coatings in aluminium die casting, in: F. Jeglitsch (Ed.), *Tool steels in the next century: Proceedings of the 5th International Conference on Tooling*, September 29th - October 1st, 1999, University of Leoben, Leoben, Austria, Inst. für Metallkunde und Werkstoffprüfung Montanuniversität Leoben, Leoben, 1999.

-
- [51] M. Azadi, G.H. Farrahi, G. Winter, W. Eichlseder, Experimental fatigue lifetime of coated and uncoated aluminum alloy under isothermal and thermo-mechanical loadings, *Ceramics International* 39 (2013) 9099–9107.
- [52] D. Kundalkar, M. Mavalankar, A. Tewari, Effect of gas nitriding on the thermal fatigue behavior of martensitic chromium hot-work tool steel, *Materials Science and Engineering: A* 651 (2016) 391–398.
- [53] N. Mebarki, P. Lamesle, D. Delagnes, C. Levaillant, Relationship between Microstructure and Mechanical Properties of a 5% Cr Hot Work Tool Steel, in: J. Bergström (Ed.), 6. International Tooling Conference: Proceedings of the 6th International Tooling Conference the use of tool steels: experience and research ; Karlstad, Sweden, 10 - 13 September 2002, Karlstad, 2002, pp. 617–632.
- [54] N. Mebarki, D. Delagnes, P. Lamesle, F. Delmas, C. Levaillant, Relationship between microstructure and mechanical properties of a 5% Cr tempered martensitic tool steel, *Materials Science and Engineering: A* 387-389 (2004) 171–175.
- [55] B. Miquel, S. Jean, S. Le Roux, P. Lamesle, F. Rézaï-Aria, Heat-checking of hot work tool steels, *European Structural Integrity Society* 29 (2002) 185–193.
- [56] F. Rézaï-Aria, A. Oudin, S. Jean, B. Miquel, P. Lamesle, An investigation on thermal and thermo-mechanical fatigue of X38CrMoV5 (AISI H11) tool steel, in: NADCA (Ed.), Proceedings of 21th international die casting congress and exposition, North American Die Casting Association, Illinois, 2001.
- [57] S. Jean, B. Miquel, S. Le Roux, F. Rézaï-Aria, An investigation on heat checking of hot work tool steels, in: F. Jeglitsch (Ed.), Tool steels in the next century: Proceedings of the 5th International Conference on Tooling, September 29th - October 1st, 1999, University of Leoben, Leoben, Austria, Inst. für Metallkunde und Werkstoffprüfung Montanuniversität Leoben, Leoben, 1999.
- [58] A. Chauhan, J. Hoffmann, D. Litvinov, J. Aktaa, High-temperature low-cycle fatigue behavior of a 9Cr-ODS steel: Part 1 - pure fatigue, microstructure evolution and damage characteristics, *Materials Science and Engineering: A* 707 (2017) 207–220.
- [59] A. Chauhan, J. Hoffmann, D. Litvinov, J. Aktaa, High-temperature low-cycle fatigue behavior of a 9Cr-ODS steel: Part 2 - hold time influence, microstructural evolution and damage characteristics, *Materials Science and Engineering: A* 730 (2018) 197–206.
- [60] J.W. Martin, *Precipitation Hardening: Theory and Applications*, secondnd ed., Elsevier Science, Burlington, 2012.
- [61] G. Gottstein, *Physikalische Grundlagen der Materialkunde*, third. Auflage, Springer-Verlag Berlin Heidelberg, Berlin, Heidelberg, 2007.
- [62] J.W. Martin, R.D. Doherty, B. Cantor, *Stability of Microstructure in Metallic Systems*, secondnd ed., Cambridge University Press, Cambridge, 2009.
- [63] C. Wagner, Theorie der Alterung von Niederschlägen durch Umlösen (Ostwald-Reifung), *Zeitschrift für Elektrochemie* (1961) 581–591.

- [64] I.M. Lifshitz, V.V. Slyozov, The kinetics of precipitation from supersaturated solid solutions, *Journal of Physics and Chemistry of Solids* 19 (1961) 35–50.
- [65] Z.D. Caliskanoglu, Einfluss der Legierungslage auf das Anwendungspotential temperaturwechselbeanspruchter Warmarbeitsstähle. Dissertation, Leoben, 2002.
- [66] J.C. Ion, K.E. Easterling, M.F. Ashby, A second report on diagrams of microstructure and hardness for heat-affected zones in welds, *Acta Metallurgica* 32 (1984) 1949–1962.
- [67] Ø. Grong, Metallurgical modelling of welding, second. ed., The Institute of Materials, London, 1997.
- [68] O.R. Myhr, Ø. Grong, Process modelling applied to 6082-T6 aluminium weldments—I. Reaction kinetics, *Acta Metallurgica et Materialia* 39 (1991) 2693–2702.
- [69] O.R. Myhr, Ø. Grong, Process modelling applied to 6082-T6 aluminium weldments—II. Applications of model, *Acta Metallurgica et Materialia* 39 (1991) 2703–2708.
- [70] H.J. Chang, C.H. Tsai, J.J. Kai, Effects of temperature on the cyclic deformation behaviour and microstructural changes of 12Cr-1MoVW martensitic stainless steel, *International Journal of Pressure Vessels and Piping* 59 (1994) 31–40.
- [71] W. Zhong-Guang, K. Rahka, P. Nenonen, C. Laird, Changes in morphology and composition of carbides during cyclic deformation at room and elevated temperature and their effect on mechanical properties of Cr-Mo-V steel, *Acta Metallurgica* 33 (1985) 2129–2141.
- [72] H. Wurmbauer, H. Leitner, M. Panzenböck, C. Scheu, H. Clemens, Short-term creep behavior of a Cr Mo V hot-work tool steel, *International Journal of Materials Research* 100 (2009) 1066–1073.
- [73] A. Abel, R.K. Ham, The cyclic strain behaviour of crystals of aluminum-4 wt.% copper—ii. low cycle fatigue, *Acta Metallurgica* 14 (1966) 1495–1503.
- [74] G. Kralik, H. Schneiderhan, Fatigue hardening of Al-4at% Zn single crystals, *Scripta Metallurgica* 6 (1972) 843–849.
- [75] J.B. Clark, A.J. McEvily, Interaction of dislocations and structures in cyclically strained aluminum alloys, *Acta Metallurgica* 12 (1964) 1359–1372.
- [76] Tsuyoshi-Takahashi, K. Sasaki, Low cycle thermal fatigue of aluminum alloy cylinder head in consideration of changing metrology microstructure, *Procedia Engineering* 2 (2010) 767–776.
- [77] M. Mokhtarishirazabad, M. Azadi, G. Hossein Farrahi, G. Winter, W. Eichlseder, Improvement of high temperature fatigue lifetime in AZ91 magnesium alloy by heat treatment, *Materials Science and Engineering: A* 588 (2013) 357–365.
- [78] M. Azadi, M.M. Shirazabad, Heat treatment effect on thermo-mechanical fatigue and low cycle fatigue behaviors of A356.0 aluminum alloy, *Materials & Design* 45 (2013) 279–285.
- [79] R.A. Fournelle, E.A. Grey, M.E. Fine, Fatigue behavior of a precipitation hardening Ni–Al–Cu medium carbon steel, *Metallurgical Transactions A* 7 (1976) 669–682.

References

- [80] M.C. Mataya, R.A. Fournelle, Fatigue behavior of a nial precipitation hardening medium carbon steel, *Metallurgical Transactions A* 9 (1978) 917–925.
- [81] R. Hamano, The effect of the precipitation of coherent and incoherent precipitates on the ductility and toughness of high-strength steel, *Metallurgical Transactions A* 24 (1993) 127–139.
- [82] W.M. Garrison, M.A. Rhoads, An evaluation of an ultra-high strength steel strengthened by alloy carbide and intermetallic precipitation, *Transactions of the Indian Institute of Metals* (1996) 151–162.
- [83] S.D. Erlach, H. Leitner, M. Bischof, H. Clemens, F. Danoix, D. Lemarchand, I. Siller, Comparison of NiAl precipitation in a medium carbon secondary hardening steel and C-free PH13-8 maraging steel, *Materials Science and Engineering: A* 429 (2006) 96–106.
- [84] S.D. Erlach, Precipitation behaviour of Ni and Al alloyed hot-work tool steels and its effects on material properties. Dissertation, Leoben, 2006.
- [85] S. Maim, L.-Å. Norström, Material-related model for thermal fatigue applied to tool steels in hot-work applications, *Metal Science* 13 (1979) 544–550.
- [86] B. Sonderegger, E. Kozeschnik, H. Leitner, H. Clemens, J. Svoboda, F.D. Fischer, P. Staron, Kinetics of Precipitation in a Complex Hot-work Tool Steel, *steel research international* 81 (2010) 64–73.
- [87] D.H. Ping, M. Ohnuma, Y. Hirakawa, Y. Kadoya, K. Hono, Microstructural evolution in 13Cr–8Ni–2.5Mo–2Al martensitic precipitation-hardened stainless steel, *Materials Science and Engineering: A* 394 (2005) 285–295.
- [88] W. Xu, P.E.J. Rivera-Díaz-del-Castillo, W. Wang, K. Yang, V. Bliznuk, L.A.I. Kestens, S. van der Zwaag, Genetic design and characterization of novel ultra-high-strength stainless steels strengthened by Ni₃Ti intermetallic nanoprecipitates, *Acta Materialia* 58 (2010) 3582–3593.
- [89] W. Xu, P.E.J. Rivera-Díaz-del-Castillo, W. Yan, K. Yang, D. San Martín, L.A.I. Kestens, S. van der Zwaag, A new ultrahigh-strength stainless steel strengthened by various coexisting nanoprecipitates, *Acta Materialia* 58 (2010) 4067–4075.
- [90] B.L. Tiemens, Performance optimization and computational design of ultra-high strength gear steels. Dissertation, Illinois, 2006.
- [91] B.L. Tiemens, A.K. Sachdev, R.K. Mishra, G.B. Olson, Three-Dimensional (3-D) Atom Probe Tomography of a Cu-Precipitation-Strengthened, Ultrahigh-Strength Carburized Steel, *Metallurgical and Materials Transactions A* 43 (2012) 3626–3635.
- [92] B.L. Tiemens, A.K. Sachdev, G.B. Olson, Cu-Precipitation Strengthening in Ultrahigh-Strength Carburizing Steels, *Metallurgical and Materials Transactions A* 43 (2012) 3615–3625.

- [93] H. Leitner, M. Bischof, H. Clemens, S. Erlach, B. Sonderegger, E. Kozeschnik, J. Svoboda, F.D. Fischer, Precipitation Behaviour of a Complex Steel, *Advanced Engineering Materials* 8 (2006) 1066–1077.
- [94] F. Pettinari-Sturmel, B. Kedjar, J. Douin, C. Gatel, D. Delagnes, A. Coujou, TEM study of structural hardening in a new martensitic steel for aeronautic application, *Materials Science and Engineering: A* 576 (2013) 290–297.
- [95] V. Seetharaman, M. Sundararaman, R. Krishnan, Precipitation hardening in a PH 13-8 Mo stainless steel, *Materials Science and Engineering* 47 (1981) 1–11.
- [96] S.D. Erlach, F. Danoix, H. Leitner, P. Auger, I. Siller, H. Clemens, Precipitation reactions during the early stages of aging in a Ni and Al alloyed martensitic medium carbon steel, *Surface and Interface Analysis* 39 (2007) 213–220.
- [97] P. Villars, K. Cenzual, NiAl Crystal Structure: Datasheet from "PAULING FILE Multinaries Edition – 2012" in SpringerMaterials (http://materials.springer.com/isp/crystallographic/docs/sd_1250058), Springer-Verlag Berlin Heidelberg & Material Phases Data System (MPDS), Switzerland & National Institute for Materials Science (NIMS), Japan.
- [98] M. Schober, R. Schnitzer, H. Leitner, Precipitation evolution in a Ti-free and Ti-containing stainless maraging steel, *Ultramicroscopy* 109 (2009) 553–562.
- [99] R.P. Kolli, Z. Mao, D.N. Seidman, D.T. Keane, Identification of a Ni_{0.5}(Al_{0.5}–xMn_x) B₂ phase at the heterophase interfaces of Cu-rich precipitates in an α -Fe matrix, *Applied Physics Letters* 91 (2007) 241903.
- [100] E. Kozeschnik, Thermodynamic prediction of the equilibrium chemical composition of critical nuclei, *Scripta Materialia* 59 (2008) 1018–1021.
- [101] I. Holzer, E. Kozeschnik, Computer simulation of the yield strength evolution in Cu-precipitation strengthened ferritic steel, *Materials Science and Engineering: A* 527 (2010) 3546–3551.
- [102] R. Monzen, M. Iguchi, M.L. Jenkins, Structural changes of 9R copper precipitates in an aged Fe-Cu alloy, *Philosophical Magazine Letters* 80 (2000) 137–148.
- [103] P. Warczok, D. Reith, M. Schober, H. Leitner, R. Podlucky, E. Kozeschnik, Investigation of Cu precipitation in bcc-Fe – Comparison of numerical analysis with experiment, *International Journal of Materials Research* 102 (2011) 709–716.
- [104] P.J. Othen, M.L. Jenkins, G.D.W. Smith, W.J. Phythian, Transmission electron microscope investigations of the structure of copper precipitates in thermally-aged Fe—Cu and Fe—Cu—Ni, *Philosophical Magazine Letters* 64 (1991) 383–391.
- [105] P.J. Othen, M.L. Jenkins, G.D.W. Smith, High-resolution electron microscopy studies of the structure of Cu precipitates in α -Fe, *Philosophical Magazine A* 70 (1994) 1–24.
- [106] G. Stechauner, S. Primig, E. Kozeschnik, Early Stages of Cu Precipitation in 15-5 PH Maraging Steel Revisited - Part II: Thermokinetic Simulation, *steel research international* 88 (2017) 1600085.

- [107] S. Primig, G. Stechauner, E. Kozeschnik, Early Stages of Cu Precipitation in 15-5 PH Maraging Steel Revisited – Part I: Experimental Analysis, *steel research international* 88 (2017) 1600084.
- [108] Z.B. Jiao, J.H. Luan, M.K. Miller, C.Y. Yu, C.T. Liu, Group precipitation and age hardening of nanostructured Fe-based alloys with ultra-high strengths, *Scientific reports* 6 (2016).
- [109] S. Vaynman, D. Isheim, R. Prakash Kolli, S.P. Bhat, D.N. Seidman, M.E. Fine, High-Strength Low-Carbon Ferritic Steel Containing Cu-Fe-Ni-Al-Mn Precipitates, *Metallurgical and Materials Transactions A* 39 (2008) 363–373.
- [110] Z.B. Jiao, J.H. Luan, Z.W. Zhang, M.K. Miller, W.B. Ma, C.T. Liu, Synergistic effects of Cu and Ni on nanoscale precipitation and mechanical properties of high-strength steels, *Acta Materialia* 61 (2013) 5996–6005.
- [111] D. Isheim, M.S. Gagliano, M.E. Fine, D.N. Seidman, Interfacial segregation at Cu-rich precipitates in a high-strength low-carbon steel studied on a sub-nanometer scale, *Acta Materialia* 54 (2006) 841–849.
- [112] D. Isheim, R.P. Kolli, M.E. Fine, D.N. Seidman, An atom-probe tomographic study of the temporal evolution of the nanostructure of Fe–Cu based high-strength low-carbon steels, *Scripta Materialia* 55 (2006) 35–40.
- [113] K. Osamura, H. Okuda, K. Asano, M. Furusaka, K. Kishida, F. Kurosawa, R. Uemori, SANS Study of Phase Decomposition in Fe-Cu Alloy with Ni and Mn Addition, *ISIJ International* 34 (1994) 346–354.
- [114] R.P. Kolli, D.N. Seidman, The temporal evolution of the decomposition of a concentrated multicomponent Fe–Cu-based steel, *Acta Materialia* 56 (2008) 2073–2088.
- [115] M. Kapoor, D. Isheim, G. Ghosh, S. Vaynman, M.E. Fine, Y.-W. Chung, Aging characteristics and mechanical properties of 1600MPa body-centered cubic Cu and B2-NiAl precipitation-strengthened ferritic steel, *Acta Materialia* 73 (2014) 56–74.
- [116] Z.B. Jiao, J.H. Luan, M.K. Miller, C.T. Liu, Precipitation mechanism and mechanical properties of an ultra-high strength steel hardened by nanoscale NiAl and Cu particles, *Acta Materialia* 97 (2015) 58–67.
- [117] H. Leitner, R. Schnitzer, M. Schober, S. Zinner, Precipitate modification in PH13-8 Mo type maraging steel, *Acta Materialia* 59 (2011) 5012–5022.
- [118] R. Schnitzer, M. Schober, S. Zinner, H. Leitner, Effect of Cu on the evolution of precipitation in an Fe–Cr–Ni–Al–Ti maraging steel, *Acta Materialia* 58 (2010) 3733–3741.
- [119] S. Höring, N. Wanderka, J. Banhart, The influence of Cu addition on precipitation in Fe-Cr-Ni-Al-(Cu) model alloys, *Ultramicroscopy* 109 (2009) 574–579.
- [120] M. Kapoor, D. Isheim, S. Vaynman, M.E. Fine, Y.-W. Chung, Effects of increased alloying element content on NiAl-type precipitate formation, loading rate sensitivity,

- and ductility of Cu- and NiAl-precipitation-strengthened ferritic steels, *Acta Materialia* 104 (2016) 166–171.
- [121] F. Danoix, R. Danoix, J. Akre, A. Grellier, D. Delagnes, Atom probe tomography investigation of assisted precipitation of secondary hardening carbides in a medium carbon martensitic steels, *Journal of microscopy* 244 (2011) 305–310.
- [122] M. Perrut, M.-H. Mathon, D. Delagnes, Small-angle neutron scattering of multiphase secondary hardening steels, *Journal of Materials Science* 47 (2012) 1920–1929.
- [123] M.D. Mulholland, D.N. Seidman, Nanoscale co-precipitation and mechanical properties of a high-strength low-carbon steel, *Acta Materialia* 59 (2011) 1881–1897.
- [124] C. Bellot, P. Lamesle, D. Delagnes, XRD synchrotron study of carbide precipitation in martensitic steels during tempering, *Acta Metallurgica Sinica (English Letters)* 26 (2013) 553–557.
- [125] J.-G. Jung, M. Jung, S.-M. Lee, E. Shin, H.-C. Shin, Y.-K. Lee, Cu precipitation kinetics during martensite tempering in a medium C steel, *Journal of Alloys and Compounds* 553 (2013) 299–307.
- [126] J. Akre, F. Danoix, H. Leitner, P. Auger, The morphology of secondary-hardening carbides in a martensitic steel at the peak hardness by 3DFIM, *Ultramicroscopy* 109 (2009) 518–523.
- [127] D.T. Peters, A study of austenite refersion during aging of maraging steels, *Transactions of the ASM* (1968) 62–74.
- [128] M. Bischof, S. Erlach, P. Staron, H. Leitner, C. Scheu, H. Clemens, Combining complementary techniques to study precipitates in steels, *Zeitschrift für Metallkunde* 96 (2005) 1074–1080.
- [129] W. Lefebvre-Ulrikson, F. Vurpillot, X. Sauvage (Eds.), *Atom probe tomography: Atom probe tomography: Put theory into practice*, Academic Press, London, 2016.
- [130] F. Vurpillot, A. Bostel, D. Blavette, Trajectory overlaps and local magnification in three-dimensional atom probe, *Applied Physics Letters* 76 (2000) 3127–3129.
- [131] A.R. Waugh, E.D. Boyes, M.J. Southon, Investigations of field evaporation with a field-desorption microscope, *Surface Science* 61 (1976) 109–142.
- [132] M. Thuvander, J. Weidow, J. Angseryd, L.K.L. Falk, F. Liu, M. Sonestedt, K. Stiller, H.-O. Andrén, Quantitative atom probe analysis of carbides, *Ultramicroscopy* 111 (2011) 604–608.
- [133] Y. Dong, A. Etienne, A. Frolov, S. Fedotova, K. Fujii, K. Fukuya, C. Hatzoglou, E. Kuleshova, K. Lindgren, A. London, A. Lopez, S. Lozano-Perez, Y. Miyahara, Y. Nagai, K. Nishida, B. Radiguet, D.K. Schreiber, N. Soneda, M. Thuvander, T. Toyama, J. Wang, F. Sefta, P. Chou, E.A. Marquis, Atom Probe Tomography Interlaboratory Study on Clustering Analysis in Experimental Data Using the Maximum Separation Distance Approach, *Microscopy and Microanalysis* (2019) 1–11.

- [134] R.P. Kolli, D.N. Seidman, Comparison of compositional and morphological atom-probe tomography analyses for a multicomponent Fe-Cu steel, *Microscopy and Microanalysis* 13 (2007) 272–284.
- [135] A. Heinrich, T.a. Al-Kassab, R. Kirchheim, Investigation of the early stages of decomposition of Cu–0.7at.% Fe with the tomographic atom probe, *Materials Science and Engineering: A* 353 (2003) 92–98.
- [136] M.K. Miller, E.A. Kenik, Atom probe tomography: a technique for nanoscale characterization, *Microscopy and Microanalysis* 10 (2004) 336–341.
- [137] L.T. Stephenson, M.P. Moody, P.V. Liddicoat, S.P. Ringer, New techniques for the analysis of fine-scaled clustering phenomena within atom probe tomography (APT) data, *Microscopy and Microanalysis* 13 (2007) 448–463.
- [138] D. Vaumousse, A. Cerezo, P.J. Warren, A procedure for quantification of precipitate microstructures from three-dimensional atom probe data, *Ultramicroscopy* 95 (2003) 215–221.
- [139] M.P. Moody, L.T. Stephenson, A.V. Ceguerra, S.P. Ringer, Quantitative binomial distribution analyses of nanoscale like-solute atom clustering and segregation in atom probe tomography data, *Microscopy research and technique* 71 (2008) 542–550.
- [140] C.K. Sudbrack, K. YOON, R. NOEBE, D.N. Seidman, Temporal evolution of the nanostructure and phase compositions in a model Ni–Al–Cr alloy, *Acta Materialia* 54 (2006) 3199–3210.
- [141] F. de Geuser, W. Lefebvre, D. Blavette, 3D atom probe study of solute atoms clustering during natural ageing and pre-ageing of an Al-Mg-Si alloy, *Philosophical Magazine Letters* 86 (2006) 227–234.
- [142] C.K. Sudbrack, R. d. Noebe, D.N. Seidman, Direct observations of nucleation in a nondilute multicomponent alloy, *Microscopy and Microanalysis* 73 (2006) 437.
- [143] P. Huter, S. Oberfrank, F. Grün, B. Stauder, Thermo-mechanical fatigue influence of copper and silicon on hypo-eutectic Al–Si–Cu and Al–Si–Mg cast alloys used in cylinder heads, *International Journal of Fatigue* 88 (2016) 142–155.
- [144] R. Schnitzer, R. Radis, M. Nöhler, M. Schober, R. Hochfellner, S. Zinner, E. Povoden-Karadeniz, E. Kozeschnik, H. Leitner, Reverted austenite in PH 13-8 Mo maraging steels, *Materials Chemistry and Physics* 122 (2010) 138–145.
- [145] P. Hähner, E. Affeldt, T. Beck, H. Klingelhöffer, M. Loveday, C. Rinaldi, Thermo-mechanical fatigue - the route to standardisation, Office for Official Publications of the European Communities, Luxembourg, 2006, Information on https://netzwerke.bam.de/Netzwerke/Content/EN/Downloads/jrc-tmf-validated-code-of-practice.pdf?__blob=publicationFile (accessed 26 November 2018).

Part B

Paper I

M. Hofinger, M. Staudacher, M. Ognianov, C. Turk, H. Leitner, R. Schnitzer

Microstructural evolution of a dual hardening steel during heat treatment

Micron 120 (2019) 48-56

DOI: [10.1016/j.micron.2019.02.004](https://doi.org/10.1016/j.micron.2019.02.004)

Microstructural evolution of a dual hardening steel during heat treatment

Matthias Hofinger ¹, Maximilian Staudacher ¹, Miloslav Ognianov ², Christoph Turk ²,
Harald Leitner ², Ronald Schnitzer ¹

1 Montanuniversität Leoben, Department of Physical Metallurgy and Materials Testing,
Franz-Josef-Straße 18, 8700 Leoben, Austria

2 voestalpine Böhler Edelstahl GmbH & Co KG, Mariazellerstraße 25, 8605 Kapfenberg,
Austria

Abstract

Dual hardening steels combine precipitation of both secondary hardening carbides and intermetallic phases in a martensitic matrix. Due to this combination, the carbon content necessary to achieve high hardness levels can be reduced, resulting in a decreased amount of large and embrittling carbides.

In this study, the influence of different heat treatments on microstructure evolution and secondary hardness is investigated. Different metallographic preparation methods were tested in order to visualize the microstructure. Carbides were characterized using spot-pattern electron backscatter diffraction.

For light optical investigations, preparation with V2A-pickle lead to the best results. Preparation with colloidal silica suspension achieved the best results for investigations by scanning electron microscopy and for carbide characterization using electron backscatter diffraction. It was found that a homogenization treatment prior to austenitization was unable to increase the amount of dissolved carbides, and thus had no effect on secondary hardness. By increasing the austenitization temperature, the amount of carbides and secondary hardness could be increased significantly.



Tutorial

Microstructural evolution of a dual hardening steel during heat treatment

Matthias Hofinger^{a,*}, Maximilian Staudacher^a, Miloslav Ognianov^b, Christoph Turk^b, Harald Leitner^b, Ronald Schnitzer^a

^a Montanuniversität Leoben, Department of Physical Metallurgy and Materials Testing, Franz-Josef-Straße 18, 8700, Leoben, Austria

^b voestalpine Böhler Edelstahl GmbH & Co KG, Mariazellerstraße 25, 8605 Kapfenberg, Austria



ARTICLE INFO

Keywords:

Dual hardening steel
Heat treatment
Electron backscatter diffraction
Primary carbides

ABSTRACT

Dual hardening steels combine precipitation of both secondary hardening carbides and intermetallic phases in a martensitic matrix. Due to this combination, the carbon content necessary to achieve high hardness levels can be reduced, resulting in a decreased amount of large and embrittling carbides.

In this study, the influence of different heat treatments on microstructure evolution and secondary hardness is investigated. Different metallographic preparation methods were tested in order to visualize the microstructure. Carbides were characterized using spot-pattern electron backscatter diffraction.

For light optical investigations, preparation with V2A-pickle lead to the best results. Preparation with colloidal silica suspension achieved the best results for investigations by scanning electron microscopy and for carbide characterization using electron backscatter diffraction. It was found that a homogenization treatment prior to austenitization was unable to increase the amount of dissolved carbides, and thus had no effect on secondary hardness. By increasing the austenitization temperature, the amount of carbides and secondary hardness could be increased significantly.

1. Introduction

The first investigations on dual hardening steels were conducted by Garrison et al. (Garrison and Bhat, 1988) in order to develop high strength secondary hardening steels with improved fracture toughness. The attempt was to reduce the alloying content of carbon in order to lower the amount of embrittling primary carbides. The loss in strength was compensated for by the addition of Al and Ni which are known to form intermetallic precipitates in ferritic and martensitic steels (Erlach et al., 2007; Leitner et al., 2006, 2010; Schober et al., 2009, 2010; Seetharaman et al., 1981). Although developed for the aeronautic industry, efforts were made to adopt these steels for hotwork applications (Delagnes et al., 2012; Erlach et al., 2006). For hot-work tool steels, high hardness especially at elevated temperatures is paramount. Their microstructure consists of μm -sized primary MC and M_6C carbides embedded in a martensitic matrix, which is further strengthened by nm-sized secondary hardening precipitates, usually MC and M_2C carbides. Primary MC carbides are formed by alloying with V, whereas M_2C is favored by the addition of Mo but metastable with respect to M_6C . The precipitation of M_6C is preferred in steels containing W and Si. Due to their complicated crystal structure, the thermodynamic stable M_6C only form when annealed at high temperatures for several hours or during

slow cooling steps. The metastable M_2C then decompose to MC and M_6C . (Brandis et al., 1977; Pippel et al., 1999; Roberts et al., 2010). Kim et al. (2015) observed primary M_2C carbides in a cold-work tool steel in the as-cast state as well as after reheating to hot deformation temperature and subsequent quenching. After hot deformation, the M_2C carbides were dissolved. For primary carbide identification and characterization, measurement of electron backscatter diffraction (EBSD) spotpattern has successfully been used (Kim et al., 2015; Laigo et al., 2006, 2008; Peruš et al., 2017).

The amount of nm-sized strengthening precipitates is adjusted by alloy composition as well as heat treatment parameters (Bellot et al., 2013; Danoix et al., 2011; Delagnes et al., 2012; Erlach et al., 2006; Garrison and Bhat, 1988; Perrut et al., 2012). To obtain the desired mechanical properties, austenitization has to meet several requirements. These include a defined volume fraction of undissolved primary carbides which inhibit grain growth throughout austenitization and reduce abrasive wear during application. Furthermore, the amount of alloying elements dissolved in the austenite controls hardenability at tempering (Roberts et al., 2010). To meet these requirements, both austenitization temperature and time have to be optimized. Dual hardening steels are usually austenitized at temperatures ranging from 950 °C to 1100 °C and subsequently quenched in oil or air cooled. The

* Corresponding author.

E-mail address: Matthias.hofinger@unileoben.ac.at (M. Hofinger).

<https://doi.org/10.1016/j.micron.2019.02.004>

Received 10 October 2018; Received in revised form 8 February 2019; Accepted 8 February 2019

Available online 10 February 2019

0968-4328/ © 2019 Elsevier Ltd. All rights reserved.

quenching is followed by a single or multiple annealing step at temperatures up to 610 °C in order to achieve age hardening (Bischof et al., 2005; Erlach et al., 2006, 2007; Garrison and Bhat, 1988; Leitner et al., 2006).

Erlach et al. (2006) were able to show that dual hardening steels containing NiAl and secondary hardening M₂C carbides experience a rapid age hardening response upon ageing. Phase separation starts at ageing for less than one minute at 610 °C. Whereas in Ni and Al free steels secondary hardening M₂C carbide precipitation is limited to lattice defects such as martensite lath boundaries and dislocations, intermetallic βNiAl particles form spherical precipitates which are homogeneously distributed within the martensitic matrix (Danoix et al., 2011). In dual hardening steels combining M₂C and β-NiAl precipitation, preferential nucleation sites for M₂C carbides shift from lattice defects to βNiAl particles. Because of the more homogenous distribution and higher number density of intermetallic precipitates compared to lattice defects, additional alloying with Ni and Al leads to a refined and more homogenous distribution of secondary hardening carbides (Danoix et al., 2011).

Although the precipitation reactions during ageing have already been studied in detail (Danoix et al., 2011; Delagnes et al., 2012; Erlach et al., 2006, 2007; Leitner et al., 2006; Perrut et al., 2012), to the authors best knowledge, no investigations on primary carbide morphology, distribution and type in dual hardening steels have been published. This study aims to improve the understanding of the carbide evolution during heat treatment in dual hardening steels, thus enabling their utilization for hot work applications.

In order to understand the phase transformations during each heat treatment step, a complete characterization of the microstructure is necessary. In this study, different heat treatments were conducted to measure the secondary hardening response and study the microstructural evolution of the investigated dual hardening alloy. Several different preparation methods were tested to achieve the best results for microstructural investigations utilizing light optical microscopy (LOM) and scanning electron microscopy (SEM). EBSD spot-patterns were recorded to characterize carbides present in different heat treatment conditions. With the knowledge of microstructure constituents such as carbide type, distribution and morphology, optimized heat treatment parameters regarding austenitization for the best combination of mechanical properties can be determined.

2. Experimental

The chemical composition of the investigated dual hardening steel is given in Table 1. The material was produced by an electric arc furnace, electro slag remelted and subsequently forged to a diameter of 160 mm, followed by a stress relief heat treatment. This state will further be referred to as the received condition. To understand the phase transformations during each heat treatment step, microstructural investigations were conducted on specimens in different heat treatment conditions. 20 × 20 × 10 mm³ cuboid samples were cut from the center of the bulk to avoid any elemental segregations in the investigated material. Before heat treatment, the samples were packed in austenitic foil to reduce oxidation and decarburization as the heat treatments were done in a laboratory chamber furnace with air atmosphere. The schematics of the different heat treatments conducted in this study are shown in Fig. 1. These included a homogenization heat treatment for carbide dissolution (Lichtenegger, 1995). These heat treatments are

Table 1
Chemical composition in mass-% (m %) of the investigated dual hardening steel.

	C	Ni	Al	Cr	Mo	V	Si	Mn	Fe
(m%)	0.35	4.80	1.50	3.00	2.50	0.85	0.20	0.25	bal.

usually conducted on tool steels containing metastable M₂C carbides. During annealing, the M₂C carbides dissolve into the thermodynamic stable M₆C and MC carbides. Because of a higher ratio of Fe incorporated into M₆C compared to M₂C, the amount of carbides increases. The MC carbides produced by the dissolution of the M₂C are rich in V and have a small particle size, which increases the amount of dissolved V during the austenitization and hence increases the achievable secondary hardness (Lichtenegger, 1995). The Ac3-temperature of the investigated dual hardening alloy was determined in the range of 1100 °C via thermodynamic calculations with MatCalc.

For the M₂C carbide dissolution, samples were heated to 1100 °C, held for 5 h and cooled with 50 °C/h to 900 °C. After 4 h at 900 °C, the specimens were cooled with 10 °C/h to 750 °C, held for another 2 h and furnace cooled to room temperature. The holding steps were introduced to apply a comparable heat treatment as conducted in industrial applications. Two different sets of austenitization parameters were tested. For austenitization at the lower temperature, specimens were heated to 990 °C within 10 min and held for another 30 min.

The austenitization treatment at the higher temperature consisted of heating the specimens to 1200 °C within 10 min and holding for another 5 min at the given temperature. Subsequently, all samples were quenched in oil to room temperature. The ageing was done isothermally at temperatures from 200 °C to 700 °C. Each sample was aged 3 times for 3 h. For ageing temperatures exceeding 585 °C, the temperature for the last annealing step was reduced to 585 °C. To investigate the influence of the carbide dissolution heat treatment, different combinations of these heat treatments were investigated, which are summarized in Table 2. One set of samples was subjected to a carbide dissolution heat treatment prior to austenitization, whereas others were austenitized from the as received condition without previous annealing.

Hardness was measured in HV10 with an EMCO-Test M4C G3 and the given values for mean hardness and standard deviation were calculated from 3 valid hardness indents. The hardness values given in HRC were calculated using Eq. (1) (Blumenauer, 2001).

$$HRC \approx 116 - 1500/\sqrt{HV} \quad (1)$$

For microstructural investigations, specimens were prepared by standard grinding and polishing techniques (Petzow, 1977). As the investigated alloys composition is quite complex, four different preparation methods were tested in order to obtain the best results for visualization of both the martensitic microstructure as well as carbide morphology and distribution. These etchants are summarized in Table 3. Kalling I and Kalling II were chosen because they are known to reveal martensitic structures in highalloy and maraging steels (Bramfitt and Benschoter, 2002; Schnitzer et al., 2009). As a standard etchant for high-alloy steels, V2A-pickle was used (Petzow, 1977). For this preparation method, no carbon containing mounting material can be used, as it is dissolved by the etchant. The V2A-pickel is heated to 100 °C in a water bath and applied by wiping the sample surface with a soaked cotton pad. Finally, preparation with a colloidal silica suspension was used for sample preparation for both microstructural investigations in the SEM and EBSD measurements (Katrakova et al., 1998; Kim et al., 2015). The specimens were examined in a LOM Zeiss Axio Imager and in a SEM Zeiss Evo50. Because of their difference in average atomic mass number compared to the surrounding iron matrix, BSE imaging mode was selected for carbide identification in SEM.

To characterize the carbides present in different heat treatment conditions, EBSD spotpatterns were recorded. For this purpose, the polishing time with colloidal silica suspension was reduced to 30–60 s to minimize height differences on the sample surface but still reveal carbide structures (Katrakova et al., 1998). The EBSD measurements were conducted in a Versa 3D DualBeam™ from FEI equipped with an EBSD Camera Hikari XP EBSD from Edax. The Kikuchi patterns were obtained at an acceleration voltage of 20 kV and a working distance of 15 mm. For data acquisition and processing, the software Team™ V4.3

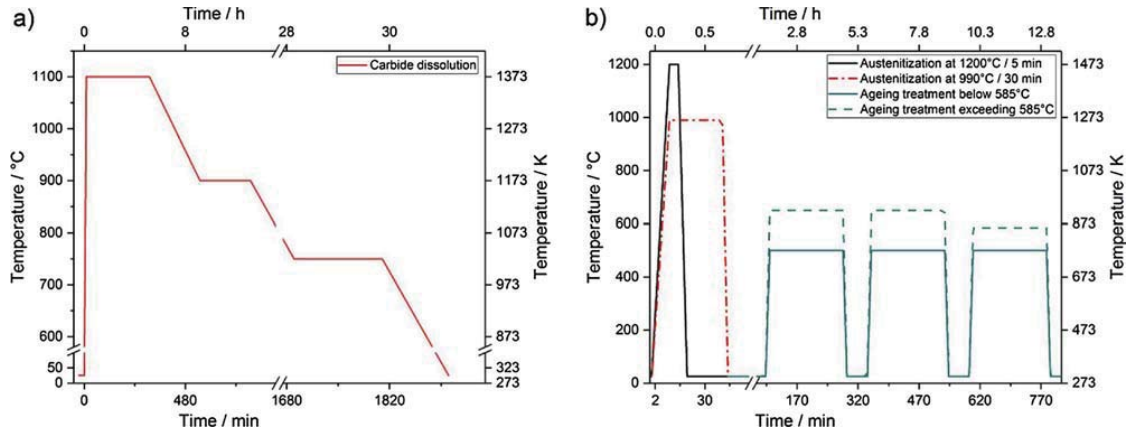


Fig. 1. Schematic of the temperature control of the different heat treatments. a) Temperature control for carbide dissolution heat treatment and b) for different austenitization treatments and subsequent ageing, exemplary shown for 500 °C and 650 °C. Note change in scaling at axis breaks.

Table 2
Overview of investigated heat treatment conditions.

Carbide dissolution	Austenitization / °C	Ageing / °C
Yes	/	/
Yes	990	200-700
Yes	1200	200-700
No	990	200-700
No	1200	200-700

from Edax was used. Phase identification was done with the database built in the Team™ software and for every recorded pattern the best fit with one of the following possible solutions was chosen: Fe-bcc, Fe-fcc, cementite, MC, M₂C, M₆C, M₇C₃. Unfortunately, the intermetallic NiAl precipitates present in the investigated dual hardening steel are in the size range of 5100 nm and thus too small to be characterized by LOM or SEM (Schober et al., 2009). Hence, the current investigation concentrates on the evolution of the carbides present in different heat treatment conditions and the iron matrix.

3. Results

3.1. Hardness depending on heat treatment parameters

The measured hardness values are shown in Fig. 2. The blue and green line represent the hardness of specimens which were subjected to a homogenization heat treatment for carbide dissolution prior to austenitization (Lichtenegger, 1995). Additional, two different austenitization treatments were conducted. The black and green line represent the hardness of specimens which were austenitized for 30 min at 990 °C, the blue and red line for 5 min at 1200 °C. The black line shows the hardness after austenitization at 990 °C for 30 min without carbide dissolution treatment. After quenching in oil, an initial hardness of

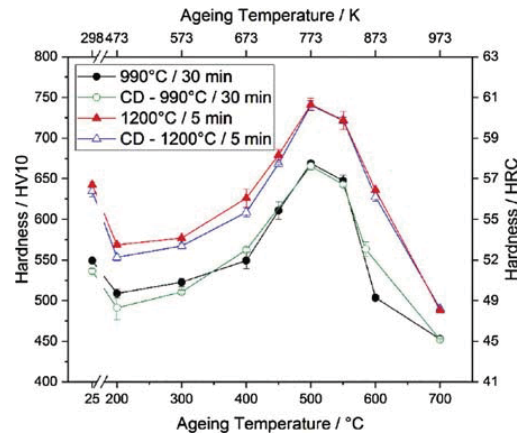


Fig. 2. Hardness depending on different heat treatment parameters. The ageing process consisted of 3 steps each lasting 3 h at the given temperature. The curves vary by the austenitization temperature from 990 °C for 30 min to 1200 °C for 5 min and an additionally carbide dissolution treatment (CD) conducted prior to austenitization.

549 ± 2 HV10 is reached. At lower annealing temperatures, a slight drop to 509 ± 5 HV10 and from 400 °C to 600 °C a secondary hardening peak reaching up to 668 ± 1 HV10 at 500 °C can be observed. An austenitization temperature of 1200 °C results in an increase in the initial hardness to 643 ± 3 HV10, followed by a more pronounced drop at lower annealing temperatures. The maximum secondary hardness of 741 ± 8 HV10 is reached at the same ageing temperature as obtained by the lower austenitization temperature. Above annealing temperatures of 550 °C, a rapid drop of secondary hardness is observed

Table 3
Summary of different etchants used for metallographic preparation.

Etchant	Kalling I	Kalling II	V2A-pickle	Silica suspension
Constituents	33 ml hydrochloric acid 33 ml ethyl alcohol 1.5 g cupric chloride 33 ml water (Bramfitt and Benschoter, 2002)	100 ml hydrochloric acid 5 g cupric chloride 100 ml ethyl alcohol (Bramfitt and Benschoter, 2002)	100 ml distilled water 100 ml hydrochloric acid 10 ml nitric acid 0.3 ml Sparbeize (Petzow, 1977)	silica water < 25% ethanediol
Etching time / s	10	5	30-150	30-60
Etching temperature / °C	25	25	80-100	25

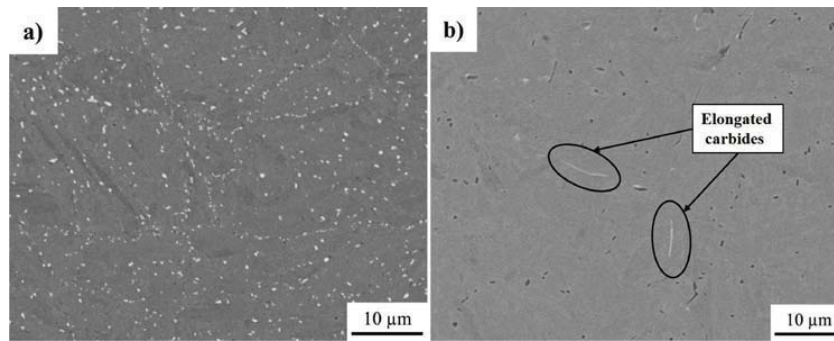


Fig. 3. BSE SEM micrographs a) of the as received condition and b) after carbide dissolution heat treatment, prepared with colloidal silica suspension.

independent of the austenitization temperature. A carbide dissolution treatment applied prior to austenitization, green curve for austenitization at 990 °C and blue curve for austenitization at 1200 °C, does not have any impact on the secondary hardness, independent of the ageing temperature.

3.2. Microstructure characterization with LOM and SEM

A BSE SEM micrograph of the as received condition is shown in Fig. 3 a) and of a specimen subjected to the carbide dissolution heat treatment is shown in Fig. 3 b). It can be seen that in the as received conditions, large amounts of primary carbides are present which form beading-like structures along prior austenite grain boundaries. After the carbide dissolution heat treatment, the amount of primary carbides is reduced, and carbide mass contrast as well as morphology have changed. The contrast of the spherical carbides located within prior austenite grains is darker compared to the surrounding iron matrix, indicating carbides containing a high ratio of carbon to alloying elements such as Cr and Mo. EDX measurements confirmed a decreased amount of Cr and Mo and increased V compared to the carbides in the as received condition, which is typical for MC carbides. Along prior austenite grain boundaries, the beading-like structures have disappeared and elongated, needle-shaped carbides are present. These elongated carbides have similar contrast compared to the spherical particles visible in Fig. 3 a).

Fig. 4 a) shows a light optical micrograph of a specimen subjected to a carbide dissolution heat treatment, etched with Kalling II for 5 s. A martensitic microstructure is visible but carbide structures cannot be determined. Fig. 4 b) shows the same sample etched with V2A-pickle for 30 s. Whilst the martensitic microstructure cannot be easily determined, a high amount of small spherical particles can be seen, which are also visible in Fig. 4 c), along with elongated particles which occupy prior austenite grain boundaries. Fig. 4 d) shows a light optical micrograph of the same specimen prepared with colloidal silica suspension. A micrograph of the same sample is shown in Fig. 3 b), where two different types of carbides can be identified by their difference in mass contrast compared to the iron matrix. From their morphology and distribution, it can be determined that the spherical particles as well as the elongated structures along prior austenite grain boundaries in Fig. 4 also represent carbides. Hence, these structures are made visible by the preparation with V2A-pickle and preparation with colloidal silica suspension.

In Fig. 5, light optical micrographs of different heat treatment conditions prepared with V2A-pickle are shown. Fig. 5 a) and b) both show specimens austenitized at 990 °C. Whilst the microstructure shown in b) was subjected to a carbide dissolution heat treatment prior to austenitization, no such treatment was performed on the specimen shown in a). In both micrographs, needle-shaped martensite laths and spherical carbides within prior austenite grains as well as elongated

carbides along prior austenite grain boundaries are visible. In Fig. 5 c) and d) a martensitic microstructure is visible, as well as prior austenite grain boundaries. Neither spherical carbides within these grains nor elongated carbides along prior austenite grain boundaries can be seen. The prior austenite grains appear enlarged compared to Fig. 5 a) and b). Both specimens were subject to an austenitization temperature of 1200 °C, while on d) also a carbide dissolution heat treatment was performed.

3.3. Carbide characterization with EBSD

Fig. 6 a) shows a SE SEM micrograph of the as received condition, the spots indicate the locations of the measured EBSD spot-patterns. The obtained patterns are depicted in Fig. 6 b) to d), and the best matching solution determined by Edax TEAM™ V4.3 database is shown in Fig. 6 e) to g). The pattern obtained from spot 1 shows the best match with MC-fcc structure whereas at the location of spot 2, a M_2C -hcp carbide was identified. In direct proximity at spot 3, a M_6C -fcc carbide was detected. Most of these larger carbides are located along prior austenite grain boundaries. Within the prior austenite grains, fine distributed spherical carbides could be determined. Unfortunately, these were too small to be measured by EBSD spot-measurements.

After the carbide dissolution heat treatment, the same types of MC, M_2C and M_6C carbides could be identified. Fig. 7 a) to c) shows the locations of the conducted EBSD spot-measurements and the corresponding pattern and indexed solutions for MC, M_2C and M_6C are shown in Fig. 7 d) to i), respectively. The needle shaped carbide structures visible in Fig. 7 c) can be identified as M_6C carbides. It can be concluded that the carbide dissolution heat treatment does not dissolve the metastable M_2C carbides in the investigated alloy.

Fig. 8 shows the patterns and solutions obtained from a specimen austenitized at 990 °C which was aged at 450 °C as well as the positions of the measured spots. Within this sample, only MC and M_6C carbides could be identified. Both types of carbides have spherical to rod-shaped morphologies and tend to form beading-like structures along prior austenite grain boundaries. Hence, after the ageing step no more metastable M_2C carbides are present. A summary of the investigated heat treatment conditions and carbide types present in each condition is given in Table 4.

4. Discussion

The microstructural evolution of a dual hardening steel was investigated using different etching methods as well as EBSD spot-pattern analysis to characterize the different types of carbides. To measure the potential for secondary hardening, different heat treatments were conducted. In Fig. 2, a secondary hardening peak is clearly visible in the temperature range from 400 °C to 600 °C. With increasing austenitization temperature, the amount of carbon and other alloying elements

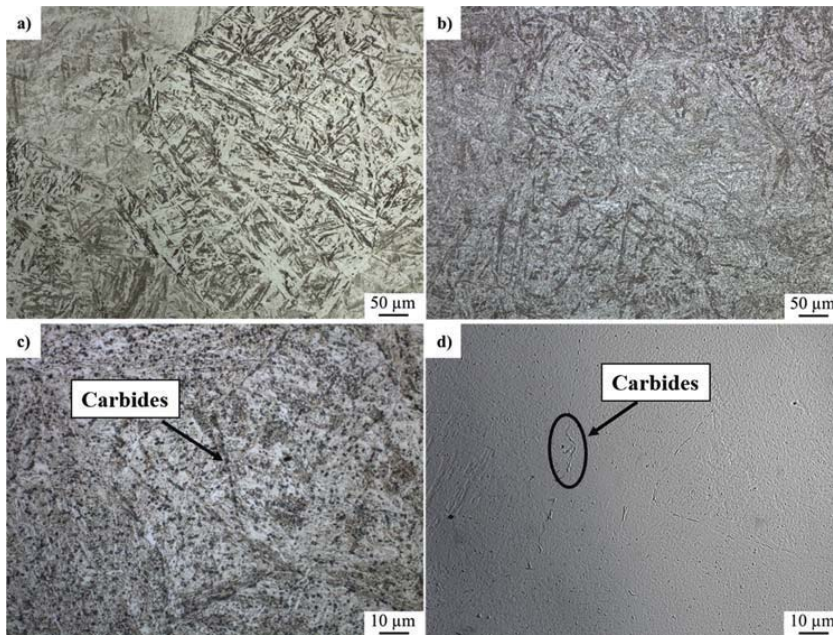


Fig. 4. Light optical micrographs of the investigated steel subjected to a carbide dissolution heat treatment and prepared with different etchants. a) Specimen etched with Kalling II, b) etched using V2A-pickle, c) etched using V2A-pickle and higher magnification. d) Polished with colloidal silica suspension, discolored. Note different scale bars.

dissolved in the austenite is increased. Thus, with increasing carbon content in the austenite, the hardness after quenching increases with rising austenitization temperature. At lower ageing temperatures up to 200 °C, the hardness drop is more pronounced for the higher austenitization temperature as the stress relief in the distorted martensite leads to a softening while the temperature is still too low for precipitation hardening in dual hardening steels (Edmonds and Pereloma, 2012; Fournelle et al., 1976; Garrison and Bhat, 1988).

At ageing temperatures exceeding 200 °C, both intermetallic NiAl and secondary hardening carbides start to precipitate, resulting in an

increase in hardness. The intermetallic NiAl are coherent to the iron matrix (Ping et al., 2005) and thus likely to be precipitated first, acting as heterogeneous precipitation sites for the secondary hardening carbides. These are typically M_2C carbides (Erlach et al., 2006). The higher austenitization temperature leads to an increased amount of V and Mo dissolved in the austenite, thus a higher number density of secondary hardening carbides is precipitated, shifting the hardness curve to higher levels. After ageing for 9 h, the temperature range of the secondary hardening maximum is independent of the austenitization treatment. The maximum hardness of 741 ± 8 HV10 (60.9 ± 0.3 HRC) is

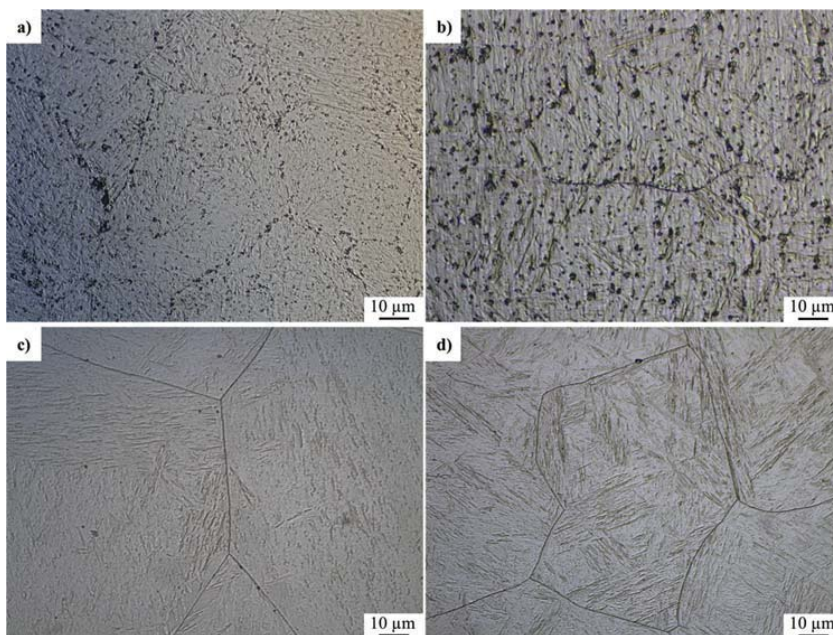


Fig. 5. Light optical micrographs taken with a reduced opening angle of the aperture. All samples were etched with V2A-pickle. Micrograph of a specimen a) austenitized at 990 °C, b) carbide dissolution heat treatment, austenitized at 990 °C, c) austenitized at 1200 °C and d) carbide dissolution heat treatment, austenitized at 1200 °C.

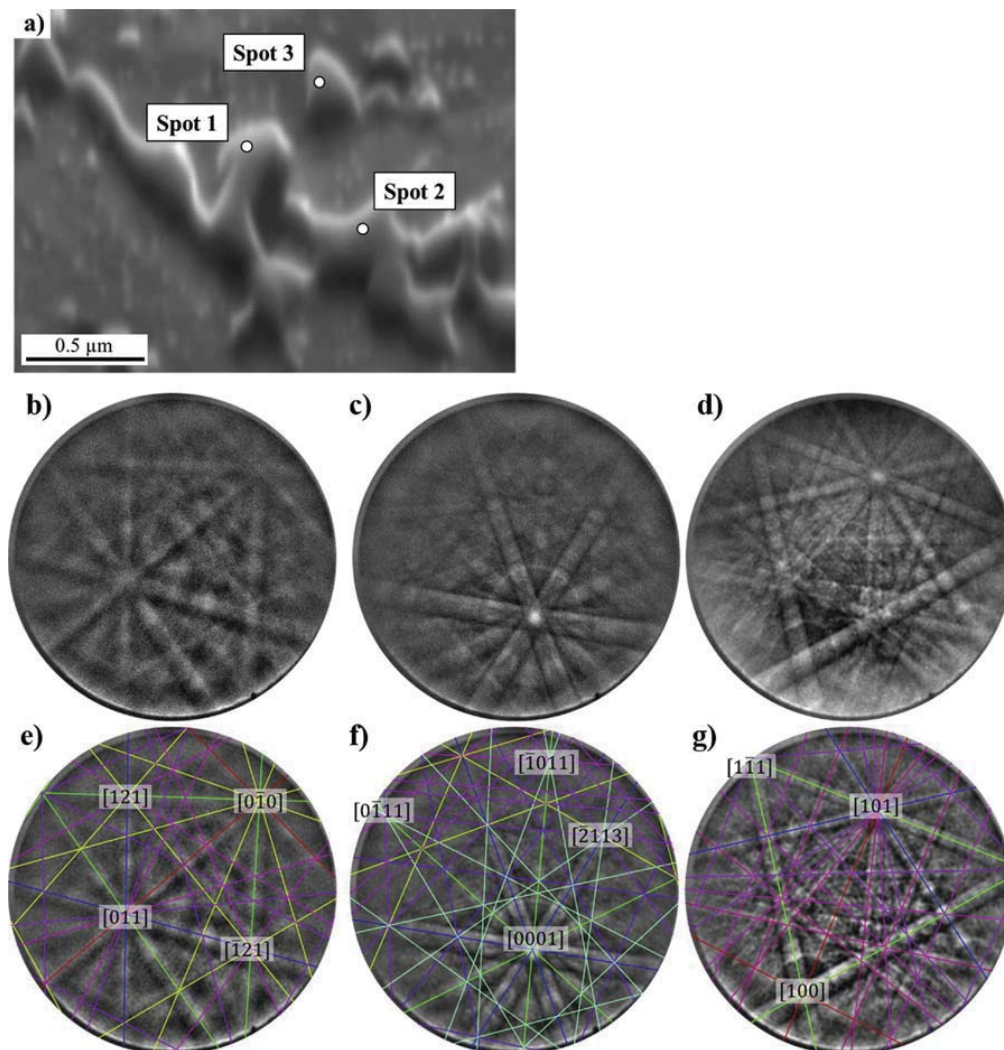


Fig. 6. Characterization of carbides in the as received condition. a) SE SEM micrograph. The spots indicate the locations of the recorded EBSD spot-pattern. b) Pattern obtained at spot 1, c) spot 2 and d) spot 3. e) Indexed solution for MC (spot 1), f) M_2C (spot 2) and g) M_6C (spot 3).

reached after austenitization at 1200 °C and ageing at 500 °C.

Erlach et al. (Erlach et al., 2006, 2007) investigated a dual hardening steel which reached a peak hardness of up to 60 HRC when isothermally aged at 610 °C for 30 min. The austenitization treatment also consisted of annealing at 990 °C for 30 min and quenching in oil. As the alloy investigated in this study contains an increased amount of 0.85 m% V compared to 0.30 m% V in (Erlach et al., 2006), it is concluded that V increases the solvus temperature of primary carbides and thus a higher austenitization temperature is required to reach optimized mechanical properties in terms of hardness. This can also be derived from the light optical micrographs of a specimen austenitized at 990 °C for 30 min, as depicted in Fig. 5 a), where large amounts of undissolved primary carbides are visible. During annealing for 5 min at 1200 °C, all carbides are dissolved and coarsening of the austenite grains takes place, as can be seen in Fig. 5.

The carbide dissolution heat treatment conducted prior to austenitization has no influence on the investigated alloys hardness, as can be determined from the ageing response depicted in Fig. 2.

In the as received condition, carbon is bound in the MC, M_2C and

M_6C carbides visible in Figs. 3 a) and 6. The characterization of carbides using EBSD spot-patterns obtained from specimens subjected to a carbide dissolution heat treatment shows that the same types of carbides are present. However, the carbides do change their morphology from beading-like spherical to elongated needle-shaped structures occupying prior austenite grain boundaries. During the isothermal segment at 1100 °C in the carbide dissolution heat treatment, M_2C and M_6C dissolve due to their lower solvus temperatures. The dissolution of the M_2C carbides leads to the formation of MC carbides enriched in V. As a consequence of the reduced amount of carbides, the austenite grains coarsen. During the cooling steps, precipitation of coarse M_2C and M_6C from the supersaturated austenite takes place, preferably needleshaped at prior austenite grain boundaries, Figs. 3 b) and 7.

When austenitized at 990 °C, the prior conducted carbide dissolution heat treatment does not increase the hardness or ageing response. It is therefore assumed that during austenitization the amount of C and V dissolved is not increased by the carbide dissolution heat treatment. However, during the annealing at 1100 °C in the carbide dissolution heat treatment, the metastable M_2C dissolve into MC and hence

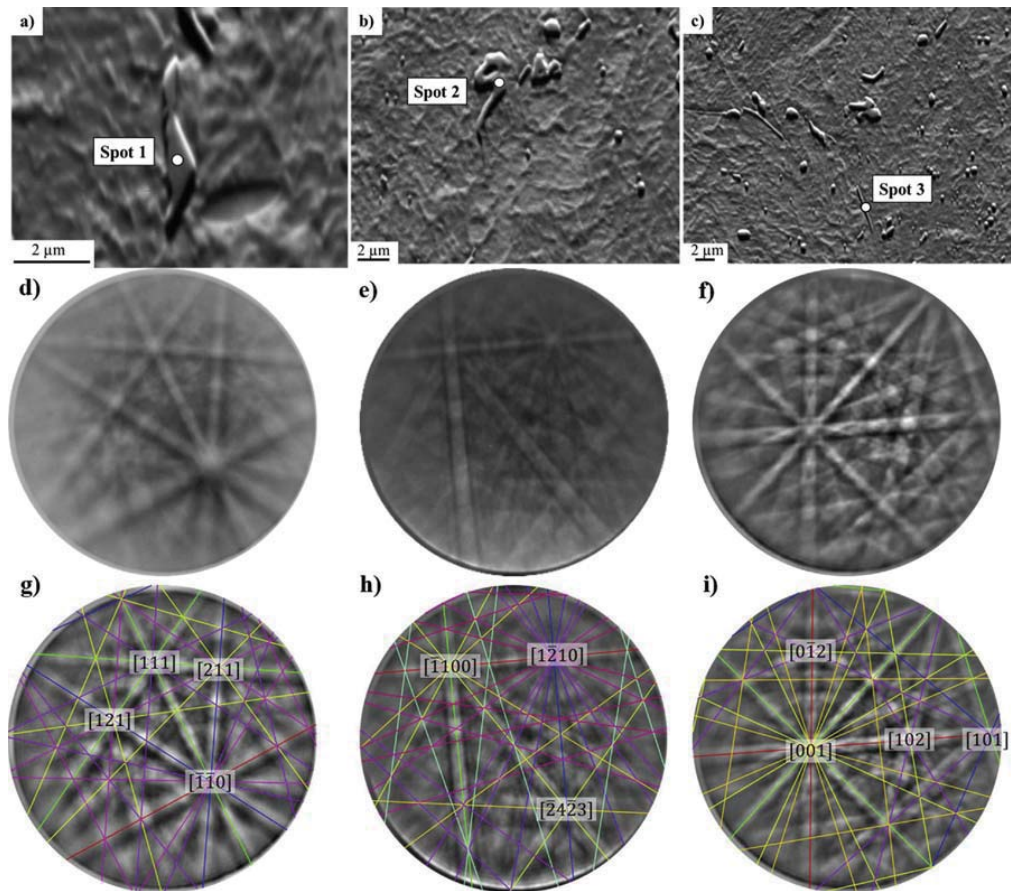


Fig. 7. Characterization of carbides in a specimen subjected to a carbide dissolution heat treatment. a), b) and c) SE SEM micrographs. The spots indicate the locations of the recorded EBSD spot-pattern. d) Pattern obtained at spot 1, e) at spot 2 and f) at spot 3. g) Indexed solution for MC, (spot 1), h) for M_2C (spot 2) and i) for M_6C (spot 3). Note different scale bars.

increase the amount of small spherical MC carbides. This can be attributed to the fact that the solvus temperature of the MC carbides is close to 1100 °C, as was calculated by thermodynamic calculations with MatCalc. It is therefore concluded that at an austenitization temperature of 990 °C the amount of MC carbides dissolved in the austenite is too small to have a significant impact on hardness and ageing response, hence the carbide dissolution heat treatment has no effect.

During the austenitization at 1200 °C, all carbides are dissolved in the austenite, which is why the prior conducted carbide dissolution heat treatment to increase the amount of dissolved MC carbides does not affect the hardness after quenching or the ageing response.

For microstructural characterization, four different preparation methods were used. Fig. 4 a) shows that etching with Kalling I or II is able to reveal the martensitic microstructure. Prior austenite grain boundaries are not visible and carbides cannot be detected in any of the investigated heat treatment conditions. At higher magnifications, pitted areas are visible. These etchants are known to reveal martensitic structures in highalloy and maraging steels (Bramfitt and Benscoter, 2002; Schnitzer et al., 2009; Small et al., 2008), which do not contain carbon and therefore neither carbides. As carbide structures are visible in Figs. 3 and 4 b) to d), where samples were prepared with V2Apickle or polished with colloidal silica, carbides seem to be lost when etched with Kalling I or II. Etching with V2A-pickle leads to the best results for microstructural investigations with the LOM. With a reduced opening angle of the microscopes aperture, both martensitic microstructure and

carbides can be visualized. It should be noted that, because of the uncertain etching time and exact temperature of the etchant, the results are difficult to reproduce. For investigations using SEM and the acquisition of Kikuchi pattern with EBSD, polishing with colloidal silica leads to the best results. Compared to preparation parameters reported in literature, reduced polishing times improved the quality of the obtained Kikuchi pattern detected in this study (Katrakova et al., 1998; Laigo et al., 2008).

In the investigated steel, 3 types of carbides were identified by EBSD spot-measurements which are generally known to precipitate in tool steels: MC, M_2C and M_6C (Roberts et al., 2010). In the as received condition, all three types of carbides could be measured. After a carbide dissolution heat treatment, schematically depicted in Fig. 1, the same types of carbides were detected. However, after an austenitization at 990 °C and ageing at 450 °C, only MC and M_6C were identified. A summary of the identified carbides in each heat treatment step is given in Table 4.

As reported in (Kim et al., 2015), the investigation of the evolution of primary carbides in different heat treatment conditions of a coldwork tool steel containing 7.9 m% Cr and 1.2 m% Mo revealed the carbides MC, M_2C , M_6C , M_7C_3 and $M_{23}C_6$. The MC carbides were enriched in Nb and Mo and remained stable during the entire thermomechanical process. The amount of Mo in the MC carbides continuously decreased during the conducted heat treatments. M_2C carbides were detected in the as-cast state as well as after heating to hot deformation

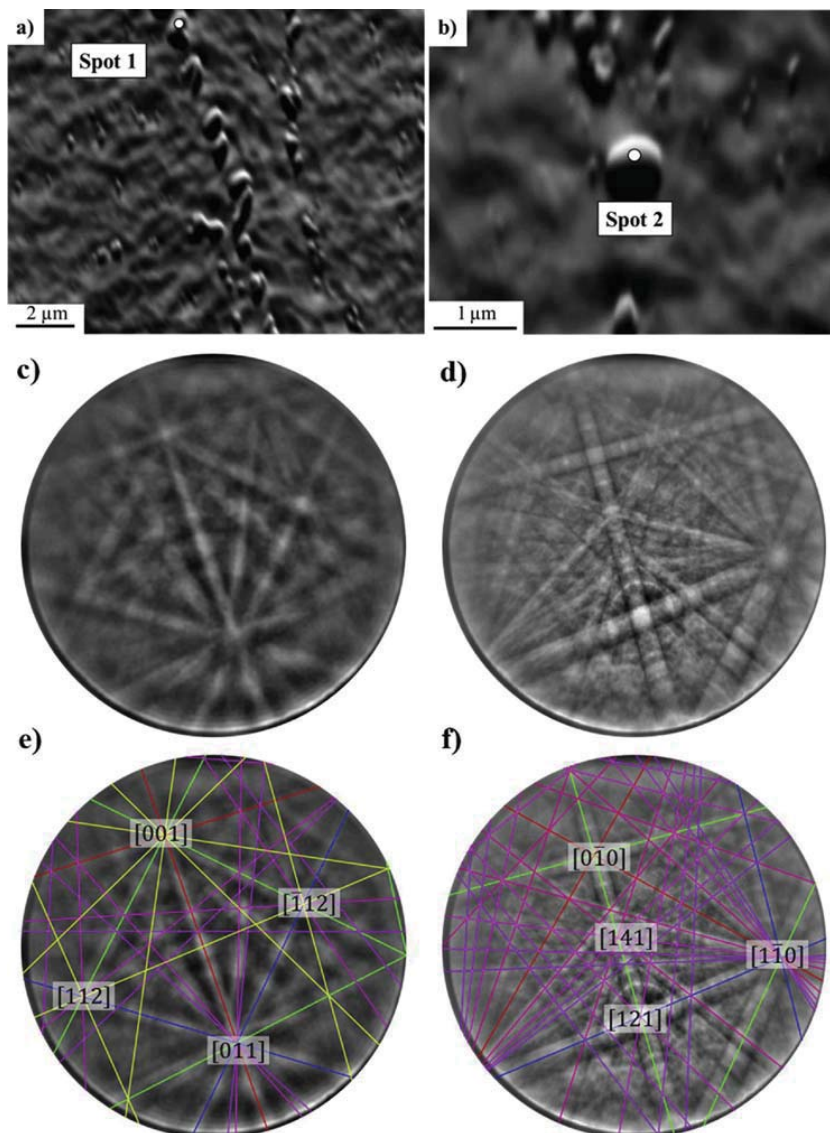


Fig. 8. Characterization of carbides in a specimen austenitized at 990 °C and aged at 450 °C. a) And b) SE SEM micrographs. The spots indicate the locations of the recorded EBSD spot-patterns. c) Patterns obtained at spot 1 and d) at spot 2. e) Indexed solution for MC (spot 1) and f) for M_6C (spot 2).

Table 4
Overview of investigated heat treatment conditions and carbides present in each condition.

Heat treatment condition	Carbide types
As received	MC, M_2C , M_6C
Carbide dissolution	MC, M_2C , M_6C
Austenitized and aged	MC, M_6C

temperature. Only after mechanical deformation at elevated temperatures, the metastable M_2C carbides were dissolved (Kim et al., 2015).

In agreement with these findings, the content of Mo and Cr in the primary carbides in this study is reduced during the carbide dissolution heat treatment, as was observed by EDX measurements and is also evident by the change in relative mass contrast to the iron matrix in Fig. 3.

Furthermore, the detected carbides showed an increased content of V, suggesting the dissolution of M_2C carbides in thermodynamic stable MC and M_6C . Located at prior austenite grain boundaries, metastable M_2C could be detected after the carbide dissolution heat treatment. It can therefore be concluded that the thermal treatment without mechanical deformation is insufficient to dissolve all of the metastable M_2C carbides in the investigated alloy.

5. Conclusions

In this study, the effects of different heat treatment parameters on microstructure evolution and secondary hardness of a dual hardening steel were investigated. Two different austenitization treatments as well as a carbide dissolution heat treatment prior to austenitization were conducted. Different preparation methods were tested in order to

visualize the microstructure using LOM and SEM. Carbides present in different heat treatment conditions were characterized by EBSD spot-measurements. The following conclusions can be drawn:

- The investigated dual hardening steel shows a secondary hardening peak in the temperature range from 400 °C to 600 °C. A carbide dissolution heat treatment leads to no improvement of the mechanical properties. Raising the austenitization temperature from 990 °C for 30 min to 1200 °C for 5 min leads to an increase of the peak hardness from 668 ± 1 HV10 to 741 ± 8 HV10. At the higher austenitization temperature, coarsening of the austenite grains takes place.
- Preparation with V2A-pickle leads to the best results for microstructural investigations using LOM, although exact reproduction of the preparation is difficult. For investigations using the SEM and recording Kikuchi patterns of carbides, polishing with colloidal silica for 30 s to 60 s leads to the best results.
- For a complete understanding of the heat treatment process, characterization of the microstructure in different heat treatment conditions is necessary. Acquisition of EBSD spot-pattern is a powerful tool for carbide characterization. However, high resolution techniques are necessary to investigate the intermetallic NiAl-precipitates.
- In the as received condition as well as after the carbide dissolution heat treatment, MC, M₂C and M₆C carbides are present. These carbides tend to occupy prior austenite grain boundaries in beading-like or needle-shaped morphologies. After the ageing treatment, the carbides MC and M₆C are present, whereas the metastable M₂C carbide could not be detected. When austenitized at 1200 °C for 5 min, all carbides are dissolved.

Acknowledgements

Funding of the Austrian BMVIT (846933) in the framework of the program “Production of the future” and the “BMVIT Professorship for Industry” is gratefully acknowledged.

References

- Bellot, C., Lamesle, P., Delagnes, D., 2013. XRD synchrotron study of carbide precipitation in martensitic steels during tempering. *Acta Metall. Sin. (Engl. Lett.)* 26 (5), 553–557.
- Bischof, M., Erlach, S., Staron, P., Leitner, H., Scheu, C., Clemens, H., 2005. Combining complementary techniques to study precipitates in steels. *MEKU* 96 (9), 1074–1080.
- Blumenauer, H. (Ed.), 2001. *Werkstoffprüfung, 6., Stark überarb. Und Erw. Aufl. Ed. Dt. Verl. Für Grundstoffindustrie. Wiley-VCH, Stuttgart, Weinheim*, pp. 426.
- Bramfitt, B.L., Benschoter, A.O., 2002. *Metallographer's Guide: Practices and Procedures for Irons and Steels, 1. Print Ed. ASM International, Materials Park, Ohio*, pp. 354.
- Brandis, H., Haberling, E., Ortmann, R., Weigand, H.H., 1977. Einfluß des siliciumgehaltes auf die Gefügeausbildung eines schnellarbeitsstahles der sorte S 6-5-2. *Archiv für das Eisenhüttenwesen* 48 (8), 437–442.
- Danoix, F., Danoix, R., Akre, J., Grellier, A., Delagnes, D., 2011. Atom probe tomography investigation of assisted precipitation of secondary hardening carbides in a medium carbon martensitic steels. *J. Microsc.* 244 (3), 305–310.
- Delagnes, D., Pettinari-Sturmel, F., Mathon, M.H., Danoix, R., Danoix, F., Bellot, C., Lamesle, P., Grellier, A., 2012. Cementite-free martensitic steels: a new route to develop high strength/high toughness grades by modifying the conventional precipitation sequence during tempering. *Acta Mater.* 60 (16), 5877–5888.
- Edmonds, D.V., Pereloma, E. (Eds.), 2012. *Diffusionless Transformations, High Strength Steels, Modelling and Advanced Analytical Techniques. Woodhead Pub, Cambridge*, pp. 648.
- Erlach, S.D., Leitner, H., Bischof, M., Clemens, H., Danoix, F., Lemarchand, D., Siller, L., 2006. Comparison of NiAl precipitation in a medium carbon secondary hardening steel and C-free PH13-8 maraging steel. *Mater. Sci. Eng. A* 429 (1-2), 96–106.
- Erlach, S.D., Danoix, F., Leitner, H., Auger, P., Siller, L., Clemens, H., 2007. Precipitation reactions during the early stages of aging in a Ni and Al alloyed martensitic medium carbon steel. *Surf. Interface Anal.* 39 (2-3), 213–220.
- Fournelle, R.A., Grey, E.A., Fine, M.E., 1976. Fatigue behavior of a precipitation hardening Ni–Al–Cu medium carbon steel. *MTA* 7 (5), 669–682.
- Garrison, W.M., Bhat, M.S., 1988. An approach to developing an alternative hot work die steel. *MTA* 19 (7), 1751–1760.
- Katrakova, D., Maas, C., Hohenlein, D., Mücklich, F., 1998. Experiences on contrasting microstructure using orientation imaging microscopy. *PM* 35, 4–20.
- Kim, H., Kang, J.-Y., Son, D., Lee, T.-H., Cho, K.-M., 2015. Evolution of carbides in cold-work tool steels. *Mater. Charact.* 107, 376–385.
- Laigo, J., Tancret, F., Le Gall, R., Furtado, J., 2006. EBSD phase identification and modeling of precipitate formation in HP alloys. *AMR* 15-17, 702–707.
- Laigo, J., Christien, F., Le Gall, R., Tancret, F., Furtado, J., 2008. SEM, EDS, EPMA-WDS and EBSD characterization of carbides in HP type heat resistant alloys. *Mater. Charact.* 59 (11), 1580–1586.
- Leitner, H., Bischof, M., Clemens, H., Erlach, S., Sonderegger, B., Kozeschnik, E., Svoboda, J., Fischer, F.D., 2006. Precipitation behaviour of a complex steel. *Adv. Eng. Mater.* 8 (11), 1066–1077.
- Leitner, H., Schober, M., Schnitzer, R., 2010. Splitting phenomenon in the precipitation evolution in an Fe–Ni–Al–Ti–Cr stainless steel. *Acta Mater.* 58 (4), 1261–1269.
- Lichtenegger, G., 1995. *Entstehung Und Stabilität Des M2C-Eutektikums in Schnellarbeitsstählen. Dissertation, Leoben*.
- Perrut, M., Mathon, M.-H., Delagnes, D., 2012. Small-angle neutron scattering of multi-phase secondary hardening steels. *J. Mater. Sci.* 47 (4), 1920–1929.
- Peruš, I., Terčelj, M., Godec, M., Kugler, G., 2017. Improving of hot workability and expanding the temperature range of safe hot working for M35 high-speed steel. *Mater. Tehnol.* 51 (3), 485–491.
- Petzow, G., 1977. *Metallographisches ätzen. Von G. Petzow. Mat.-wiss. u. Werkstofftech.* 8 (2), 68.
- Ping, D.H., Ohnuma, M., Hirakawa, Y., Kadoya, Y., Hono, K., 2005. Microstructural evolution in 13Cr–8Ni–2.5Mo–2Al martensitic precipitation-hardened stainless steel. *Mater. Sci. Eng. A* 394 (1-2), 285–295.
- Pippel, E., Woltersdorf, J., Pöckl, G., Lichtenegger, G., 1999. Microstructure and nanochemistry of carbide precipitates in high-speed steel S 6-5-2-5. *Mater. Charact.* 43 (1), 41–55.
- Roberts, G.A., Krauss, G., Kennedy, R., 2010. *Tool Steels, 5. Ed. Ed. ASM International, Materials Park, OH*, pp. 364.
- Schnitzer, R., Hochfellner, R., Nöhner, M., Schober, M., Clemens, H., Zinner, S., Leitner, H., 2009. Mikrostrukturelle Charakterisierung von PH 13-8 Mo maraging-stählen. *PM* 46 (10), 521–536.
- Schober, M., Schnitzer, R., Leitner, H., 2009. Precipitation evolution in a Ti-free and Ti-containing stainless maraging steel. *Ultramicroscopy* 109 (5), 553–562.
- Schober, M., Lerchbacher, C., Eidenberger, E., Staron, P., Clemens, H., Leitner, H., 2010. Precipitation behavior of intermetallic NiAl particles in Fe-6 at.%Al-4 at.%Ni analyzed by SANS and 3DAP. *Intermetallics* 18 (8), 1553–1559.
- Seetharaman, V., Sundararaman, M., Krishnan, R., 1981. Precipitation hardening in a PH 13-8 Mo stainless steel. *Mater. Sci. Eng.* 47 (1), 1–11.
- Small, K.B., Englehart, D.A., Christman, T.A., 2008. Guide to etching specialty alloys. *Adv. Mater. Processes* 166, 32–37.

Paper II

M. Hofinger, M. Ognianov, C. Turk, H. Leitner, R. Schnitzer

Early Stages of Precipitate Formation in a Dual Hardening Steel

Journal of Heat Treatment and Materials 74 (2019) 293–301.

DOI: 10.3139/105.110390

Early stages of precipitate formation in a dual hardening steel

Matthias Hofinger¹, Miloslav Ognianov², Christoph Turk², Harald Leitner²,
Ronald Schnitzer¹

1 Montanuniversität Leoben, Department of Physical Metallurgy and Materials Testing,
Franz-Josef-Straße 18, 8700 Leoben, Austria

2 voestalpine Böhler Edelstahl GmbH & Co KG, Mariazellerstraße 25, 8605 Kapfenberg,
Austria

Abstract

For plastic mold steels, secondary hardening as well as hardenable, corrosion-resistant steels are used. Secondary hardening can be achieved through alloying with Ni, Ti, Al and Cu. The precipitation sequence of combined Cu and intermetallic NiAl particles depends on the precise ratio of the alloying contents.

In this study, a dual hardening iron-based alloy with a high ratio of Ni/Cu and Al/Cu and low C content is investigated. These dual hardening steels represent alloys that utilize both carbidic and intermetallic secondary hardening precipitations to achieve secondary hardening. The investigations focus on the initial precipitation of intermetallic particles in order to analyze the sequence of precipitate formation for a specific ratio of alloying elements. DSC measurements were used to identify characteristic precipitation temperatures between 360 °C and 600 °C and the corresponding heat treatment conditions were reproduced using a quenching dilatometer. The initial stages of precipitate formation were examined using high-resolution atom probe tomography. C-enrichments in the form of retained austenite films were evident in the examined material. Heterogeneous nucleation of Cu-NiAl precipitates on these retained austenite films was attributed to exothermal reactions at 460 °C.

M. Hofinger, M. Ognianov, C. Turk, H. Leitner, R. Schnitzer

Early Stages of Precipitate Formation in a Dual Hardening Steel*

Frühe Stadien der Ausscheidungsbildung eines dualhärtenden Stahls

Abstract/Kurzfassung

For plastic mold steels, secondary hardening as well as hardenable, corrosion-resistant steels are used. Secondary hardening can be achieved through alloying with Ni, Ti, Al and Cu. The precipitation sequence of combined Cu and intermetallic NiAl particles depends on the precise ratio of the alloying contents. In this study, a dual hardening iron-based alloy with a high ratio of Ni/Cu and Al/Cu and low Carbon content is investigated. These dual hardening steels represent alloys that utilize both carbidic and intermetallic secondary hardening precipitates to achieve secondary hardening. The investigations focus on the initial precipitation of intermetallic particles in order to analyze the sequence of precipitate formation for a specific ratio of alloying elements. DSC measurements were used to identify characteristic precipitation temperatures between 360 °C and 600 °C and the corresponding heat treatment conditions were reproduced using a quenching dilatometer. The initial stages of precipitate formation were examined using high-resolution atom probe tomography. C-enrichments in the form of retained austenite films were evident in the examined material. Heterogeneous nucleation of Cu-NiAl precipitates on these retained austenite films was attributed to exothermal reactions at 460 °C. ■

Keywords: Dual hardening steel, differential scanning calorimetry, continuous heat treatment, atom probe tomography, intermetallic NiAl precipitates

Für Kunststoffformenstähle werden neben härtbaren, korrosionsbeständigen auch ausscheidungshärtbare Stähle eingesetzt. Zur Ausscheidungshärtung werden unter anderem Legierungselemente wie Ni, Ti, Al und Cu eingesetzt. In Kombination hängt die Ausscheidungssequenz von Cu-Partikeln und intermetallischen NiAl-Teilchen von deren genauem Legierungsverhältnis ab. In dieser Arbeit wurde eine dualhärtende Eisenbasislegierung mit einem hohen Verhältnis von Ni/Cu und Al/Cu und geringen Legierungsgehalten an Kohlenstoff untersucht. Bei diesen dualhärtenden Stählen handelt es sich um Legierungen, die karbidische und intermetallische Sekundärhärteauscheidungen zur Festigkeitssteigerung nutzen. Der Fokus der Untersuchungen wurde dabei auf die zuerst ausgeschiedenen intermetallischen Teilchen gelegt, um bei gegebenem Verhältnis der Legierungselemente die Sequenz der Ausscheidungsbildung zu analysieren. Die charakteristischen Ausscheidungstemperaturen wurden mithilfe von DSC-Messungen zwischen 360 °C und 600 °C identifiziert und die jeweiligen Wärmebehandlungszustände in einem Abschreckdilatometer reproduziert. Anschließend wurden die ersten Stadien der Ausscheidungsbildung mit hochauflösender Atomsondentomographie untersucht. In dem untersuchten Material konnten C-Anreicherungen in Form von Restaustenitfilmen nachgewiesen werden. Eine exotherme Reaktion bei 460 °C konnte der heterogenen Keimbildung von Cu-NiAl-Ausscheidungen an diesen Restaustenitfilmen zugeordnet werden. ■

Schlüsselwörter: Dualhärtender Stahl, Dynamische Differenzkalorimetrie, Kontinuierliche Wärmebehandlung, Atomsondentomographie, Intermetallische NiAl-Ausscheidungen

Authors/Autoren: Dipl.-Ing. Matthias Hofinger, Univ.-Prof. Dr. Ronald Schnitzer, Department Werkstoffwissenschaft, Montanuniversität Leoben, Franz-Josef-Straße 18, 8700 Leoben, Austria, matthias.hofinger@unileoben.ac.at (Corresponding author/Kontakt)
Dipl.-Ing. Miloslav Ognianov, Dr. Christoph Turk, Priv.-Doz. Dr. Harald Leitner, voestalpine Böhler Edelstahl GmbH & Co KG, Kapfenberg, Austria

HOW TO CITE THIS ARTICLE: M. Hofinger et al.: Early Stages of Precipitate Formation in a Dual Hardening Steel. HTM J. Heat Treatm. Mat. 74 (2019) 5, pp. 293-301, DOI:10.3139/105.110390

* Lecture presented at the ASMET Werkstofftechnik- und Härtereitagung 2019, March 28-29, 2019, Vienna, Austria

1 Introduction

Dual hardening steels utilize precipitation of carbidic and intermetallic particles to achieve secondary hardening [1, 2]. To avoid competitive precipitation reactions, these intermetallic phases comprise alloying elements without high affinity towards carbon. Both Ni and Al, forming the ordered intermetallic NiAl phase, as well as Cu are used. Cr, Mo and V are used as carbide forming alloying elements [3, 4]. The intermetallic NiAl phase has an ordered B2 structure and precipitates coherent to the ferritic iron matrix. This coherence causes fast precipitation kinetics of high particle densities of spherical, homogeneously distributed precipitates [5–8]. In α -iron, precipitation of Cu starts with the formation of bcc Cu clusters. These clusters exhibit high Fe contents, reducing the interfacial energy to the iron matrix and thus the critical nucleation energy. Extended ageing results in the formation of Cu-rich fcc precipitates [9, 10]. Due to the fast precipitation kinetics of NiAl and Cu, these particles can act as heterogeneous precipitation sites for secondary hardening carbides [11, 12]. This accelerates precipitation kinetics and leads to a more homogeneous distribution of secondary hardening carbides, improving mechanical properties such as strength and toughness of dual hardening steels [13]. In combination, the precipitation sequence of Cu and intermetallic NiAl particles depends on the alloying ratio of Ni/Cu and Al/Cu. If low ratios of Ni/Cu and Al/Cu are present, precipitation starts with the formation of Cu particles. The interfacial energy and thus the critical nucleation energy is reduced through Ni enrichments at the interface to the iron matrix [14–16]. This will subsequently lead to the heterogeneous nucleation of NiAl precipitates [17–19]. However, if a high ratio of these alloying elements is present, precipitation starts with the nucleation of NiAl particles [20]. These are often enriched in Mn and Cu. Especially Cu reduces the lattice parameter and thus the critical nucleation energy of NiAl in α -Fe [21]. Although these different individual precipitation sequences have been described in the literature, a threshold value at which the precipitation sequences shifts is currently unknown. Since the alloying contents in the investigated alloy lie between the two described cases, this study investigates the initial stages in order to determine the sequence of precipitation between Cu and NiAl in a dual hardening steel with high ratios of Ni/Cu and Al/Cu.

2 Experimental methods

Table 1 shows the chemical composition of the investigated alloy. The DSC measurements were performed using a Labsys DSC instrument by SETARAM Instrumentation. Specimens with 200 mg were heated to 650 °C with a heating rate of 20 °C/min. Ar was used as measuring atmosphere, with a gas flow of 50 ml/min during heating and 200 ml/min during cooling. The tests were

1 Einleitung

Dualhärtende Stähle nutzen sowohl karbidische als auch intermetallische Sekundärhärteausscheidungen zur Festigkeitssteigerung [1, 2]. Diese intermetallischen Phasen bestehen aus Legierungselementen ohne hohe Affinität zu Kohlenstoff, um in keiner Konkurrenz zur Karbidbildung zu stehen. Dafür genutzt werden sowohl Ni und Al, welche die geordnete intermetallische Phase NiAl bilden, als auch Cu. Als karbidbildende Legierungselemente werden Cr, Mo und V genutzt [3, 4]. Die intermetallische Phase NiAl besitzt eine geordnete B2-Struktur und scheidet sich kohärent zur ferritischen Eisenmatrix aus. Aufgrund dieser Kohärenz weist sie eine schnelle Ausscheidungskinetik auf, die zu einer hohen Dichte von sphärischen, homogen verteilten Teilchen führt [5–8]. In α -Eisen beginnt die Ausscheidungsbildung von Cu mit der Bildung von krz-Cu-Clustern. Diese weisen einen hohen Gehalt an Fe auf, welcher die Grenzflächenenergie zur Eisenmatrix und damit die kritische Keimbildungsarbeit reduziert. Erst bei längerer Auslagerungsdauer kommt es in weiterer Folge zur Bildung von kfz-Cu-reichen Ausscheidungen [9, 10]. Durch ihre schnelle Ausscheidungskinetik fungieren NiAl- oder Cu-Ausscheidungen in Kombination mit Sekundärhärtekarbiden als heterogene Keimbildungsstellen für die Karbide [11, 12]. Dies resultiert in einer beschleunigten Ausscheidungskinetik und homogenen Verteilung der Sekundärhärtekarbide und wirkt sich dadurch positiv auf die mechanischen Eigenschaften wie der Festigkeit und Zähigkeit von dualhärtenden Stählen aus [13]. In Kombination ist die Ausscheidungssequenz von Cu und intermetallischen NiAl-Partikeln abhängig vom Legierungsverhältnis Ni/Cu und Al/Cu. Liegt ein niedriges Verhältnis von Ni/Cu und Al/Cu vor, so beginnt die Ausscheidungsbildung mit der Entstehung von Cu-Partikeln. Durch die Anreicherung von Ni in der Grenzschicht zur Eisenmatrix kann die Grenzflächenenergie und damit die Keimbildungsarbeit reduziert werden [14–16]. Dies führt in weiterer Folge zur heterogenen Keimbildung von NiAl-Ausscheidungen [17–19]. Liegt stattdessen ein hohes Verhältnis dieser Legierungselemente vor, werden zuerst NiAl-Partikel gebildet [20]. In diese werden bevorzugt Mn und Cu eingebaut. Vor allem Cu führt zu einer Reduktion des Gitterparameters und setzt so die kritische Keimbildungsarbeit für NiAl in α -Fe herab [21]. Obwohl die unterschiedlichen Ausscheidungssequenzen in der Literatur bereits eindeutig beschrieben sind, ist kein Grenzwert bekannt, ab dem die Änderung der Ausscheidungssequenz auftritt. Da die Legierungsverhältnisse der in dieser Arbeit untersuchten Legierung zwischen den beiden beschriebenen Fällen liegen, wurden hier die ersten Stadien der Ausscheidungsbildung analysiert, um die Sequenz der Ausscheidungsbildung zwischen Cu und NiAl in einem dualhärtenden Stahl mit hohem Verhältnis von Ni/Cu und Al/Cu zu beobachten.

2 Experimentelle Methoden

Die chemische Zusammensetzung der untersuchten Legierung ist in Tabelle 1 angegeben. Die DSC-Messungen wurden mit einem DSC-Gerät Labsys von SETARAM Instrumentation durchgeführt. Dabei wurden Proben mit einer Masse von 200 mg verwendet und mit einer Heizrate von 20 °C/min auf eine Temperatur von 650 °C erhitzt. Als Messatmosphäre wurde Ar mit einer Durchflussrate von 50 ml/min

	C	Cr	Ni	Al	Cu	Mn	Si	Fe	Ni/Cu	Al/Cu
wt. %	0.13	0.4	3.5	1.2	1.2	2.0	0.3	bal.	2.9	1.0

Table 1. Nominal composition of the investigated alloy and information on the Ni/Cu and Al/Cu ratios

Tabelle 1. Nominelle Zusammensetzung der untersuchten Legierung und Angabe des Ni/Cu- bzw. Al/Cu-Verhältnisses

performed on solution-annealed materials to render the precipitation reactions visible.

A DIL 805A dilatometer by Bähr Thermoanalyse GmbH was used for heat treatment of the samples prior to hardness measurements and atom probe investigations. Specimens were solution-annealed for 30 min at 900 °C, followed by quenching with He with $t_{8/5} = 5$ s. Subsequently samples were heated with a constant rate of 20 °C/min to 460 °C and quenched with He to room temperature within 14 s. Hardness was measured in HV10 on metallographic cross sections. The given values are the mean and standard deviation of three individual measurements. From the dilatometer samples, 0.3 mm × 0.3 mm × 8 mm rods were cut and atom probe tips prepared electrolytically. 25 % Perchloric in acetic acid was used as the electrolyte for the first step. The final etching was performed in a microloop in 2 % perchloric acid in 2-Butoxyethanol [22, 23]. Atom probe measurements were carried out using a LEAP 3000X HR at 40 K in laser mode with 0.2 nJ laser energy and a frequency of 250 kHz. The CAMECA® IVAS 3.6.14 software was used for reconstruction and data evaluation. For measurements including interfaces, the k-factor was altered in order to avoid arching of the interfaces. For measured volumes without such microstructural features, reconstruction was performed with standard software parameters (image compression factor 1.65, k-factor 3.3). Analyses showed superposition of Al_{27}^{1+} with Fe_{54}^{2+} at 27 Da (Dalton, atomic mass unit per Coulomb) and Ni_{58}^{2+} with Fe_{58}^{2+} at 29 Da. After peak decomposition by natural isotope abundance, the peak at 27 Da was ranged as Fe_{54}^{2+} and at 29 Da ranged as Ni_{58}^{2+} [24].

während der Heizsegmente und 200 ml/min zur Kühlung verwendet. Um die Ausscheidungsreaktionen sichtbar zu machen, wurden die Untersuchungen an lösungsgeglühtem Material durchgeführt.

Die Wärmebehandlung der Proben für Härtemessungen und Atomsondenuntersuchungen erfolgte in einem Dilatometer DIL 805A der Bähr Thermoanalyse GmbH. Das Probenmaterial wurde bei einer Temperatur von 900 °C für 30 min lösungsgeglüht und anschließend mit $t_{8/5} = 5$ s mit He abgeschreckt. Darauf folgend wurden die Proben mit einer konstanten Heizrate von 20 °C/min auf eine Temperatur von 460 °C erhitzt und mit He in 14 s auf Raumtemperatur abgeschreckt. Zur Härtemessung wurden metallographische Schläffe hergestellt und die Härte nach Vickers (HV10) gemessen. Jeder angegebene Wert entspricht dem Mittel aus drei Einzelmessungen. Aus den Dilatometerproben wurden anschließend Stäbchen mit 0.3 mm × 0.3 mm × 8 mm gefertigt und elektrolytisch Atomsondenspitzen präpariert. Als Elektrolyt für den ersten Präparationsschritt wurde 25 %ige Perchlorsäure in Essigsäure verwendet. Das Anspitzen erfolgte mithilfe einer Microloop in 2 %iger Perchlorsäure in 2-Butoxyethanol [22, 23]. Atomsondenmessungen wurden mit einer LEAP 3000X HR bei 40 K im Lasermode mit einer Laserenergie von 0,2 nJ und Frequenz von 250 kHz durchgeführt. Die Rückkonstruktion und Auswertung erfolgte mit dem Programm IVAS 3.6.14 von CAMECA®. Im Falle von Messungen, die eine Grenzfläche beinhalteten, wurde die Rückkonstruktion mithilfe des k-Faktors so angepasst, dass diese geradlinig verlaufen und keine Wölbung aufweisen. Bei gemessenen Volumen ohne entsprechenden Gefügebestandteilen erfolgte die Rückkonstruktion anhand von Standard-Parametern der Software (Image Compression Factor 1,65, k-Factor 3,3). Bei der Auswertung wurde eine Überlagerung des Messsignals für Al_{27}^{1+} mit Fe_{54}^{2+} bei 27 Da (Dalton, atomare Masseneinheit pro Coulomb) und Ni_{58}^{2+} mit Fe_{58}^{2+} bei 29 Da festgestellt. Eine Aufteilung gemäß der natürlichen Isotopenverteilung führte zu einer Festlegung des Signals bei 27 Da als Fe_{54}^{2+} und bei 29 Da als Ni_{58}^{2+} [24].

3 Results and discussion

Figure 1a shows the heat flow during heating of the DSC measurement. Figure 1b shows the first derivative of the heat flow versus the temperature. The red curve in 1a shows the results of the hardness measurements on the dilatometer samples. The steep initial fall of the DSC signal can be ascribed to transient phenomena at the start of the measurement. A weak pronounced local minimum is evident in the temperature range from 200 to 300 °C. First signs of exothermal reactions are visible at 330 °C and 370 °C. The weak nature of these reactions leads to the assumption that these are no precipitation reactions yet. Two pronounced exothermal reactions, partially overlapping and difficult to distinguish, are evident at

3 Ergebnisse und Diskussion

In Bild 1a ist der Wärmefluss während des Aufheizvorgangs der DSC-Messung dargestellt, Bild 1b zeigt die 1. Ableitung des Wärmeflusses nach der Temperatur. Die rote Kurve in 1a zeigt die Ergebnisse der Härtemessungen an den Dilatometerproben. Der steile Abfall zu Beginn des DSC-Signals ist auf Einschwingvorgänge während des Starts der Messung zurückzuführen. Im Temperaturbereich von 200–300 °C zeigt sich ein schwach ausgeprägtes lokales Minimum. Bei einer Temperatur von 330 °C und 370 °C zeigen sich erste Anzeichen von exothermen Reaktionen. Aufgrund der geringen Ausprägung dieser Reaktionen wird davon ausgegangen, dass es sich hierbei um keine Ausscheidungs Vorgänge handelt. Bei

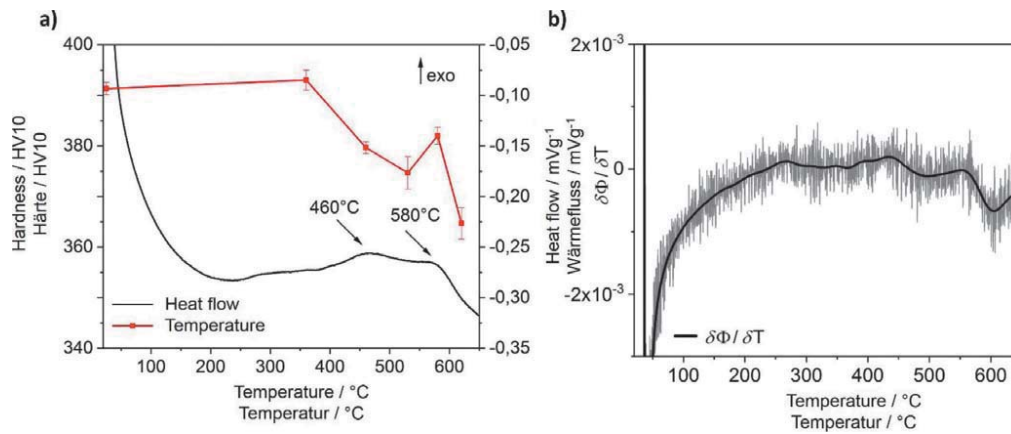


Fig. 1. a) Heat flow during heating of the DSC measurement with a constant heating rate of 20 °C/min. Two exothermal reactions at 460 °C and at 580 °C are distinguishable. For the hardness measurements samples were heat treated in a dilatometer up to the corresponding temperature at the same heating rate. b) 1st derivative of the heat flow. Solid line: smoothed by moving average (weighted)

Bild 1. a) Wärmefluss während des Aufheizvorgangs der DSC-Messung, konstante Heizrate von 20 °C/min. Bei 460 °C und 580 °C sind zwei exotherme Reaktionen zu erkennen. Für die Härtemessungen: Proben mit derselben Heizrate bis zur entsprechenden Temperatur in einem Dilatometer wärmebehandelt. b) 1. Ableitung des Wärmeflusses, durchgezogene Linie: Glättung mit gleitendem Durchschnitt (gewichtet)

460 °C and 580 °C. Since prior studies have shown the precipitation of Cu to be an exothermal reaction [25], it is assumed that this reaction is indicative of the first occurrence of precipitation in the investigated alloy. Further high resolution investigations were thus performed on specimens in the quenched state and on samples heated with a constant heating rate to 460 °C. Hardness results show that up to a temperature of 360 °C, no hardness loss is caused by tempering. Between 360 °C and 460 °C the initial hardness of 391 ± 1 HV10 drops to 380 ± 2 HV10. Although exothermal reactions are evident at this ageing temperature, no hardness increase is visible. At an ageing temperature of 580 °C a slight increase in hardness to 382 ± 2 HV10 occurs. The second exothermal reaction is thus associated with the formation of secondary hardening precipitates.

Table 2 shows the comparison between the nominal chemical composition and the composition as measured by atom probe. To prevent the effect of selective C enrichments, the chemical compo-

460 °C sowie bei 580 °C sind zwei ausgeprägte exotherme Reaktionen zu erkennen, welche teilweise überlappen und nicht eindeutig voneinander differenzierbar sind. Da aus der Literatur bekannt ist, dass es sich bei der Ausscheidung von Cu um eine exotherme Reaktion handelt [25], wird davon ausgegangen, dass es sich bei dieser Reaktion um das erste Auftreten von Ausscheidungsvorgängen in der untersuchten Legierung handelt. Aus diesem Grund wurden die weiteren hochauflösenden Untersuchungen im abgeschreckten Zustand und bei einer kontinuierlichen Wärmebehandlung bis zu 460 °C durchgeführt. Die Härteergebnisse zeigen, dass bis zu einer Temperatur von 360 °C bei einer kontinuierlichen Auslagerung kein Härteverlust durch Anlasseneffekte auftritt. Erst zwischen 360 °C und 460 °C kommt es zu einem Abfall der Ansprunghärte von 391 ± 1 HV10 auf 380 ± 2 HV10 bei 460 °C. Obwohl bei dieser Auslagerungstemperatur bereits eine exotherme Reaktion erkennbar ist, tritt keine Härtesteigerung auf. Bei einer Auslagerungstemperatur von 580 °C steigt die Härte neuerlich geringfügig auf 382 ± 2 HV10 an. Die zweite exotherme Reaktion wird deshalb mit der Bildung von festigkeitssteigernden Sekundärhärteauscheidungen in Verbindung gebracht.

Tabelle 2 zeigt den Vergleich zwischen der nominellen und der mit Atomsonde gemessenen chemischen Zusammensetzung. Zur Bestimmung der chemischen Zusammensetzung wurde ein Mess-

	C	Cr	Ni	Al	Cu	Mn	Si	Fe	Ni/Cu	Al/Cu
at% nominal	0.6	0.4	3.3	2.4	1.0	2.0	0.6	bal.	3.2	2.4
at% measured	0.54	0.35	3.41	2.58	0.89	1.64	0.56	bal.	3.8	2.9

Table 2. Chemical composition in at% and Ni/Cu and Al/Cu ratios, nominal and measured by atom probe

Tabelle 2. Nominelle und mit Atomsonde gemessene chemische Zusammensetzung in At%, sowie Verhältnis von Ni/Cu und Al/Cu

sition was determined on a selected measurement with no microstructural inhomogeneities. Table 2 shows that the Ni/Cu and Al/Cu ratios measured by atom probe tomography are increased compared to the nominal composition, which, according to the literature, favors the precipitation of NiAl as opposed to Cu [26].

Figure 2a depicts the reconstruction of an atom probe measurement after solution annealing and quenching. Only the C atoms are shown for improved visibility. Two laminar C enrichments are evident running roughly parallel to the z-axis of the measurement. In the lower part of the volume, a wider pronounced, orthogonal C enrichment is visible. The actual shape is shown in the image rotated 90° about the z-axis. Figure 2b shows the concentration profile along the cylinder Profile 1 with a volume of 20 nm × 20 × 55 nm. The C enrichments reach up to between 1.5 at% and 0.9 at%. The other alloying elements are distributed evenly along the profile; the fluctuations in the concentrations of the elements Al, Ni and Mn can be attributed to the small volume of the cylinder. The morphology and C-content are indicative of martensite lath boundaries. Figure 2c shows the concentration profile along the z-axis of Profile 2, with a volume of 25 nm × 25 nm × 55 nm. As already visible in the reconstruction, the C enrichment is more pronounced, reaching up to 7 at%. The Al concentration decreases from 2.2 at% at the edge of the profile (2.58 at% in the matrix, Table 2) to 1.6 at% inside the C enrichment. The other alloying elements are evenly distributed along the concentration profile. The high C concentration and decreased Al content give rise to the assumption that the described inhomogeneity is a retained austenite film [27, 28]. The existence of retained austenite films may be explained by the lack of tempering in this condition. The diffusion and enrichment of C at martensite grain boundaries takes place

volumen ohne mikrostruktureller Inhomogenitäten gewählt, um dem Einfluss von selektiven C-Anreicherungen vorzubeugen. Aus Tabelle 2 ist ersichtlich, dass in den Atomsondenmessungen im Vergleich zur nominellen Zusammensetzung ein erhöhtes Verhältnis von Ni/Cu und Al/Cu vorliegt, wodurch laut Literatur die Bildung von NiAl gegenüber Cu-Ausscheidungen bevorzugt wird [26].

In Bild 2a ist die Rückkonstruktion einer Atomsondenmessung nach Lösungsglühen und Abschrecken dargestellt. Zur besseren Sichtbarkeit werden lediglich die C-Atome gezeigt. Sichtbar sind zwei flächenförmige C-Anreicherungen, welche parallel zur z-Achse der Messung verlaufen, sowie eine breiter ausgeprägte C-Anreicherung im unteren Bereich, nahezu normal dazu. In der um 90° um die z-Achse gedrehten Darstellung wird die tatsächliche Ausprägung sichtbar. In Bild 2b ist das Konzentrationsprofil entlang des Zylinders Profil 1 mit einem Volumen von 20 nm × 20 × 55 nm gezeigt. Darin ist ersichtlich, dass die C-Anreicherungen auf bis zu 1,5 At% bzw. 0,9 At% reichen. Die übrigen Legierungselemente zeigen einen gleichmäßigen Verlauf entlang des Profils, die Schwankungen in den Konzentrationsprofilen der Elemente Al, Ni und Mn sind auf das geringe Zylindervolumen zurückzuführen. Durch die Morphologie und den C-Gehalt wird angenommen, dass es sich hierbei um Martensit-Lattengrenzen handelt. Bild 2c zeigt das Konzentrationsprofil entlang der z-Achse von Profil 2 mit einem Volumen von 25 nm × 25 nm × 55 nm. Die C-Anreicherung ist, wie bereits in der Rückkonstruktion sichtbar, deutlicher ausgeprägt und erreicht bis zu 7 At% C. Die Konzentration von Al fällt von 2,2 At% am Rande des Profils (2,58 At% in der Matrix, Tabelle 2) zu 1,6 At% im Inneren der C-Anreicherung ab. Die weiteren Legierungselemente zeigen eine gleichmäßige Verteilung entlang des Konzentrationsprofils. Aufgrund der hohen C-Konzentration und der Abnahme des Gehaltes von Al wird davon aus-

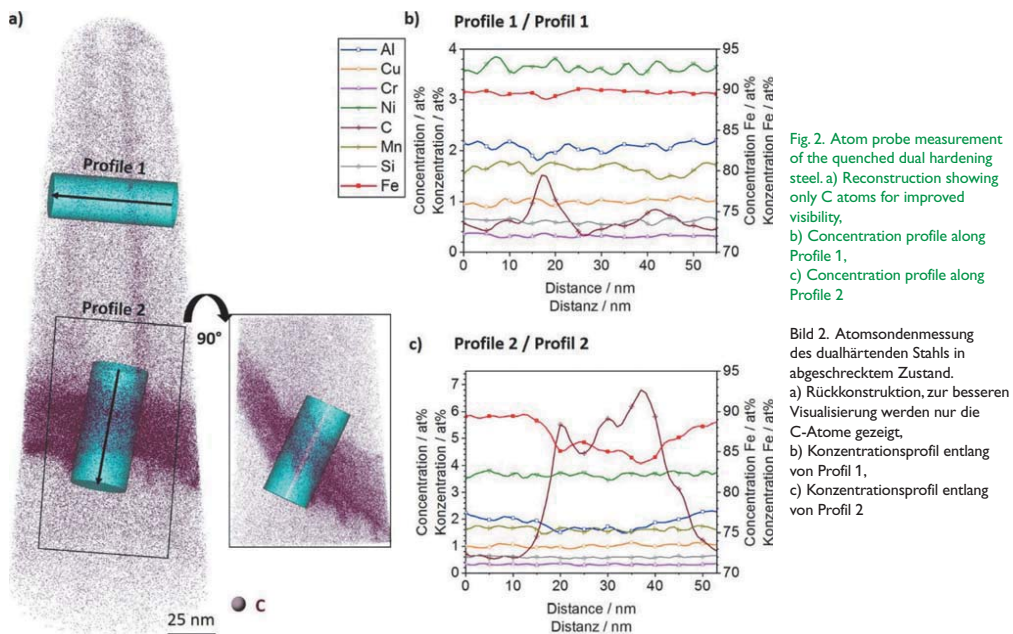


Fig. 2. Atom probe measurement of the quenched dual hardening steel. a) Reconstruction showing only C atoms for improved visibility, b) Concentration profile along Profile 1, c) Concentration profile along Profile 2

Bild 2. Atomsondenmessung des dualhärtenden Stahls in abgeschrecktem Zustand. a) Rückkonstruktion, zur besseren Visualisierung werden nur die C-Atome gezeigt, b) Konzentrationsprofil entlang von Profil 1, c) Konzentrationsprofil entlang von Profil 2

during quenching from the austenitization temperature of 900 °C with $t_{8/5} = 5$ s. For these inhomogeneous microstructures, comparing the distribution of solute atoms such as Cu, Ni and Al, to a random frequency distribution utilizing the Pearson coefficient [29], does not produce meaningful results. No clusters were found when applying the isosurface method. It may thus be assumed that, although diffusion of C and Al (enrichment or repulsion from retained austenite films) occurs during quenching, such diffusion is not sufficient for cluster formation.

Figure 3 shows a reconstruction of an atom probe measurement of a sample continuously aged to 460 °C. Figure 3a shows the 3-D reconstruction with each point representing a measured C atom. Concentration ranges of $(\text{Ni}+\text{Al}) > 7$ at% and $\text{Cu} > 5$ at% are shown in green and orange, respectively. The C enriched regions have a two-dimensional shape and are arranged approximately parallel to each other in the measured volume. Figure 3b shows the 1-D concentration profile along Profile 1. The C enrichment reaches a concentration of 6–9 at% and a layer thickness of ~5 nm. This leads to the conclusion the described microstructural features are in fact carbon enriched retained austenite films [27, 28]. Figure 3a also shows local enrichments of Ni, Al and Cu, preferentially located in close proximity to the retained austenite films.

gegangen, dass es sich hierbei um einen Restaustenitfilm handelt [27, 28]. Das Vorhandensein von Restaustenitfilmen lässt sich durch die fehlende Anlassbehandlung dieses Zustandes erklären. Die Diffusion und Anreicherung von C an Martensit-Lattengrenzen tritt bereits während des Abschreckens von der Austenitisierungstemperatur von 900 °C mit $t_{8/5} = 5$ s auf. Die Verteilung der Legierungsatome Cu, Ni und Al führt im Vergleich mit einer zufälligen Häufigkeitsverteilung mithilfe des Pearson-Koeffizienten [29] im Fall von solch inhomogenen Mikrostrukturen zu keinen aussagekräftigen Ergebnissen. Mithilfe der Isosurface-Methode konnten keine Cluster nachgewiesen werden. Es wird daher angenommen, dass es während des Abschreckens zwar bereits zur Diffusion von C und Al (Anreicherung bzw. Verdrängung aus den Restaustenitfilmen) kommt, diese Diffusion aber nicht für eine Clusterbildung ausreicht.

Die rückkonstruierte Atomsondenmessung einer kontinuierlich bis 460 °C ausgelagerten Probe ist in Bild 3 dargestellt. Bild 3a zeigt die 3-D-Rückkonstruktion, wobei jeder Punkt ein gemessenes C-Atom repräsentiert. In grün und orange sind Konzentrationsbereiche von $(\text{Ni}+\text{Al}) > 7$ At% und $\text{Cu} > 5$ At% dargestellt. Anreicherungen von C weisen eine flächige Struktur auf und liegen etwa parallel zueinander in dem gemessenen Volumen. Bild 3b zeigt das 1-D-Konzentrationsprofil entlang von Profil 1. Die C-Anreicherung weist eine Konzentration von 6–9 At% und eine Schichtdicke von ~5 nm auf. Daraus ist zu schließen, dass es sich hierbei um an Kohlenstoff angereicherte Restaustenitfilme handelt [27, 28]. In Bild 3a befinden sich des Weiteren lokale Anreicherungen von Ni, Al und Cu, bevorzugt in der Nähe der Rest-

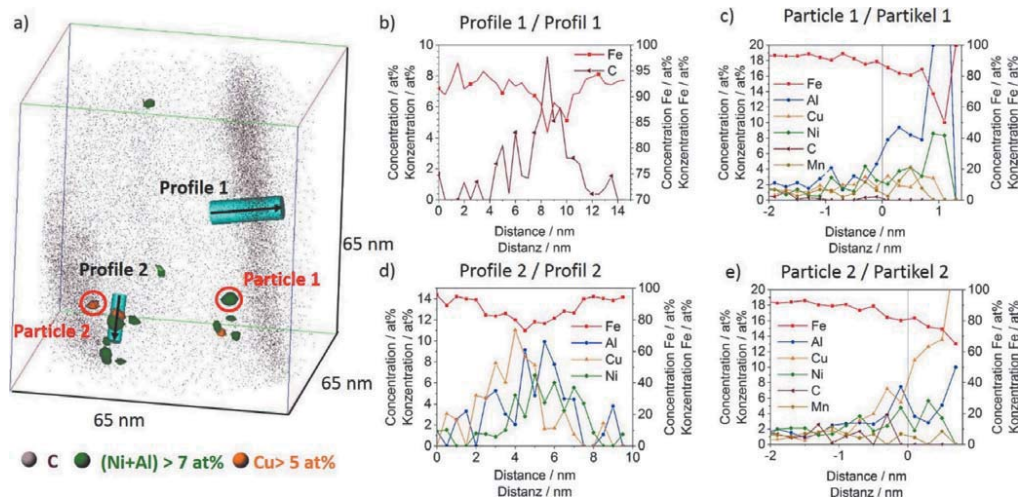


Fig. 3. Excerpt of an atom probe measurement, sample continuously heated to 460 °C with 20 °C/min. a) Reconstruction showing the C atoms. Green areas: Concentration ranges of $(\text{Ni}+\text{Al}) > 7$ at%, orange areas: $\text{Cu} > 5$ at%. The depicted volume is an excerpt of a measurement, edge length of 65 nm. b) Fe and C concentration along Profile 1. c) Radially averaged distribution of concentrations around Particle 1, particle surface marks the origin of the abscissa-axis. d) Fe, Al, Cu and Ni concentrations along Profile 2. e) Radially averaged distribution of concentrations around Particle 2, particle surface marks the origin of the abscissa-axis

Bild 3. Auszug einer Atomsondenmessung, Probe kontinuierlich mit 20 °C/min auf 460 °C erhitzt. a) Rückkonstruktion mit Darstellung der C-Atome. In grün: Konzentrationsbereiche von $(\text{Ni}+\text{Al}) > 7$ At%, in orange: $\text{Cu} > 5$ At%. Das Volumen ist ein Auszug einer Messung; Kantenlänge von 65 nm. b) Konzentrationsprofil von Fe und C entlang von Profil 1. c) Radial gemittelte Konzentrationsverteilung um Partikel 1, Partikeloberfläche als Ursprung der Abszissenachse. d) Konzentrationsprofil von Fe, Al, Cu und Ni entlang von Profil 2. e) Radial gemittelte Konzentrationsverteilung um Partikel 2, Partikeloberfläche als Ursprung der Abszissenachse

Figure 3c shows a radially averaged distribution of concentrations around such a particle. However, due to the superposition of Al and Fe at 27 Da and Ni and Fe at 29 Da the amount of Al is systematically underestimated and that of Ni overestimated. The chemical composition of these early precipitates is thus impossible to determine precisely. Local Cu enrichments occur in the form of combined Cu-NiAl precipitations as evident in the 1-D concentration profile in Figure 3d and the radially averaged distribution of concentrations around Particle 2 in Figure 3e.

First indications of exothermal reactions are evident in the DSC curve in Figure 1 around temperatures of 330 °C and 370 °C. Based on the atom probe measurements shown in Figures 2 and 3, the decomposition of retained austenite may be excluded. No secondary hardening carbides were evident in measurements of higher tempered conditions. Literature shows that nucleation of secondary hardening carbides in dual hardening steels preferentially starts heterogeneously at intermetallic precipitates [12, 13]. It may thus be assumed that the sequence of precipitation starts with the formation of intermetallic particles. The exothermal reactions in this temperature range can thus neither be attributed to the decomposition of retained austenite nor to the formation of secondary hardening carbides. A pronounced exothermal maximum, accompanied by a decrease in hardness, occurs at 460 °C. Thus at this ageing temperature no strengthening precipitates are formed. However, the exothermal reaction could be explained by the formation of Cu clusters. Such clusters, not accompanied by an increase in hardness, were found at ageing temperatures between 200 °C and 460 °C by *Primig et al.* [25, 30]. The measurements performed within the framework of this study show no homogeneous cluster formation in the iron matrix at an ageing temperature of 460 °C. Heterogeneous nucleation on retained austenite films is, however, indicative of initial precipitation reactions. Since these precipitates have high contents of Cu, Ni and Al they may be considered as combined Cu-NiAl precipitates. Compared to homogeneous precipitation within the iron matrix, heterogeneous precipitation at the grain boundaries occurs accelerated. No secondary hardening carbides were evident in the examined conditions, despite the high diffusion of C. It is assumed that homogeneous precipitation of Cu and NiAl is limited to higher ageing temperatures. It was shown that the sequence of heterogeneous nucleation is not clear-cut, since precipitations were observed as combined Cu-NiAl particles even in the very early stages.

4 Summary

This study examined the early stages of precipitate formation in dual hardening steels. DSC measurements showed that, for a constant heating rate of 20 °C/min, initial precipitation reactions occurred at a temperature of 460 °C. The maximum hardness of 393 ± 2 HV10 was measured at an ageing temperature of 360 °C. The hardness for higher ageing temperatures initially fell to 375 ± 3 HV10 before it increased again to 382 ± 2 HV10 at 580 °C,

austenitfilme. Eine radial gemittelte Konzentrationsverteilung um solch einen Partikel ist in Bild 3c dargestellt. Hierbei sei erwähnt, dass aufgrund einer Überlagerung des Messsignals für Al und Fe bei 27 Da und Ni und Fe bei 29 Da der Anteil von Al systematisch unterschätzt und von Ni überschätzt wird. Eine exakte Bestimmung der chemischen Zusammensetzung dieser frühen Ausscheidungsstadien ist aus diesem Grund nicht möglich. Die lokalen Anreicherungen von Cu treten in Form von kombinierten Cu-Ni-Al-Ausscheidungen auf, wie sie in einem 1-D-Konzentrationsprofil in Bild 3d und radial gemittelter Konzentrationsverteilung um Partikel 2 in Bild 3e ersichtlich sind.

In der DSC-Kurve in Bild 1 treten im Temperaturbereich von 330 °C und 370 °C erste Anzeichen von exothermen Reaktionen auf. Mithilfe der Atomsondenmessungen, dargestellt in den Bildern 2 und 3, kann der Zerfall von Restaustenit ausgeschlossen werden. Sekundärhärtekarbide konnten in keiner Messung von höheren Anlasszuständen nachgewiesen werden. Aus der Literatur ist bekannt, dass sich Sekundärhärtekarbide in dualhärtenden Stählen bevorzugt an intermetallischen Ausscheidungen bilden [12, 13]. Deshalb kann angenommen werden, dass die Ausscheidungssequenz mit der Bildung der intermetallischen Phasen beginnt. Es wird also ausgeschlossen, dass die exothermen Reaktionen in diesem Temperaturbereich dem Zerfall von Restaustenit oder der Bildung von Karbiden zugeordnet werden können. Bei 460 °C tritt ein erstes deutlich ausgeprägtes exothermes Maximum auf, welches allerdings von einem Abfall der Härte begleitet wird. Bei dieser Auslagerungstemperatur kommt es daher nicht zur Bildung von festigkeitssteigernden Ausscheidungen. Die exotherme Reaktion kann möglicherweise durch die Bildung von Cu-Clustern erklärt werden. Diese wurden von *Primig et al.* bei Temperaturen zwischen 200 °C und 460 °C nachgewiesen und wurden nicht von einer Härtesteigerung begleitet [25, 30]. Die Messungen im Rahmen dieser Untersuchung zeigten bei einer Auslagerungstemperatur von 460 °C keine homogene Clusterbildung in der Eisenmatrix. Erste Ausscheidungen konnten jedoch durch heterogene Keimbildung an Restaustenitfilmen nachgewiesen werden. Diese Ausscheidungen weisen einen hohen Gehalt an Cu, Ni und Al auf und können daher als kombinierte Cu-NiAl-Ausscheidung betrachtet werden. Die heterogene Ausscheidungsbildung an den Korngrenzen läuft im Vergleich zur Ausscheidungsbildung in der Eisenmatrix beschleunigt ab. Trotz der hohen Diffusion von C konnten in den untersuchten Zuständen keine Sekundärhärtekarbide nachgewiesen werden. Es wird angenommen, dass die homogene Ausscheidungsbildung von Cu und NiAl erst bei höheren Auslagerungstemperaturen beginnt. Im Falle der heterogenen Keimbildung konnte nachgewiesen werden, dass keine eindeutige Sequenz vorliegt, sondern die Ausscheidungen bereits in den frühen Stadien als kombinierte Cu-NiAl-Partikel vorliegen.

4 Zusammenfassung

In dieser Arbeit wurden die frühen Stadien der Ausscheidungsbildung in einem dualhärtenden Stahl untersucht. Mithilfe von DSC-Messungen wurde das erste Auftreten von Ausscheidungsreaktionen bei einer konstanten Heizrate von 20 °C/min bei einer Temperatur von 460 °C festgestellt. Die Maximalhärte von 393 ± 2 HV10 wurde bei einer Auslagerungstemperatur von 360 °C gemessen. Bei erhöhten Auslagerungstemperaturen fällt zunächst

remaining below the level of maximum hardness. The initial exothermal reaction at 460 °C can be explained by heterogeneous nucleation of Cu-NiAl clusters, thus depleting the iron matrix from alloying elements and leading to a reduced hardness. The second exothermal reaction at 580 °C can, in the context of increasing hardness, be associated with the formation of secondary hardening precipitates.

Atom probe measurements after quenching found C enrichments in the form of retained austenite films. For continuous ageing with 20 °C/min to 460 °C, heterogeneous precipitated Cu-NiAl particles were measured in close proximity to retained austenite films. No homogeneous precipitation could be detected within the iron matrix.

Acknowledgements

Funding of the Austrian BMVIT in the framework of the program "Production of the future" and the "BMVIT Professorship for Industry" is gratefully acknowledged.

Literatur

- Garrison, W. M.; Bhat, M. S.: An approach to developing an alternative hot work die steel. *Metall. Trans. A* 19 (1988) 7, pp. 1751-1760, DOI:10.1007/bf02645143
- Erlach, S. D.; Leitner, H.; Bischof, M.; Clemens, H.; Danoix, F.; Lemarchand, D.; Siller, I.: Comparison of NiAl precipitation in a medium carbon secondary hardening steel and C-free PH13-8 maraging steel. *Mater. Sci. Eng. A* 429 (2006) 1-2, pp. 96-106, DOI:10.1016/j.msea.2006.05.071
- Roberts, G. A.; Krauss, G.; Kennedy, R.: *Tool steels*, 5th ed., ASM International, Materials Park, OH, USA, 2010. – ISBN: 978-0-87170-599-0
- Hofinger, M.; Staudacher, M.; Ognianov, M.; Turk, C.; Leitner, H.; Schmitzer, R.: Microstructural evolution of a dual hardening steel during heat treatment. *Micron* 120 (2019), pp. 48-56, DOI:10.1016/j.micron.2019.02.004
- Seetharaman, V.; Sundaraman, M.; Krishnan, R.: Precipitation hardening in a PH 13-8 Mo stainless steel. *Mater. Sci. Eng.* 47 (1981) 1, pp. 1-11, DOI:10.1016/0025-5416(81)90034-3
- Schmitzer, R.; Hochfellner, R.; Nöhner, M.; Schober, M.; Clemens, H.; Zinner, S.; Leitner, H.: Mikrostrukturelle Charakterisierung von PH 13-8 Mo Maraging-Stählen. *Prac. Metall.* 46 (2009) 10, pp. 521-536, DOI:10.3139/147.110032
- Leitner, H.; Schober, M.; Schmitzer, R.: Splitting phenomenon in the precipitation evolution in an Fe-Ni-Al-Ti-Cr stainless steel. *Acta Mater.* 58 (2010) 4, pp. 1261-1269, DOI:10.1016/j.actamat.2009.10.030
- Schober, M.; Schmitzer, R.; Leitner, H.: Precipitation evolution in a Ti-free and Ti-containing stainless maraging steel. *Ultramicroscopy* 109 (2009) 5, pp. 553-562, DOI:10.1016/j.ultramic.2008.10.016
- Kozeschnik, E.: Thermodynamic prediction of the equilibrium chemical composition of critical nuclei: Bcc Cu precipitation in α -Fe. *Scripta Mater.* 59 (2008) 9, pp. 1018-1021, DOI:10.1016/j.scriptamat.2008.07.008
- Holzer, I.; Kozeschnik, E.: Simulation of Copper Precipitation in Fe-Cu Alloys. *Mater. Sci. Forum* 638-642 (2010), pp. 2579-2584, DOI:10.4028/www.scientific.net/msf.638-642.2579
- Tiemens, B. L.; Sachdev, A. K.; Mishra, R. K.; Olson, G. B.: Three-Dimensional (3-D) Atom Probe Tomography of a Cu-Precipitation-Strengthened, Ultrahigh-Strength Carburized Steel. *Metall. Mat. Trans. A* 43 (2012) 10, pp. 3626-3635, DOI:10.1007/s11661-012-1178-5
- Danoix, F.; Danoix, R.; Akre, J.; Grellier, A.; Delagnes, D.: Atom probe tomography investigation of assisted precipitation of secondary hardening carbides in a medium carbon martensitic steels. *J. microsc.* 244 (2011) 3, pp. 305-310, DOI:10.1111/j.1365-2818.2011.03537.x
- Delagnes, D.; Pettinari-Sturmel, F.; Mathon, M. H.; Danoix, R.; Danoix, F.; Bellot, C.; Lamesle, P.; Grellier, A.: Cementite-free martensitic steels: A new route to develop high strength/high toughness grades by modifying the conventional precipitation

die Härte auf 375 ± 3 HV10, bevor es zu einem neuerlichen Härteanstieg kommt, der mit 382 ± 2 HV10 bei 580 °C aber unter dem Niveau des Härtemaximums liegt. Die erste exotherme Reaktion bei 460 °C wird durch die heterogene Keimbildung von Cu-NiAl-Clustern erklärt, welche zu einer Verarmung der Eisenmatrix an Legierungselementen und dadurch zu einem Härteabfall führen. Die zweite exotherme Reaktion bei 580 °C wird in Kombination mit dem Härteanstieg mit der Bildung festigkeitssteigernder Sekundärhärteausscheidung in Verbindung gebracht.

Mithilfe von Atomsondenmessungen konnten im abgeschreckten Zustand Anreicherungen von C in Form von Restaustenitfilmen nachgewiesen werden. Bei einer kontinuierlichen Auslagerung mit 20 °C/min auf 460 °C wurden heterogen an Restaustenitfilmen ausgeschiedene Cu-NiAl-Ausscheidungen gemessen. Eine homogene Ausscheidungsbildung in der Eisenmatrix konnte nicht nachgewiesen werden.

Danksagung

Für die finanzielle Unterstützung im Rahmen des Programms "Produktion der Zukunft" und der "BMVIT Stiftungsprofessur für Industrie" gilt unser besonderer Dank dem österreichischen Bundesministerium für Verkehr, Innovation und Technologie (BMVIT).

- sequence during tempering. *Acta Mater.* 60 (2012) 16, pp. 5877-5888, DOI:10.1016/j.actamat.2012.07.030
- Isheim, D.; Gagliano, M. S.; Fine, M. E.; Seidman, D. N.: Interfacial segregation at Cu-rich precipitates in a high-strength low-carbon steel studied on a sub-nanometer scale. *Acta Mater.* 54 (2006) 3, pp. 841-849, DOI:10.1016/j.actamat.2005.10.023
- Isheim, D.; Kollí, R. P.; Fine, M. E.; Seidman, D. N.: An atom-probe tomographic study of the temporal evolution of the nanostructure of Fe-Cu based high-strength low-carbon steels. *Scripta Mater.* 55 (2006) 1, pp. 35-40, DOI:10.1016/j.scriptamat.2006.02.040
- Jiao, Z. B.; Luan, J. H.; Zhang, Z. W.; Miller, M. K.; Ma, W. B.; Liu, C. T.: Synergistic effects of Cu and Ni on nanoscale precipitation and mechanical properties of high-strength steels. *Acta Mater.* 61 (2013) 16, pp. 5996-6005, DOI:10.1016/j.actamat.2013.06.040
- Kollí, R. P.; Seidman, D. N.: The temporal evolution of the decomposition of a concentrated multicomponent Fe-Cu-based steel. *Acta Mater.* 56 (2008) 9, pp. 2073-2088, DOI:10.1016/j.actamat.2007.12.044
- Vaynman, S.; Isheim, D.; Kollí, R. P.; Bhat, S. P.; Seidman, D. N.; Fine, M. E.: High-Strength Low-Carbon Ferritic Steel Containing Cu-Fe-Ni-Al-Mn Precipitates. *Metall. Mat. Trans. A* 39 (2008) 2, pp. 363-373, DOI:10.1007/s11661-007-9417-x
- Kapoor, M.; Isheim, D.; Ghosh, G.; Vaynman, S.; Fine, M. E.; Chung, Y.-W.: Aging characteristics and mechanical properties of 1600 MPa body-centered cubic Cu and B2-NiAl precipitation-strengthened ferritic steel. *Acta Mater.* 73 (2014), pp. 56-74, DOI:10.1016/j.actamat.2014.03.051
- Jiao, Z. B.; Luan, J. H.; Miller, M. K.; Liu, C. T.: Precipitation mechanism and mechanical properties of an ultra-high strength steel hardened by nanoscale NiAl and Cu particles. *Acta Mater.* 97 (2015), pp. 58-67, DOI:10.1016/j.actamat.2015.06.063
- Leitner, H.; Schmitzer, R.; Schober, M.; Zinner, S.: Precipitate modification in PH13-8 Mo type maraging steel. *Acta Mater.* 59 (2011) 12, pp. 5012-5022, DOI:10.1016/j.actamat.2011.04.053
- Lefebvre-Ulrikson, W.; Vurpillot, F.; Sauvage, X. (Eds.): *Atom probe tomography: Atom probe tomography: Put theory into practice*. 1st ed., Academic Press, London, UK, 2016. – ISBN 9780128046470
- Gault, B.; Moody, M. P.; Cairney, J. M.; Ringer, S. P.: *Atom probe microscopy*. Springer, New York, NY, USA, 2012. – ISBN 978-1-4614-3436-8
- de Laeter, J. R.; Böhlke, J. K.; de Bièvre, P.; Hidaka, H.; Peiser, H. S.; Rosman, K. J. R.; Taylor, P. D. P.: Atomic weights of the elements. *Review* 2000. *Pure and Appl. Chem.* 75 (2003) 6, pp. 683-800, DOI:10.1351/pac200375060683

25. Primig, S.; Stechauner, G.; Kozeschnik, E.: Early Stages of Cu Precipitation in 15-5 PH Maraging Steel Revisited – Part I: Experimental Analysis. *steel res. int.* **88** (2017) 1, p. 1600084, DOI:10.1002/srin.201600084
26. Jiao, Z. B.; Luan, J. H.; Miller, M. K.; Yu, C. Y.; Liu, C. T.: Group precipitation and age hardening of nanostructured Fe-based alloys with ultra-high strengths. *Scientific reports* **6** (2016) 1, DOI:10.1038/srep21364
27. Lerchbacher, C.; Zinner, S.; Leitner, H.: Atom probe study of the carbon distribution in a hardened martensitic hot-work tool steel X38CrMoV5-1. *Micron* **43** (2012) 7, pp. 818-826, DOI:10.1016/j.micron.2012.02.005
28. Sherman, D. H.; Cross, S. M.; Kim, S.; Grandjean, F.; Long, G. J.; Miller, M. K.: Characterization of the Carbon and Retained Austenite Distributions in Martensitic Medium Carbon, High Silicon Steel. *Metall. Mat. Trans. A* **38** (2007) 8, pp. 1698-1711, DOI:10.1007/s11661-007-9160-3
29. Moody, M. P.; Stephenson, L. T.; Ceguerra, A. V.; Ringer, S. P.: Quantitative binomial distribution analyses of nanoscale like-solute atom clustering and segregation in atom probe tomography data. *Microsc. Res. Techniq.* **71** (2008) 7, pp. 542-550, DOI:10.1002/jemt.20582
30. Primig, S.; Leitner, H.: Transformation from continuous-to-isothermal aging applied on a maraging steel. *Mater. Sci. Eng. A* **527** (2010) 16-17, pp. 4399-4405, DOI:10.1016/j.msea.2010.03.084

Bibliography

DOI:10.3139/105.110390

HTM J. Heat Treatm. Mat.

74 (2019) 5; page 293-301

© Carl Hanser Verlag GmbH & Co. KG

ISSN 1867-2493

Standard ISO

ASTM International

Designation: E1806 – 18

Standard Practice for Sampling Steel and Iron for Determination of Chemical Composition¹

Current edition approved March 15, 2018. Published April 2018.

Originally approved in 1996. Last previous edition approved in 2016 as E1806 – 09 (2016). DOI: 10.1520/E1806-18.

Distributed under ASTM license by Beuth Verlag, Berlin, www.beuth.de

This standard is issued under the fixed designation E1806; the number immediately following the designation indicates the year of original adoption or, in the case of revision, the year of

last revision. A number in parentheses indicates the year of last reapproval. A superscript epsilon (ε) indicates an editorial change since the last revision or reapproval.

This practice covers the sampling of all grades of steel, both cast and wrought, and all types (grades) of cast irons and blast furnace iron for chemical and spectrochemical determination of composition. This practice is similar to ISO 14284.

¹ This practice is under the jurisdiction of ASTM Committee E01 on Analytical Chemistry for Metals, Ores, and Related Materials and is the direct responsibility of Subcommittee E01.01 on Iron, Steel, and Ferroalloys.

Paper III

M. Hofinger, B. Seisenbacher, M. Ognianov, H. Leitner, C. Turk, M. Kapp, R. Schnitzer

Thermomechanical Fatigue Testing of Dual Hardening Tool Steels

steel research int. 3 (2019) 1900423.

DOI: 10.1002/srin.201900423

Thermo-mechanical Fatigue Testing of Dual Hardening Tool Steels

Matthias Hofinger¹, Benjamin Seisenbacher², Miloslav Ognianov³, Harald Leitner³,
Christoph Turk³, Marianne Kapp³, Ronald Schnitzer¹

¹ Department of Materials Science, Montanuniversität Leoben, Franz-Josef-Straße 18, 8700
Leoben, Austria

² Department Product Engineering, Montanuniversität Leoben, Franz-Josef-Straße 18, 8700
Leoben, Austria

³ voestalpine BÖHLER Edelstahl GmbH & Co KG, Mariazellerstraße 25, 8605 Kapfenberg,
Austria

Abstract

Hot-work tool steels are exposed to complex interacting cyclic thermal and mechanical loadings. Due to the combination of strengthening via carbides and intermetallic precipitates, dual hardening steels achieve well-balanced mechanical properties in terms of fatigue strength and fracture toughness. As a result, dual hardening steels have a great potential for hot-work applications.

In this study, out-of-phase thermo-mechanical fatigue tests were used to simulate the loading conditions experienced in hot-work tool steel applications on a laboratory scale. The testing was carried out on Fe-C-Cr-Mo-V and Fe-C-Cr-Mo-V-Ni-Al alloys to compare common 5% Cr and dual hardening hot-work tool steels. The resistance to thermo-mechanical fatigue can therefore be correlated with single or dual hardening. Both alloys experienced softening during the fatigue testing. Atom probe tomography investigations revealed coarsening of the secondary hardening precipitates for both alloys. However, the number density of surface cracks was greater for the 5% Cr hot-work tool steel. The dual hardening steel possessed higher resistance to softening and reached a higher lifetime.

Thermomechanical Fatigue Testing of Dual Hardening Tool Steels

Matthias Hofinger,* Benjamin Seisenbacher, Miloslav Ognianov, Harald Leitner, Christoph Turk, Marianne Kapp, and Ronald Schnitzer

Hot-work tool steels are exposed to complex interacting cyclic thermal and mechanical loadings. Due to the combination of strengthening via carbides and intermetallic precipitates, dual hardening steels achieve well-balanced mechanical properties in terms of fatigue strength and fracture toughness. Therefore, dual hardening steels have a great potential for hot-work applications. Herein, out-of-phase thermomechanical fatigue tests are used to simulate the loading conditions experienced in hot-work tool steel applications on a laboratory scale. The testing is conducted on Fe–C–Cr–Mo–V and Fe–C–Cr–Mo–V–Ni–Al alloys to compare common 5% Cr and dual hardening hot-work tool steels. The resistance to thermomechanical fatigue is therefore correlated with single or dual hardening. Both alloys experience softening during the fatigue testing. Atom probe tomography investigations reveal coarsening of the secondary hardening precipitates for both alloys. However, the number density of surface cracks is greater for the 5% Cr hot-work tool steel. The dual hardening steel possesses higher resistance to softening and reaches a higher lifetime.

thermal shock, and resistance to heat checking.^[1] Heat checks, fine surface crack networks, are the major lifetime limiting factor for tools in die-casting applications. This thermal fatigue can either be caused by alternating stresses that develop due to time-dependent temperature gradients, resulting in external loads. These conditions are called “thermomechanical fatigue” (TMF). In the case of position-dependent temperature gradients, no external loads but residual stresses lead to “thermal stress fatigue.”^[2] When hot material is injected into a die, the thermal expansion of the tool surface is restrained by the cooler core, resulting in compressive stresses in regions close to the surface. When these stresses exceed the yield strength of the tool material, which decreases with increasing temperature, local plastic deformation occurs, resulting

in the formation of residual tensile stresses. During the lifetime of a tool, the accumulated plastic deformation can lead to alternating compressive–tensile stresses with a continuous shift of the mean stress into the tensile region. These loading conditions ultimately lead to the formation of surface crack networks.^[1,3,4]

Influencing factors on heat checking resistance include thermal softening, cyclic softening, development of residual stresses, and the microstructure. Thermal conductivity and the coefficient of thermal expansion influence the resistance against heat checking as well. While the former leads to a more uniform thermal expansion and thus indirectly reduces thermal stresses, the latter has a direct influence on thermal strains and thereby thermal stresses.^[4–6] In the case of low strain ranges, high tensile strength can increase the lifetime during thermal fatigue, whereas in the case of high strain ranges, ductility is more important, and high strength can have a negative effect on the lifetime.^[7] The investigation of different atmospheres during immersion tests of hot-work tool steels in molten Al showed a shift from global oxidation in air and nitrogen to localized oxidation at surface cracks in Ar atmosphere.^[8]

Thermal fatigue was tested by Siller via heating hot-work tool steels by laser irradiation.^[5] It was observed that the maximum surface temperature has a major influence on the thermal fatigue lifetime of hot-work tool steels. For temperatures below 650 °C, the investigated alloys showed cyclic isotropic softening within the first 5000 cycles, depending on the duration of the thermal loading. After this initial stage, the surface hardness remained


1. Introduction

Hot-work tool steels experience harsh operating conditions, which include complex interacting cyclic thermal and mechanical loadings. The physical and mechanical properties necessary to withstand these loading conditions are high red hardness, sufficient hot yield strength, temper resistance, resistance to

M. Hofinger, Prof. R. Schnitzer
Department of Materials Science
Montanuniversität Leoben
Franz-Josef-Straße 18, 8700 Leoben, Austria
E-mail: matthias.hofinger@unileoben.ac.at

B. Seisenbacher
Department Product Engineering
Montanuniversität Leoben
Franz-Josef-Straße 18, 8700 Leoben, Austria

M. Ognianov, Dr. H. Leitner, Dr. C. Turk, Dr. M. Kapp
voestalpine BÖHLER Edelstahl GmbH & Co KG
Mariazellerstraße 25, 8605 Kapfenberg, Austria

 The ORCID identification number(s) for the author(s) of this article can be found under <https://doi.org/10.1002/srin.201900423>.

© 2019 The Authors. Published by WILEY-VCH Verlag GmbH & Co. KGaA, Weinheim. This is an open access article under the terms of the Creative Commons Attribution-NonCommercial License, which permits use, distribution and reproduction in any medium, provided the original work is properly cited and is not used for commercial purposes.

DOI: 10.1002/srin.201900423

constant, and the materials reached a stable condition. For maximum surface temperatures exceeding 650 °C, no stable conditions were met, but continuous softening occurred, associated with the formation of surface crack networks. It was shown that especially prior austenite grain boundaries act as fatigue crack initiation sites.

Thermal fatigue tests are often performed on hot-work tool steels by cyclic induction heating of internally water cooled hollow cylinders^[9,10] or by repeated immersion of internally cooled specimens into a bath of molten Al.^[8,11] TMF tests are conducted by inductive heating of solid or tubular specimens, whereas a certain percentage of the thermal expansion is mechanically suppressed.^[12] However, in literature no data can be found on the TMF behavior of dual hardening steels.

These dual hardening steels represent a promising alloying concept for hot-work applications. Due to their combination of secondary hardening carbides and intermetallic precipitates, high hardness levels of up to 60 Rockwell hardness, scale C can be achieved, whereas the amount of embrittlement caused by large primary carbides is reduced compared with chromium hot-work tool steels.^[13–15]

This study aims to investigate the influence of single and dual hardening on resistance against TMF. Out-of-phase thermomechanical fatigue (OP-TMF) tests have been conducted on a common hot-work tool steel and a dual hardening steel. A test rig developed by Riedler et al.^[16] was used for the fatigue testing. The material behavior under TMF loading conditions was analyzed during the TMF testing by recording the stress–strain hysteresis. The amount of softening was evaluated by room temperature hardness measurements of the tested specimens. The influence of microstructure and oxidation behavior was investigated using light optical microscopy (LOM), scanning electron microscopy (SEM), and atom probe tomography (APT).

2. Experimental Section

The chemical compositions of the investigated alloys are shown in Table 1. The dual hardening alloy A was solution annealed at 990 °C for 30 min, followed by oil quenching to room temperature. Ageing was conducted three times at 585 °C for 3 h. The 5% Cr hot-work tool steel, referred to as alloy B, was austenitized at 1050 °C for 30 min, air cooled to room temperature, and subsequently annealed three times at 620 °C for 2 h. Hardness was measured in Vickers HV 5, and the mean value and standard deviation of three measurements were given for every condition.

Strain-controlled OP-TMF tests were performed on samples produced according to Figure 1. An extensometer length of 12.6 mm was used. For temperature control and measurement, three-point temperature measurement using K-type ribbon

Table 1. Nominal chemical composition of the investigated alloys.

Alloy		C	Cr	Mo	V	Si	Mn	Ni	Al	Fe
A	[wt%]	0.37	3.00	2.50	0.85	0.20	0.25	4.80	1.50	bal.
	[at%]	1.68	3.15	1.42	0.91	0.39	0.25	4.47	3.04	bal.
B	[wt%]	0.50	4.50	3.00	0.60	0.20	0.25			bal.
	[at%]	2.30	4.78	1.73	0.65	0.39	0.25			bal.

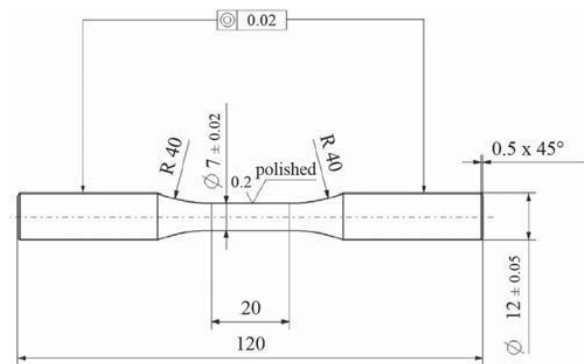


Figure 1. Geometry of the TMF samples, dimensions in mm.

thermocouples located within 20 mm of the center of the specimen was carried out. The thermocouple that was used for temperature control was placed in the center of the specimen and the second and third about 5 mm below and above the central one. Minimum temperature was 200 °C and maximum temperature was 636 ± 6 °C for alloy A and 641 ± 5 °C for alloy B, with a constant heating and cooling rate of 10 °C s⁻¹ and no dwell time. Specimens were heated with a high-frequency induction system and cooled with pressurized air. At the start of each measurement, a zero stress test was performed to obtain the thermal expansion in the desired temperature range. The mean and maximum longitudinal temperature difference was 4 and 11 °C for alloy A and 7 and 24 °C for alloy B.

As shown in Figure 2, a phase shift of 180° between thermal and mechanical loading was used. The strain amplitude was 0.3% and the ratio between thermal and mechanical expansion –0.91 for alloy A and –0.85 for alloy B. A more detailed description of OP-TMF testing^[17] and the test setup used in this investigation can be found in the study by Riedler et al.^[16]

TMF lifetime was determined as suggested by Hähner et al.^[17] As shown in Figure 3a, TMF lifetime was calculated at a drop of 10% below a tangent line drawn at the last point of zero curvature of the maximum tensile stress.

For microstructural analysis, the TMF-tested samples were cut along the longitudinal axis. Metallographic samples were produced using standard grinding and polishing techniques,^[18] with special emphasis on the preservation of the surface oxide layer. Fracture surfaces were investigated with a stereo microscope. Analysis of the TMF-tested microstructure as well as the oxide layer was done with LOM. The 5% Cr hot-work tool steel was etched with 3% HNO₃. Samples of the dual hardening alloy were etched with W2.^[18] The sample surface and formed oxides were investigated with an SEM Zeiss Evo50. High-resolution analysis was performed by APT with a LEAP 3000 XHR. Tips were produced electrolytic by standard techniques.^[19] In the case of TMF-tested specimens, special care was taken to assure the investigated volume was as close as possible to the fracture surface, i.e., in the area of the most precise temperature control. Due to a high number density of large precipitates, which tend to act as fracture sites, measurements were carried out in laser mode at 60 K. Laser pulse energy was set to 0.2 nJ, and a laser frequency and target evaporation rate of 250 kHz and 0.5% were used, respectively.

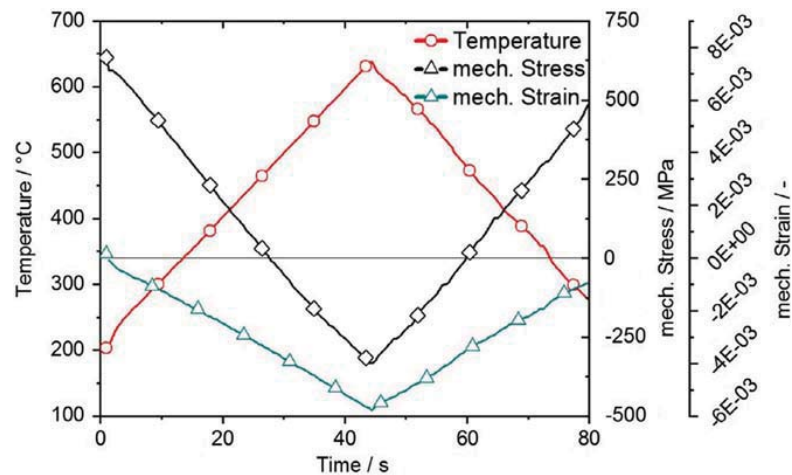


Figure 2. Evolution of the temperature as well as mechanical strain and stress during OP-TMF testing. A phase shift of 180° between thermal and mechanical loading was used.

3. Results and Discussion

3.1. Thermomechanical Fatigue Testing

The results of the TMF tests are shown in Figure 3. For the dual hardening alloy, 2 separate TMF-tests were performed, called alloy A-1 and alloy A-2. The TMF-test alloy B-1 was performed on the 5% Cr hot-work tool steel. In Figure 3a, the maximum tensile stress of each cycle, recorded at minimum temperature of 200 °C, is shown. Figure 3b shows the evolution of the maximum compressive stress, recorded at maximum temperature. Figure 3c,d show the development of the mean stress and the stress amplitude during TMF lifetime. It can be seen that within the first few cycles, high tensile stresses are reached. Alloy B-1 reaches its maximum tensile stress of 894 MPa after 616 cycles. This fast development of high tensile stresses is caused by the plastic deformation during the heating step and simulates the formation of residual tensile stresses during application. After the peak value is reached, the maximum tensile stress decreases continuously, which is attributed to thermal softening. After roughly 2500 cycles, the maximum tensile stress shows a rapid drop, which is correlated with the growth of macroscopic fatigue cracks.

The dual hardening alloy A-1 reaches its peak tensile stress of 878 MPa at 1869 cycles, and the rate of increase of the maximum tensile stress within the first cycles shows a more continuous behavior. The test of alloy A-2 reaches a significant higher lifetime compared with alloy A-1. The deviation between the two stress signals starts at cycle 330, with alloy A-2 experiencing a less steep change of the stress amplitude and mean stress. This can be attributed to a deviation from the desired maximum testing temperature of 623 ± 10 °C for alloy A-2 and 636 ± 6 °C for alloy A-1. Due to the lower temperature and subsequent mechanical loading, the specimen alloy A-2 takes longer to reach a comparable overaged state, resulting in an increased lifetime. Thus, the fatigue test of alloy A-2 reaches its maximum tensile

stress of 844 MPa at 3954 cycles and peak stress amplitude of 497 MPa at 4012 cycles.

Due to the deviations during the tests, further investigations will be limited to the TMF-tests of alloy A-1 and alloy B-1. The slope of the decreasing maximum tensile stress after the maximum value is reached is lower for alloy A-1 than for alloy B-1, indicating a reduced amount of thermal softening. Therefore, alloy A-1 shows a higher TMF lifetime of 4169 cycles compared with 2587 cycles for alloy B-1.

The peak value of the maximum compressive stress shown in Figure 3b is -703 MPa for alloy A-1 and -664 MPa for alloy B-1. Both alloys reach the maximum compressive stress and thus the most severe plastic deformation at cycle number 2. The evolution of the maximum compressive stress is similar to the maximum tensile stress for both alloys. The lowest value before the determined lifetime of the respective alloy is reached is -139 MPa at 1767 cycles for alloy A-1 and -160 MPa at 655 cycles for alloy B-1.

The mean stress in Figure 3c shows a rapid shift into the tensile region, resulting in alternating tensile-compressive loadings. Considering that during the OP-TMF testing the thermal expansion during heating is suppressed, this behavior is indicative of plastic deformation and comparable to the formation of residual tensile stresses. In the evolution of the stress amplitude shown in Figure 3d, softening of both of the investigated materials can be observed. For the first 1200 cycles, the stress amplitude is higher for alloy B-1 and reaches a maximum value of 532 MPa at 616 cycles. The peak amplitude is 511 MPa for alloy A-1 and reached at 1256 cycles. However, the slope of the decreasing stress amplitude is greater for alloy B-1. As the decrease in the stress amplitude is a measure of softening, it is concluded that the dual hardening alloy A possesses a higher resistance against softening in the OP-TMF setup, resulting in the increased lifetime compared with alloy B. This thermomechanical softening is attributed to overaging and coarsening of the microstructure and secondary hardening precipitates.

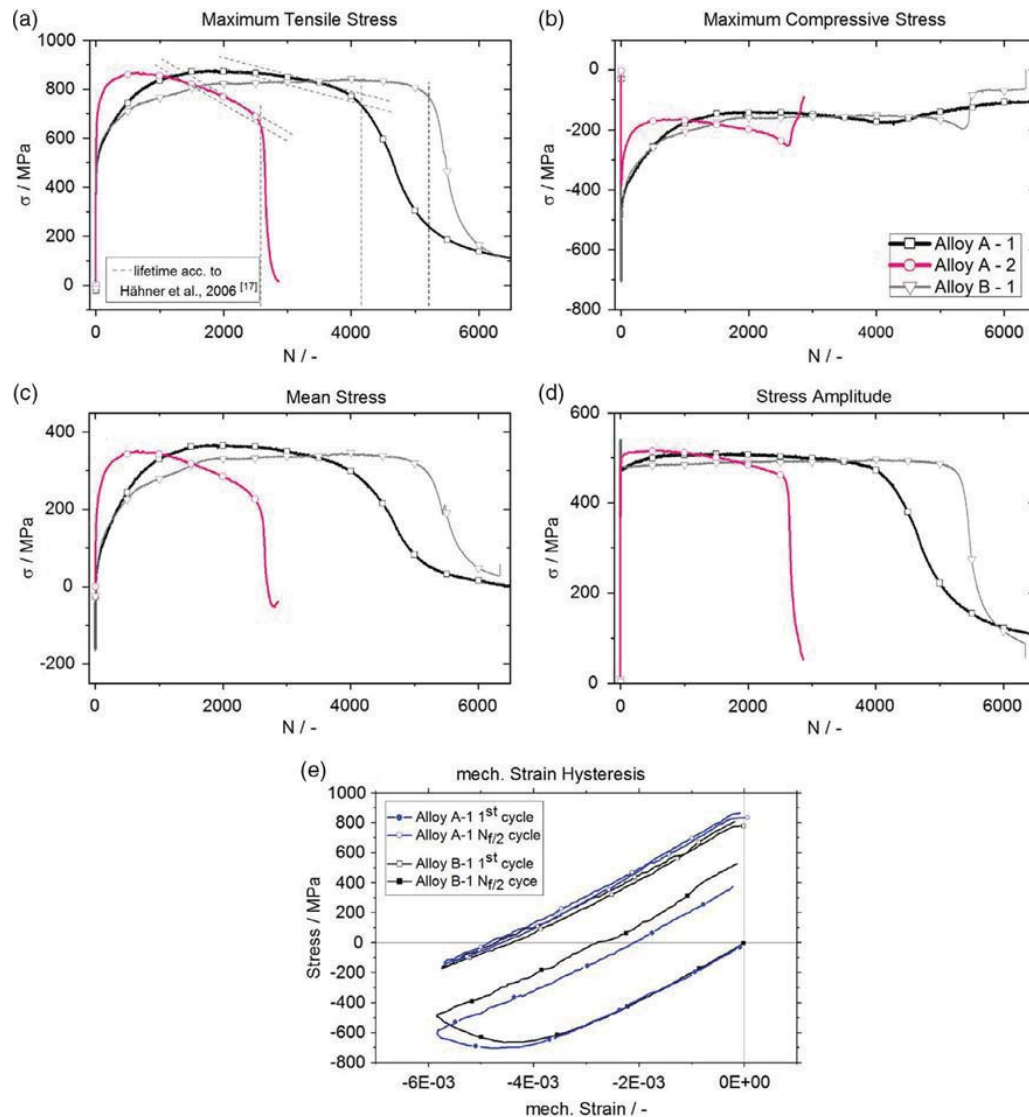


Figure 3. Development of stresses during OP-TMF testing. a) Maximum tensile stress, b) maximum compressive stress, c) mean stress, and d) stress amplitude of each cycle. e) Mechanical stress–strain hysteresis loop for the first and $N_{f/2}$ cycle of the TMF tests alloy A-1 and alloy B-1.

In Figure 3e, the mechanical stress–strain hysteresis for the first and $N_{f/2}$ -cycle of the TMF tests alloy A-1 and alloy B-1 are shown. Both alloys experience large plastic deformations within the first cycle. However, the plastic strain is clearly higher for alloy B-1, which according to Manson–Coffin’s law results in a lower fatigue lifetime.^[20] With increasing cycle number, the plastic strain amplitude decreases for both alloys. At $N_{f/2}$, hardly any plastic deformation is detectable.

3.2. Microstructural Investigations

In the final heat treatment condition, the microstructures of both materials consist of tempered martensite containing

micrometer-sized primary carbides.^[15,21] Alloys A and B reach a hardness of 617 ± 2 HV5 and 654 ± 4 HV5, respectively. After the TMF testing, the hardness of alloy A drops to 363 ± 4 HV5 and 356 ± 2 HV5 for alloy B. Due to the heating rate of ± 10 K s⁻¹ and 6762 cycles until fracture, alloy A was exposed to temperatures exceeding 500 °C for 51.1 h leading to a reduction of hardness by 41%. Alloy B in contrast endured only 2864 cycles and thus temperatures exceeding 500 °C for 21.8 h until fracture, resulting in a hardness drop by 46%. Although alloy A was longer exposed to the increased temperatures, the hardness drop is more pronounced for alloy B, indicating a higher tempering resistance for alloy A.

Siller^[5] reported continuous softening of hot-work tool steels if the surface temperatures exceeded 650 °C during thermal fatigue testing, which is slightly higher compared with the findings in this study. However, the testing device used by Siller used laser irradiation inducing a thermal gradient within the tested specimens, whereas the test setup used in this study uses a near constant temperature distribution in the sample volume. This deviation in temperature and stress distribution is therefore likely to be the main cause for these differing observations.

In **Figure 4**, micrographs of the fracture surfaces are shown. The numerous initiated fatigue cracks are visible as smooth areas along the circumference of the specimens. Because the fatigue testing was conducted in air atmosphere, the entire fracture surface of both alloys is covered by an oxide layer. The metallic bright area at the right of **Figure 4b** marks the position of the sample fracture.

As can be seen in the cross sections of TMF-tested samples in **Figure 5**, crack paths are covered by oxide layers as well. Adjacent

to large cracks, both alloys show numerous small cracks with a length of a few microns underneath a thick oxide layer. However, the crack density and therefore the amount of the surface area covered by the thick oxide layer are much greater for alloy B. These oxides have a duplex structure, consisting of a thin and compact outer and a thick, porous inside layer. Similar findings were made in the study by Le Roux et al.,^[10] where a duplex oxide scale on TMF-tested X38CrMoV5 consisting of an inside layer of Cr₂O₃ and an outer porous Fe₂O₃ layer was reported.

Etched cross sections of the fracture surface are shown in **Figure 6**. In **Figure 6a**, the martensitic microstructure of alloy A can be determined. In contrast, no martensitic microstructure is visible in the micrograph of alloy B in **Figure 6b**. Parts of the oxide layer covering the fracture surface are lost during sample preparation. The visible oxide has a reduced thickness compared with the surface oxide layer in close proximity to large fatigue cracks, but shows the same duplex structure. It can be seen that for both investigated alloys, neither fatigue cracks nor the fracture

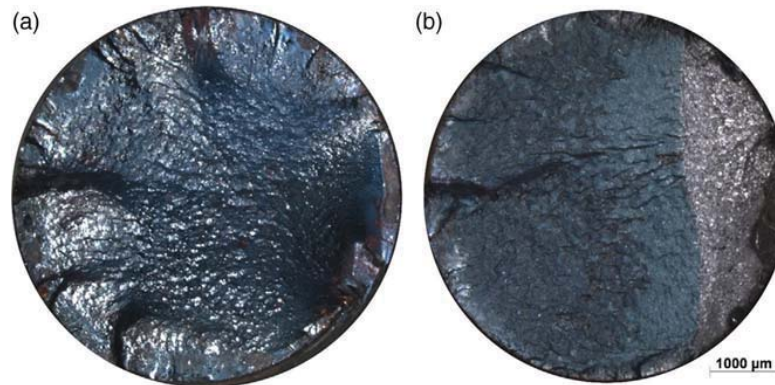


Figure 4. Stereo microscopic micrograph of the oxide covered fracture surface of a) TMF-tested alloy A and b) TMF-tested alloy B.

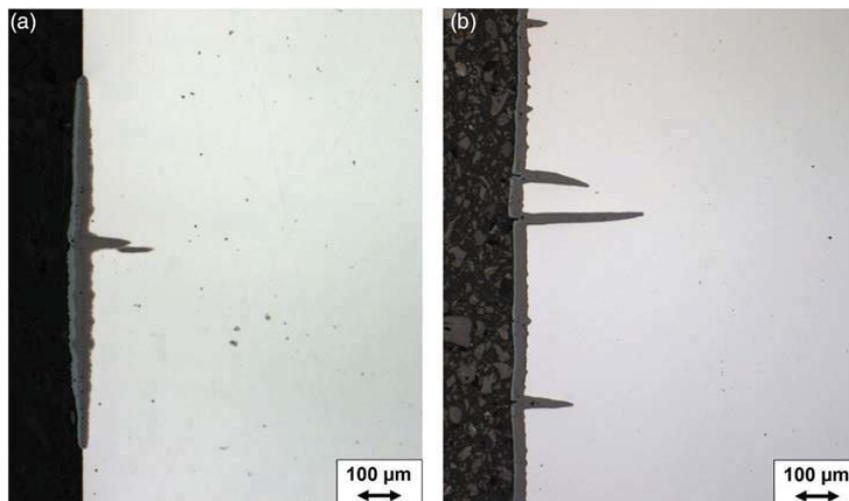


Figure 5. Cross sections of the specimen surface with large cracks and oxide layer of a) alloy A and b) alloy B. Adjacent to large cracks a thick oxide layer is formed, covering small surface cracks.

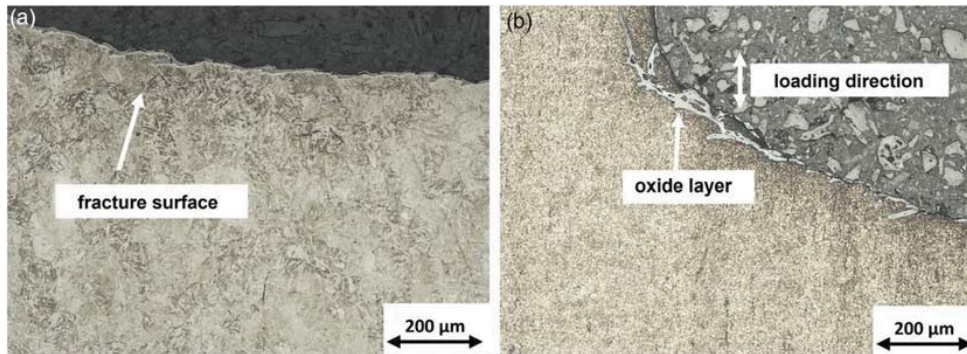


Figure 6. Cross sections of the fracture surface of a) alloy A, etched with W2 and b) alloy B, etched with 3% HNO₃. Due to the sample preparation, parts of the oxide layer are lost. In the case of alloy A, a martensitic microstructure is visible.

surface propagates along grain boundaries. However, the fatigue cracks propagate perpendicular to the loading direction.

As shown in **Figure 7**, numerous fatigue cracks have been initiated on the surface of the specimens. The number density of these surface cracks is greater for alloy B compared to alloy A. These cracks are, in contrast to conventional heat checks,^[3,4] oriented parallel to each other and perpendicular to the longitudinal axis of the specimens. The reason for this behavior is the test setup, where a temperature gradient is simulated by a mechanical constraint of the thermal expansion along the longitudinal axis of the specimen and thus plastic deformation is limited to this direction. A quantification of the crack density was not performed as an unknown number of surface cracks is covered by the thick oxide layer. Especially for alloy B, the high crack density and resulting oxidation leads to an almost complete coverage of the sample surface with thick oxide.

The micrograph of alloy A in **Figure 7a** shows that only in close proximity to large surface cracks a thick oxide layer has formed. These oxides have a cloudy shape and propagate perpendicular to the fatigue cracks in loading direction. Further investigations showed series of parallel-oriented cracks propagating perpendicular to the loading direction underneath these thick oxide layers, which is also visible in **Figure 5**. No evidence of material damage caused by circumferential stresses introduced

by thermal gradients could be detected in any of the investigated specimens. The specimen surface not covered by thick oxides appears orange for alloy A and rose for alloy B, indicating an oxide layer of a few hundred nanometers thickness.^[22] These findings are in contrast to the investigations presented in the study by Le Roux et al.,^[8] where immersion tests of hot-work tool steels into molten Al were conducted. In air atmosphere, a global oxidation was observed. Only a reduced oxygen partial pressure resulted in similar oxide structures adjacent to large surface cracks, as was also observed in this study.

3.3. High-Resolution Analysis by Atom Probe Tomography

The following results aim to give an impression on the impact of the TMF testing on the microstructure of the investigated steels. However, due to poor statistics, no attempt will be made to quantify the volume fraction, number density, or particle size of the secondary hardening precipitates.

3.3.1. Alloy A

Figure 8 shows the reconstruction of an atom probe measurement of alloy A aged at 585 °C. A high number density of evenly distributed, spherical particles enriched in Ni and Al is visible,

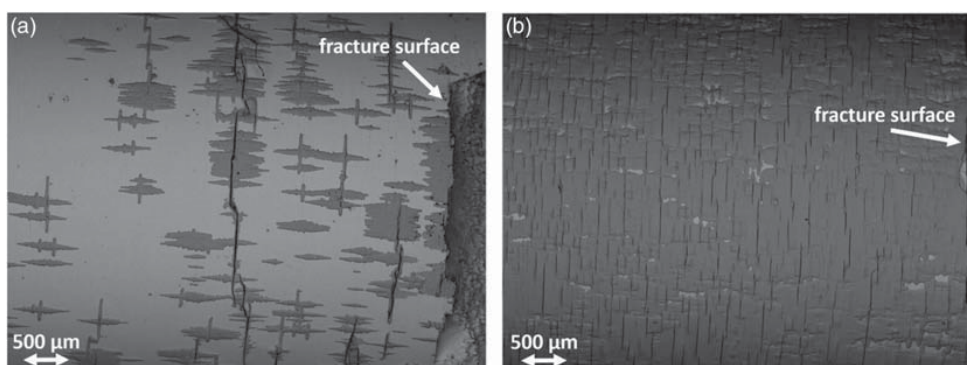


Figure 7. Back-scattered electron scanning electron microscope micrograph of the specimen surface of a) alloy A and b) alloy B after TMF testing. In proximity to large fatigue cracks, a thick oxide layer has formed.

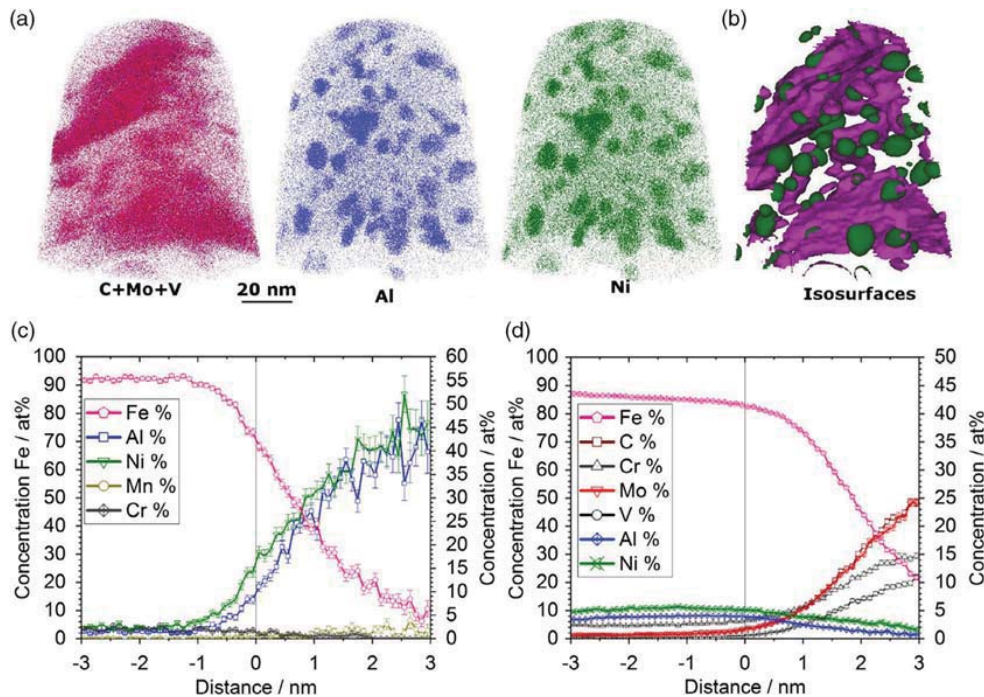


Figure 8. APT measurement of alloy A aged at 585 °C. a) From left to right: atom maps of (C, Mo, V), Al and Ni. b) Isoconcentration surfaces of 25 at% (Ni + Al) in green and 5 at% (Mo + V) in pink. c) Proximity histogram according to (Ni + Al) isosurfaces. d) Proximity histogram according to large (Mo + V) isosurface. Zero distance on the abscissa corresponds to the precipitate/matrix interface; positive values are inside the precipitate. For colored images, the reader is referred to the web version of this article.

which form the intermetallic NiAl phase in a size range of a few nm. As can be derived from the proximity histogram of such a particle shown in Figure 8c, only a small Fe content is present within the precipitates. Furthermore, they show an enrichment in Mn and depletion of Cr compared with the surrounding iron matrix. The distribution of carbide forming elements in Figure 8a such as C, Mo, and V seems more irregular compared with that of NiAl. Despite small, plate-like carbides situated in close proximity to NiAl particles, two almost parallel plate-like structures stretching through the entire diameter of the measured volume are visible. The smaller carbides close to the NiAl particles reach a lower carbon content compared with the large structures. Within the plate-like carbide structures, the carbon content varies from 20 to 30 at% C, resulting in the mean core value of 25 at%, as shown in Figure 8d. The carbides are depleted in Ni and Al. If considered that some amount of the carbon is lost due to multiple detector events,^[23] it can be assumed that these are M_2C or possibly $M_{23}C_6$. Prior microstructural investigations of this alloy showed no $M_{23}C_6$ carbides in this heat treatment condition,^[15] which is why it is assumed that these carbides represent an early or transition state of M_2C carbides.

The microstructure of alloy A after TMF testing is shown in Figure 9. It is clearly visible that both precipitate populations are significantly coarsened. The chemical composition of the NiAl particles has not changed compared with Figure 8 and still

contains about 10 at% Fe. However, the chemical composition of the detected carbides does differ significantly, which possess a carbon content of 40 and 25 at% of both V and Mo and are thus likely MC carbides.

3.3.2. Alloy B

Figure 10a shows the microstructure of alloy B annealed at 620 °C and Figure 10b in the TMF-tested condition. In the heat-treated condition, plate-like carbide structures as well as spherical carbides are visible, similar to alloy A. The carbide plates contain a core carbon content of ≈ 30 at% C and are considerably enriched in Mo. This could give rise to the assumption that the detected carbides are Mo_2C carbides. After the TMF testing (Figure 10b), a low particle number density of large carbides is present. However, these carbides contain an increased Fe content of up to 10 at%. Significant coarsening of the carbides due to the TMF testing is visible.

It is assumed that the improved tempering resistance and therefore the increased TMF lifetime of the dual hardening alloy is caused by the combination of secondary hardening carbides and intermetallic precipitates. Upon ageing, the intermetallic particles precipitate very fast and homogeneously distributed due to their coherency to the iron matrix,^[24] expanding the preferred precipitation sites for secondary hardening carbides from dislocations and grain boundaries to interfaces between the NiAl

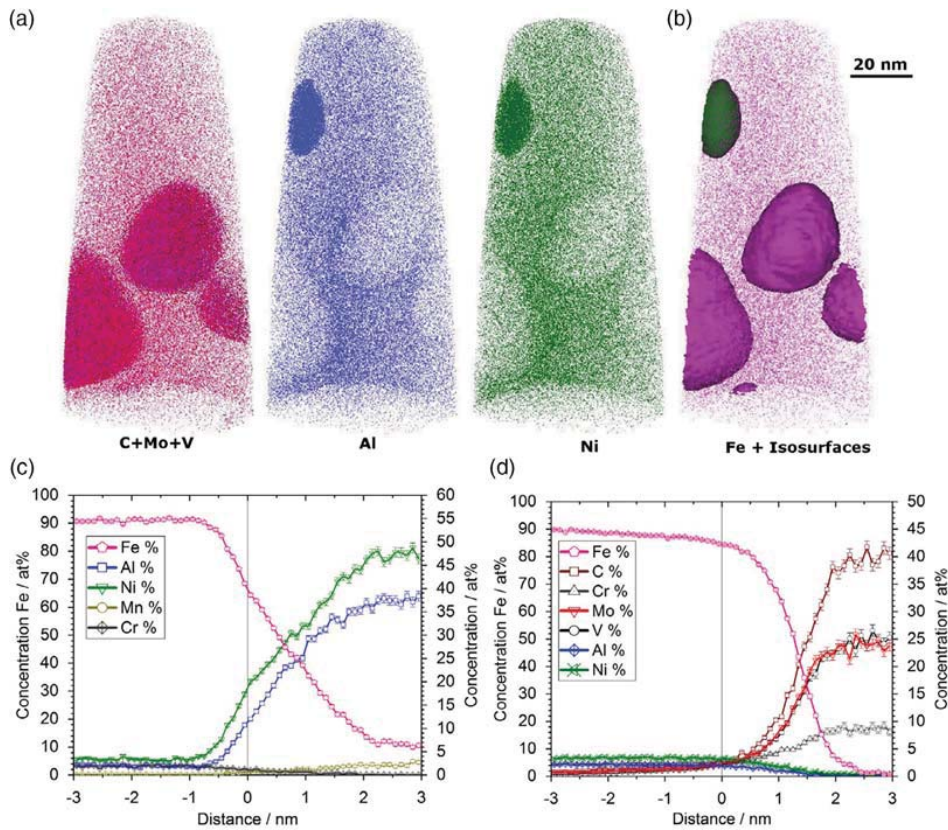


Figure 9. APT measurement of TMF-tested alloy A-1. a) From left to right: atom maps of (C, Mo, V) Al and Ni. b) Isoconcentration surfaces of 25 at% (Ni + Al) in green and 5 at% (Mo + V) in pink. c) Proximity histogram according to (Ni + Al) isosurfaces. d) Proximity histogram according to (Mo + V) isosurfaces. Zero distance on the abscissa corresponds to the precipitate/matrix interface; positive values are inside the precipitate.

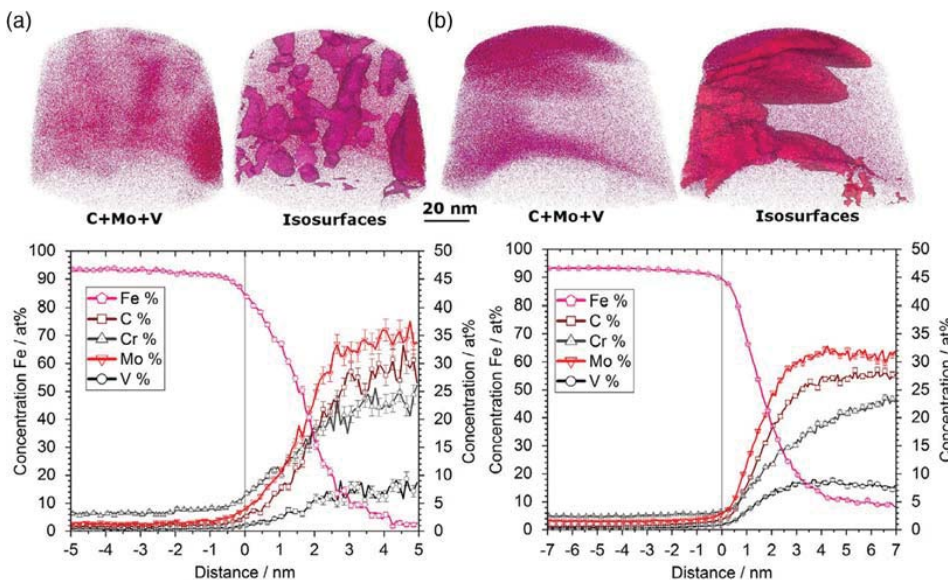


Figure 10. APT measurements of alloy B. a) Annealed at 620 °C. b) TMF-tested specimen alloy B-1. Left: Atom map of C, Mo, and V. Right: isoconcentration surfaces of 5 at% (Mo + V). Bottom: Proximity histograms according to isosurfaces, zero distance on the abscissa corresponds to the carbide/matrix interface; positive values are inside the carbides.

particles and the iron matrix.^[13] This leads to an increased amount of precipitation sites, thus a more homogeneous distribution and size refinement of the secondary hardening carbides, resulting in an increased tempering resistance. Furthermore, the atom probe data shows that in the dual hardening steel, after TMF testing, a higher particle number density is present due to two different populations of precipitates.

4. Conclusions

In this study, out-of-phase TMF tests, reproducing the complex cyclic loading conditions hot-work tool steels experience during application, were performed. The investigated materials include a 5% Cr hot-work tool steel and a dual hardening steel, containing intermetallic NiAl as well as carbide secondary hardening precipitates. The dual hardening alloy showed an increased resistance against softening during the TMF testing, resulting in a higher lifetime and lesser surface crack density compared with the chromium hot-work tool steel.

Following conclusions can be drawn: 1) The TMF testing leads to a shift of the mean stress into the tensile region through plastic deformation. A constant drop of the stress amplitude is visible during the TMF lifetime and is more pronounced for the chromium hot-work tool steel. 2) Numerous fatigue cracks are initiated around the circumference of the specimens. The surface of these cracks is covered by an oxide layer. 3) The dual hardening alloy shows higher tempering resistance and a higher resistance to TMF than the chromium hot-work tool steel. APT was able to reveal significant coarsening of the secondary hardening precipitates in both investigated alloys during the TMF testing.

Acknowledgements

The authors gratefully acknowledge funding from the Austrian BMVIT (846933) in the framework of the program "Production of the future" and the "BMVIT Professorship for Industry."

Conflict of Interest

The authors declare no conflict of interest.

Keywords

atom probe tomography, dual hardening steels, fatigue testing, heat checking, hot-work tool steel, secondary hardening, thermomechanical fatigue

Received: August 19, 2019

Revised: October 23, 2019

Published online:

- [1] G. A. Roberts, G. Krauss, R. Kennedy, *Tool Steels*, ASM International, Materials Park, OH **2010**.
 [2] D. A. Spera, D. F. Mowbray, *Thermal Fatigue of Materials and Components*, ASTM International, West Conshohocken, PA **1976**, pp. 19428–2959.

- [3] J. R. Davis, *Tool Materials*, ASM International, Materials Park, Ohio **1995**.
 [4] R. Bürgel, H. J. Maier, T. Niendorf, in *Handbuch Hochtemperatur-Werkstofftechnik* (Eds: H. J. Maier, T. Niendorf, R. Bürgel), Springer Fachmedien Wiesbaden, Wiesbaden **2015**, pp. 189–243.
 [5] I. Siller, *Temperaturwechselprüfung von Warmarbeitsstählen mittels gepulster Laserstrahlung*, Montanuniversität Leoben, Leoben **2003**.
 [6] Q. Zhou, X. Wu, N. Min, Y. Min, in *Tool 2012* (Ed: ASMET), ASMET - The Austrian Society for Metallurgy and Materials, Leoben **2012**, pp. 365–373.
 [7] a) R. Ebner, S. Marsoner, I. Siller, W. Ecker, *IJMMMP* **2008**, *3*, 182; b) D. Delagnes, F. Rézai-Aria, C. Levaillant, A. Grellier, in *Tool Steels in the Next Century: Proceedings of the 5th International Conference on Tooling* (Ed: F. Jeglitsch), University of Leoben, Leoben, Austria **1999**.
 [8] M. Salem, P. Lamesle, G. Dour, S. Le Roux, F. Rézai-Aria, in *Tool 2012* (Ed: ASMET), ASMET - The Austrian Society for Metallurgy and Materials, Leoben **2012**, pp. 357–364.
 [9] A. Persson, S. Hogmark, J. Bergström, *Int. J. Fatigue* **2004**, *26*, 1095.
 [10] S. Le Roux, F. Medjedoub, G. Dour, F. Rézai-Aria, *Micron* **2013**, *44*, 347.
 [11] D. Klobčar, J. Tušek, B. Taljat, *Mater. Sci. Eng. A* **2008**, *472*, 198.
 [12] a) J. Bergström, F. Rézai-Aria, in *Tooling Materials and their Applications from Research to Market* (Eds: M. Rosso, M. A. Grande, D. Ugues), Politecnico Di Torino, Torino, Italy **2006**, pp. 545–554; b) F. Rézai-Aria, A. Oudin, S. Jean, B. Miquel, P. Lamesle, in *Proceedings of 21th International Die Casting Congress and Exposition* (Ed: NADCA), North American Die Casting Association, Illinois **2001**; c) P. Huter, S. Oberfrank, F. Grün, B. Stauder, *Int. J. Fatigue* **2016**, *88*, 142.
 [13] F. Danoix, R. Danoix, J. Akre, A. Grellier, D. Delagnes, *J. Microscopy* **2011**, *244*, 305.
 [14] a) W. M. Garrison, M. S. Bhat, *MTA* **1988**, *19*, 1751; b) S. D. Erlach, F. Danoix, H. Leitner, P. Auger, I. Siller, H. Clemens, *Surf. Interface Anal.* **2007**, *39*, 213; c) H. Leitner, M. Bischof, H. Clemens, S. Erlach, B. Sonderegger, E. Kozeschnik, J. Svoboda, F. D. Fischer, *Adv. Eng. Mater.* **2006**, *8*, 1066.
 [15] M. Hofinger, M. Staudacher, M. Ognianov, C. Turk, H. Leitner, R. Schnitzer, *Micron* **2019**, *120*, 48.
 [16] M. Riedler, H. Leitner, B. Prillhofer, G. Winter, W. Eichlseder, *Meccanica* **2007**, *42*, 47.
 [17] P. Hähner, E. Affeldt, T. Beck, H. Klingelhöffer, M. Loveday, C. Rinaldi, *Thermo-Mechanical Fatigue – The Route to Standardisation*, Office for Official Publications of the European Communities, Luxembourg, **2006**, https://netzwerke.bam.de/Netzwerke/Content/EN/Downloads/jrc-tmf-validated-code-of-practice.pdf?__blob=publicationFile, (accessed: November 2018).
 [18] G. Petzow, *Mat.-wiss. u. Werkstofftech.* **1977**, *8*, 68.
 [19] a) *Atom Probe Tomography: Put Theory into Practice*, (Eds: W. Lefebvre-Ulrikson, F. Vurpillot, X. Sauvage, Academic Press, London **2016**); b) B. Gault, M. P. Moody, J. M. Cairney, S. P. Ringer), *Atom Probe Microscopy*, Springer, New York, NY **2012**.
 [20] a) S. S. Manson, *Exp. Mech.* **1965**, *5*, 193; b) L. F. Coffin, *Trans. ASME* **1954**, *76*, 931.
 [21] H. Wurmbauer, M. Panzenböck, H. Leitner, C. Scheu, H. Clemens, *Mat.-wiss. u. Werkstofftech.* **2010**, *41*, 18.
 [22] a) U. R. Evans, *Proc. Roy. Soc. Lond. A* **1925**, *228*; b) G. Tammann, *Z. Anorg. Allg. Chem.* **1920**, *111*, 78.
 [23] L. Yao, B. Gault, J. M. Cairney, S. P. Ringer, *Philos. Mag. Lett.* **2010**, *90*, 121.
 [24] a) F. Pettinari-Sturmel, B. Kedjar, J. Douin, C. Gatel, D. Delagnes, A. Coujou, *Mater. Sci. Eng. A* **2013**, *576*, 290; b) M. Hofinger, M. Ognianov, C. Turk, H. Leitner, R. Schnitzer, *HTM* **2019**, *74*, 293.

Paper IV

M. Hofinger, C. Turk, M. Ognianov, H. Leitner, R. Schnitzer

Precipitation reactions in a Cu-Ni-Al medium carbon alloyed dual hardening steel

Materials Characterization 160 (2020) 110126.

DOI: [10.1016/j.matchar.2020.110126](https://doi.org/10.1016/j.matchar.2020.110126)

Precipitation reactions in a Cu-Ni-Al medium carbon alloyed dual hardening steel

Matthias Hofinger¹, Christoph Turk², Miloslav Ognianov², Harald Leitner², Ronald Schnitzer¹

¹ Montanuniversität Leoben, Department of Materials Science, Franz-Josef-Straße 18, 8700 Leoben, Austria

² voestalpine Böhler Edelstahl GmbH & Co KG, Mariazellerstraße 25, 8605 Kapfenberg, Austria

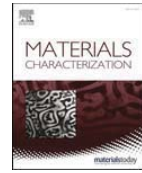
Abstract

Dual hardening steels achieve secondary hardening through the combined precipitation of intermetallic phases and carbides. The early stages of precipitation of a Cu-Ni-Al medium carbon alloyed dual hardening steel with a low alloying ratio of Cu/NiAl were investigated. Phase separation during continuous heating with 20 Kmin⁻¹ was identified to occur in the temperature range from 360°C to 620°C by differential scanning calorimetry. The precipitates were characterized utilizing atom probe tomography. Different cluster search algorithms were used in order to determine the sequence of phase separation and thus identify the individual precipitation reactions. It was shown that phase separation starts with the formation of Cu (Ni, Al, Mn) clusters. At an ageing temperature of 580°C, heterogeneous precipitation of VC-clusters at the interfaces between the Cu-precipitates and the iron matrix takes place. A phase separation of the Cu (Ni, Al, Mn) clusters into separate Cu and NiAl particles could not be observed up to an ageing temperature of 620°C. The sequence of precipitation is thus determined to be Cu-VC-NiAl.



Contents lists available at ScienceDirect

Materials Characterization

journal homepage: www.elsevier.com/locate/matchar

Review

Precipitation reactions in a Cu-Ni-Al medium carbon alloyed dual hardening steel

Matthias Hofinger^{a,*}, Christoph Turk^b, Miloslav Ognianov^b, Harald Leitner^b, Ronald Schnitzer^a^a Montanuniversität Leoben, Department of Materials Science, Franz-Josef-Straße 18, 8700 Leoben, Austria^b voestalpine Böhler Edelstahl GmbH & Co KG, Mariazellerstraße 25, 8605 Kapfenberg, Austria

ARTICLE INFO

Keywords:

Dual hardening steel
 Differential scanning calorimetry
 Atom probe tomography
 Radial distribution function
 Cluster analysis
 Solute clustering

ABSTRACT

Dual hardening steels achieve secondary hardening through the combined precipitation of intermetallic phases and carbides. The early stages of precipitation of a Cu-Ni-Al medium carbon alloyed dual hardening steel with a low alloying ratio of Cu/NiAl were investigated. Phase separation during continuous heating with 20 K min^{-1} was identified to occur in the temperature range from 360 °C to 620 °C by differential scanning calorimetry. The precipitates were characterized utilizing atom probe tomography. Different cluster search algorithms were used in order to determine the sequence of phase separation and thus identify the individual precipitation reactions. It was shown that phase separation starts with the formation of Cu (Ni, Al, Mn) clusters. At an ageing temperature of 580 °C , heterogeneous precipitation of VC-clusters at the interfaces between the Cu-precipitates and the iron matrix takes place. A phase separation of the Cu (Ni, Al, Mn) clusters into separate Cu and NiAl particles could not be observed up to an ageing temperature of 620 °C . The sequence of precipitation is thus determined to be Cu-VC-NiAl.

1. Introduction

Dual hardening steels were first investigated in 1988 [1] in order to produce high strength steels with increased toughness and a reduced carbon content. High strength was achieved by the combined precipitation of both intermetallic particles and carbides. The intermetallic phases used in these steels must comprise of non-carbon affine elements, to ensure no competition between the formation of intermetallic precipitates and carbides takes place. Alloying possibilities are therefore currently limited to Ni and Al, known to form NiAl-particles, or Cu.

Dual hardening steels show rapid hardening upon ageing. Precipitation reactions occur within the first minute of ageing at 610 °C [2,3]. The intermetallic NiAl precipitates are fully coherent to the ferrite iron matrix and therefore experience rapid precipitation kinetics, resulting in a homogeneous distribution of very fine particles [4–8]. The evolution of coherent B2 NiAl precipitates shows that for short ageing times, significant amounts of Fe are incorporated in the precipitates, which reach an equilibrium composition after ageing at 575 °C for 15 h [9–11].

In dual hardening steels, carbide formation is achieved with carbon contents between 0.6 and 1.7 at.% and additional alloying with V, Cr or Mo [12,13]. In NiAl free steels, secondary hardening carbide precipitation is limited to dislocations or grain boundaries. However, due

to the rapid formation of homogeneous distributed NiAl within the iron matrix, these intermetallic precipitates can act as heterogeneous precipitation sites for the carbides, leading to a homogeneous distribution of the latter [3,7,14]. The “assisted precipitation” of secondary hardening carbides caused by the intermetallic NiAl particles leads to a homogeneous carbide distribution [7], which is the main reason for the combination of high strength and toughness of dual hardening steels [15].

The precipitation of Cu from supersaturated ferrite is reported to start with the formation of a bcc CuFe cluster [16]. Upon further ageing, these particles undergo a transformation into a 9R martensitic structure, and reach their equilibrium fcc structure at a particle size beyond approximately 15 nm [16–20]. Through including high amounts of Fe during the early stages, the nucleation barrier can be reduced, leading to a rapid precipitation of CuFe particles. Due to their reduced thermodynamic stability, these precipitates dissolve after reaching their peak density, resulting in the formation of thermodynamic stable Cu-rich particles containing a negligible amount of Fe [16,21].

Assisted precipitation of secondary hardening carbides by additional alloying with Cu, similar to the effect described in [3,7,14,15] for NiAl, was successfully shown for high-strength gear steels in [22].

The early stages of Cu precipitation in 15–5PH maraging steel were

* Corresponding author.

E-mail address: matthias.hofinger@unileoben.ac.at (M. Hofinger).<https://doi.org/10.1016/j.matchar.2020.110126>

Received 5 June 2019; Received in revised form 7 January 2020; Accepted 8 January 2020

Available online 09 January 2020

1044-5803/ © 2020 Elsevier Inc. All rights reserved.

investigated by Primig et al. in [23]. Early CuFe clusters with a mean radius of 0.35 nm were detected between 200 °C and 400 °C when continuously aged with a heating rate of 15 K min⁻¹. An exothermal reaction around 500 °C was attributed to compositional changes of the precipitates, reaching their equilibrium Cu content [24].

When sufficient amounts for precipitation of both NiAl and Cu are present in an age hardening steel, the precipitation sequence depends on the ratio of Cu/Ni and Cu/Al [25]. If a high ratio of Cu/Ni and Cu/Al (0.5 [26]–2.8 [27]) is used, phase separation starts with the formation of Cu clusters. These Cu particles and their interface to the iron matrix enrich in solute elements such as Ni, Al and Mn [23,28–30]. After prolonged ageing times, heterogeneous precipitation of intermetallic NiAl precipitates takes place [25,26,29,31,32]. However, if low ratios of Cu/Ni and Cu/Al are present (0.3 [33]), phase separation is reported to start with the formation of NiAl clusters, which in turn enrich in Cu at the precipitate interfaces [34] or incorporate increased amounts of Cu, which eventually leads to heterogeneous precipitation of Cu at the NiAl interfaces [25]. No exact value for this ratio causing the shift in the precipitation sequence is reported in the literature.

Mn is reported to segregate at bcc-Cu ferrite interfaces along with Ni and reduces the elastic interactions with the iron matrix [28]. Hence, subsequent heterogeneous precipitation of particles enriched in Ni and Mn is promoted. Mn has also been found to be incorporated in B2-NiAl precipitates [35], where it is suspected to substitute either for Al [36] or Ni [3].

Due to its near atomic resolution, 3D-atom probe tomography (APT) provides a tool to elucidate the precipitation reactions in such complex alloys [37]. However, care must be taken when analyses sensitive to user-defined parameters are applied for the identification of clusters/precipitates. For these tasks, various analysis methods and algorithms exist. These can be based on, among others, the maximum separation between solute atoms [38–40], normalized frequency distribution analysis [41] or compositional analyses [42]. The radial distribution function (RDF) calculates the number of atoms in a spherical shell around a selected solute element in the entire measured volume. [43,44]. This analysis offers a high sensitivity, which despite the limitations in APT detector efficiency and spatial resolution is able to detect even the early stages of phase separation.

A recent interlaboratory study [45] addressed the issue of reproducibility and sensitivity of cluster identification and data evaluation of APT data on user defined parameters [38,45,46]. A thorough report of all relevant parameters and methods used for reconstruction, data mining and evaluation is strongly suggested in order to guarantee reproducibility and accurate data interpretation.

The precipitation sequence influences the available precipitation sites and thus distribution and homogeneity of the secondary hardening precipitates. Thus the aim of this study is to elucidate the precipitation reactions in a Cu-Ni-Al medium carbon alloyed dual hardening steel by identifying the temperature range of phase separation and high-resolution characterization of the precipitation reactions during continuous ageing. APT in combination with different tools for data mining is used to understand the evolution of chemical complex clusters during continuous ageing.

2. Experimental

The nominal chemical composition of the investigated dual hardening steel is given in Table 1. Heat treatments were performed in a Dilatometer Bähr DIL 805A. Samples were heated to an austenitization temperature of 900 °C with a heating rate of 5 K s⁻¹, held for 30 min and quenched with He to room temperature within 5 s. To determine the temperature ranges of phase separation, differential scanning calorimetry (DSC) measurements were performed on austenitized and quenched samples. Measurements were conducted with a constant heating rate of 20 K min⁻¹ in a Setaram Labsys and Ar with a gas flow of 50 ml/min during heating and 200 ml/min during cooling was used

Table 1

Nominal chemical composition of the investigated dual hardening steel and ratio of Cu/Ni and Cu/Al.

	C	V	Ni	Al	Cr	Cu	Si	Mn	Fe	Cu/Ni	Cu/Al
wt.%	0.13	0.06	3.50	1.15	0.35	1.20	0.20	1.95	Bal.	0.34	1.04
at.%	0.59	0.06	3.27	2.34	0.37	1.04	0.39	1.95	Bal.	0.32	0.44

as atmosphere. Specimens in the solution annealed condition were heated to 650 °C, held for 5 min and continuously cooled with 20 K min⁻¹ to room temperature. The same cycle was repeated after a thermal stabilization period and the signal measured in the second run was subsequently subtracted as baseline. Ageing was performed with a continuous heating rate of 20 K min⁻¹ to various temperatures ranging from 360 °C to 620 °C. Hardness was measured in HV10 and every given value equals the mean of six measurements. APT investigations were executed with an Imago LEAP 3000 X-HR in laser mode at a temperature of 40 K, 0.5% target evaporation rate and 0.2 nJ laser energy with a pulse frequency of 250 kHz. Processing of the acquired data was done with the software Ivas 3.6.14.

For every heat treatment condition, roughly 14 million ions were separated from the measured volumes for further cluster search investigations, taking care that no inhomogeneous microstructural features such as prior austenite grain boundaries or martensite lath boundaries were situated within the investigated volumes. This was done in order to ensure that no heterogeneous precipitation sites influenced the analysis. The mean atomic density of the measurements was 37 ± 2 hits/nm³.

During ranging of the APT data, peak overlaps of the Al₂₇¹⁺ and Fe₅₄²⁺ at 27 Da as well as of the Fe₅₈²⁺ and the Ni₅₈²⁺ ions occurred. A decomposition of these peaks based on natural isotope abundance [47] lead to a mean percent of range of 10.5 ± 3.0% Al₂₇¹⁺ and 88.3 ± 0.4% Ni₅₈²⁺ (mean and standard deviation calculated from the measurements investigated in this study). The peak at 27 Da was therefore ranged as Fe and at 29 Da ranged as Ni.

The RDFs were calculated with a step width of 0.05 nm. Only results for distances greater than 0.2 nm are presented, as results for smaller distances may be influenced by ion trajectory effects [48,49]. In the case of detected molecules, in particular C₂ and C₃, the RDF interpreted these as 2 and 3 atoms of that species at the same position, thus having a strong impact on the sensitivity of the RDF on the interpretation of C.

To evaluate the results obtained with RDF analysis, efforts were made in order to visualize and confirm these findings via cluster analysis based on the maximum separation algorithm [39] and the iso-surface method. The parameters for cluster analysis were determined as suggested in [38].

Phase fractions were determined by X-ray diffraction (XRD) measurements with a Bruker-AXS D8 Advance DaVinci with Cu K_α radiation with 40 mA and 40 kV. A 2θ angular range from 20 to 120° was measured with a step size of 0.01°. Phase fractions were calculated with the software TOPAS V.6.0 from Bruker AXS based on a refined Rietveld analysis [50]. The calibration of the XRD instrument was performed with a LaB₆ standard. Investigated heat treatment conditions included mechanically ground and polished samples of the quenched state and samples aged to 360 °C. In neither condition, a detectable austenite content was present.

3. Results

3.1. Differential scanning calorimetry and hardness

In Fig. 1, the difference in the heat flow between run and rerun in the DSC is shown. The following temperature values represent the mean and standard deviation of three individual measurements. A first exothermal reaction is seen in the temperature range from 223 ± 25 °C to

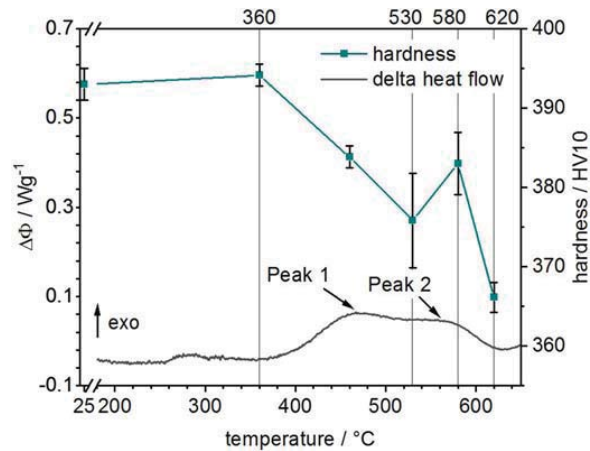


Fig. 1. Difference in heat flow $\Delta\Phi$ between run and rerun with a constant heating rate of 20 K min^{-1} and hardness of samples heat treated in a dilatometer to the respective temperatures.

$367 \pm 18 \text{ }^\circ\text{C}$. In the temperature range from $367 \text{ }^\circ\text{C}$ to $630 \text{ }^\circ\text{C}$, at least two individual exothermal peaks can be seen. The first, indicated in the graph with Peak 1, reaches its maximum at $470 \pm 5 \text{ }^\circ\text{C}$ and the second, indicated with Peak 2, at $552 \pm 5 \text{ }^\circ\text{C}$.

After quenching, the material reaches a hardness of $393 \pm 2 \text{ HV10}$. When continuously aged to $360 \text{ }^\circ\text{C}$, the material achieves a hardness of $394 \pm 1 \text{ HV10}$. Up to $530 \text{ }^\circ\text{C}$, the hardness continuously drops, after which a secondary hardening increase to $383 \pm 4 \text{ HV10}$ is reached at $580 \text{ }^\circ\text{C}$. When aged to $620 \text{ }^\circ\text{C}$, the hardness drops again to $366 \pm 2 \text{ HV10}$.

3.2. Atom probe tomography

To be able to link the exothermal reactions to individual precipitation reactions, APT measurements of samples continuously aged to $360 \text{ }^\circ\text{C}$, $530 \text{ }^\circ\text{C}$, $580 \text{ }^\circ\text{C}$ and $620 \text{ }^\circ\text{C}$ were performed. The mean chemical composition of all measurements is given in Table 2. The Pearson coefficient μ [41] was found to be inadequate to distinguish between the segregation behavior of Ni, Al and Cu. Especially in the early stages, this method showed the same amount of non-random distribution behavior for all the alloying elements.

RDFs centered around Al, Ni, Cu and C were calculated in every heat treatment condition. The evolution of the Al- and Ni-centered RDFs for the different maximum ageing temperatures is depicted in Fig. 2. The RDFs of C and V are not included as no deviation from random distribution was visible for any given annealing temperature. When aged to $360 \text{ }^\circ\text{C}$, the comparison to a random distribution, i.e. a normalized concentration equal to one, shows no elemental segregation of any solute elements towards Al or Ni. If the material is continuously aged to $530 \text{ }^\circ\text{C}$, which slightly surpasses the maximum of the first exothermal reaction in Fig. 1, first signs of cluster formation become visible. The

highest intensity at this temperature is reached for Al-Cu and Ni-Cu. Additionally, Al and Ni segregate into these clusters, along with Mn. At an ageing temperature of $580 \text{ }^\circ\text{C}$, a significant increase of solute elements and drop of Al-Fe and Ni-Fe can be seen. The highest values are again reached for Al-Cu and Ni-Cu. The enrichments reach to approximately 3 nm for all elements. In the case of Ni-Al, a local depletion of Al can be seen at distances greater than 2.5 nm .

When aged to $620 \text{ }^\circ\text{C}$, the composition of the clusters starts to change significantly. Except for Al-Cu and Ni-Cu, the amount of segregation decreases compared to an annealing temperature of $580 \text{ }^\circ\text{C}$. Due to a lower maximum and a shallower slope of the RDF at $620 \text{ }^\circ\text{C}$, it intersects with the RDF at $580 \text{ }^\circ\text{C}$ between 1.5 nm and 2.8 nm . It is interesting to note that the Al-Fe and Ni-Fe RDFs do not change significantly from $580 \text{ }^\circ\text{C}$ to $620 \text{ }^\circ\text{C}$.

The evolution of Cu-centered RDFs is shown in Fig. 3 and deviates significantly from those of Al and Ni. At an annealing temperature of $360 \text{ }^\circ\text{C}$, Cu-Cu already shows slight increases to 1.1 times normalized composition. When aged to $530 \text{ }^\circ\text{C}$, the Cu-centered RDFs show similar trends as Ni- and Al-centered, with Cu-Cu reaching the highest value. At $580 \text{ }^\circ\text{C}$, the RDFs show further cluster growth and enrichment of all solute elements. At distances from 1 to 3 nm and $1\text{--}4 \text{ nm}$ segregation of both C and V can be seen, respectively. These local enrichments are not visible at lower annealing temperatures or in the Al- and Ni-centered RDFs.

At a temperature of $620 \text{ }^\circ\text{C}$, Cu shows very strong signs of segregation. The segregations of Cu, Ni, Al and Mn clearly overlap and range to roughly $4.5\text{--}5 \text{ nm}$, experiencing an almost constant concentration up to 0.5 nm , followed by a continuous decrease. The local enrichments of C and V mentioned above are still visible and increase in both intensity and size. The high amount of scattering of C and V towards small distances is attributed to the small alloying content of these alloying elements and thus low number of atoms contributing to the RDFs at small distances. The Cu-Fe RDFs show continuous intensifying repulsion with increasing annealing temperature. These APT results confirm the formation of clusters as presumably visible in the DSC plot shown above in Fig. 1.

Carbon shows clear signs of segregation in all the conditions investigated, as is visible in Fig. 4. It must be noted that the measured C content, shown in Table 2, experiences the highest variations throughout the measured volumes. A possible explanation for these variations is the presence of large microstructural inhomogeneities, such as μm sized secondary carbides or retained austenite films, which have previously been detected, even in the quenched state [51]. Furthermore, the RDF has a decreased sensitivity for the interpretation of C clustering due to the detection of C_2 and C_3 molecules. Nevertheless, the same trends are true for all investigated samples. Carbon evidently segregates during quenching, not only to prior austenite grain or martensite lath boundaries, but also forms clusters within the iron matrix. These carbon clusters lack increased concentrations of carbide forming elements, such as V. Only when heated to $580\text{--}620 \text{ }^\circ\text{C}$, signs of V segregation towards C atoms and therefore the formation of VC carbides becomes evident.

To gain further information regarding precipitation sites and possible co-precipitation of Cu, NiAl and VC, as well as to obtain visual

Table 2

Chemical compositions measured by APT. The mean value and standard deviation were calculated from all successful measurements conducted in this study. The Cu cluster and 10 at.% (Ni + Al) Isosurfaces (which will be described in more detail later), were calculated in a sample continuously aged to $620 \text{ }^\circ\text{C}$.

at.%	C	V	Ni	Al	Cr	Cu	Si	Mn	Fe	Cu/Ni	Cu/Al
Mean of all measurements	0.18	0.07	3.05	2.62	0.34	0.79	0.56	1.62	Bal.	0.26	0.30
	± 0.16	± 0.00	± 0.17	± 0.10	± 0.004	± 0.06	± 0.01	± 0.02			
Cu cluster	0.07	0.06	8.38	7.87	0.25	14.88	0.48	3.09	64.79		
Matrix	0.07	0.06	2.80	2.55	0.33	0.55	0.59	1.57	91.39		
NiAl isosurface	0.11	0.10	9.68	8.33	0.27	10.23	0.50	3.14	67.62		
Matrix	0.05	0.06	2.77	2.54	0.33	0.61	0.59	1.57	91.45		

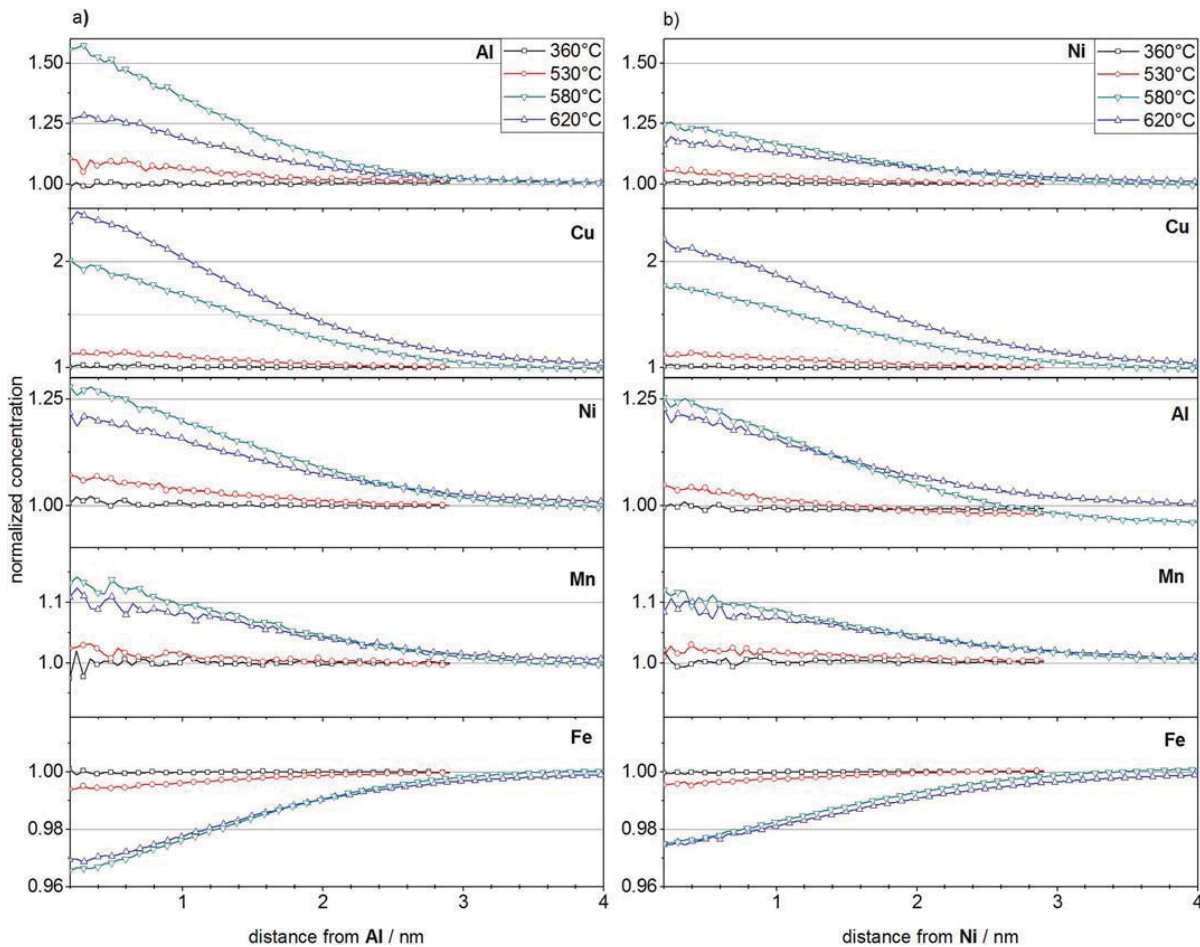


Fig. 2. Radial distribution functions centered around a) Al and b) Ni for continuous heating with 20 K min^{-1} to 360°C , 530°C , 580°C and 620°C . The RDFs of C and V are not included as no deviation from random distribution was visible for any given annealing temperature. Note different scaling of the ordinates.

confirmation of solute segregations, further cluster analyses were performed. For Cu, reasonable parameters for further cluster analysis could be distinguished in samples aged to 620°C , which are depicted in Fig. 5. The cluster count distribution shown in Fig. 5 a) has a local minimum of d_{max} around 0.6 nm . At this maximum separation distance, small variations do not greatly influence the number of detected clusters, and no clusters are artificially combined. Hence, this d_{max} is chosen for further analysis. Fig. 5 b) shows the distribution of Cu clusters as a function of the number of atoms within a cluster with a d_{max} of 0.6 nm . For further analysis, a N_{min} of 12 atoms was chosen.

Cluster analysis was performed with a d_{max} of 0.60 nm , order of ions of 3, minimum number of ions within a cluster of 12, an envelope of 0.60 nm and an erosion distance of 0.30 nm . The entire analyzed volume is shown in Fig. 6 a) and the identified Cu clusters in Fig. 6 b). The chemical composition of the Cu clusters and the remaining matrix is summarized in Table 2. These findings visually confirm the formation of Cu clusters enriched in Ni, Al and Mn as detected by the RDF analysis. Unfortunately, cluster count and size distributions for both Ni and Al failed to generate reasonable results (i.e., significant deviations from random distributions), independent of the heat treatment condition investigated.

To determine possible heterogeneous NiAl precipitation,

isoconcentration surfaces were calculated for (Ni + Al). A concentration below 10 at.% lead to a very rapid increase of the particle number density. From ten upwards a linear decrease was observed. The optical observation revealed that particles lost after increasing beyond 10 at.% often corresponded to sites also enriched in Cu and thus a $C_{(\text{Ni}+\text{Al})}^{\text{threshold}}$ of 10 at.% was chosen for further analysis. The 10 at.% (Ni + Al) isosurfaces are shown in Fig. 6 c) and were separately ranged and analyzed, exhibiting an Al and Ni concentration of 8.3 at.% and 9.7 at.% within the isosurface volume, respectively. The chemical composition of the isosurfaces and the remaining matrix are shown in detail in Table 2. The Fe content within the NiAl isosurfaces fits quite well to that measured in the Cu clusters. Although NiAl particles were successfully identified, the high Cu content is indicative that the Cu, Ni and Al enrichments are still present as one particle and phase separation or heterogeneous precipitation of NiAl adjacent to Cu has not started yet. From visual observations, it is clear that the NiAl particles derived with the isosurface method and the Cu clusters obtained by the cluster analysis overlap. However, while some Cu clusters lack significant amounts of Ni and Al, the analysis shows enrichment of Cu within all of the NiAl precipitates.

Fig. 6 d) shows a detailed view of a spherical Cu particle, which is also marked in Fig. 6 b). The Cu, Al and Ni atoms are depicted as spheres (not so scale), and the Fe atoms as points for improved

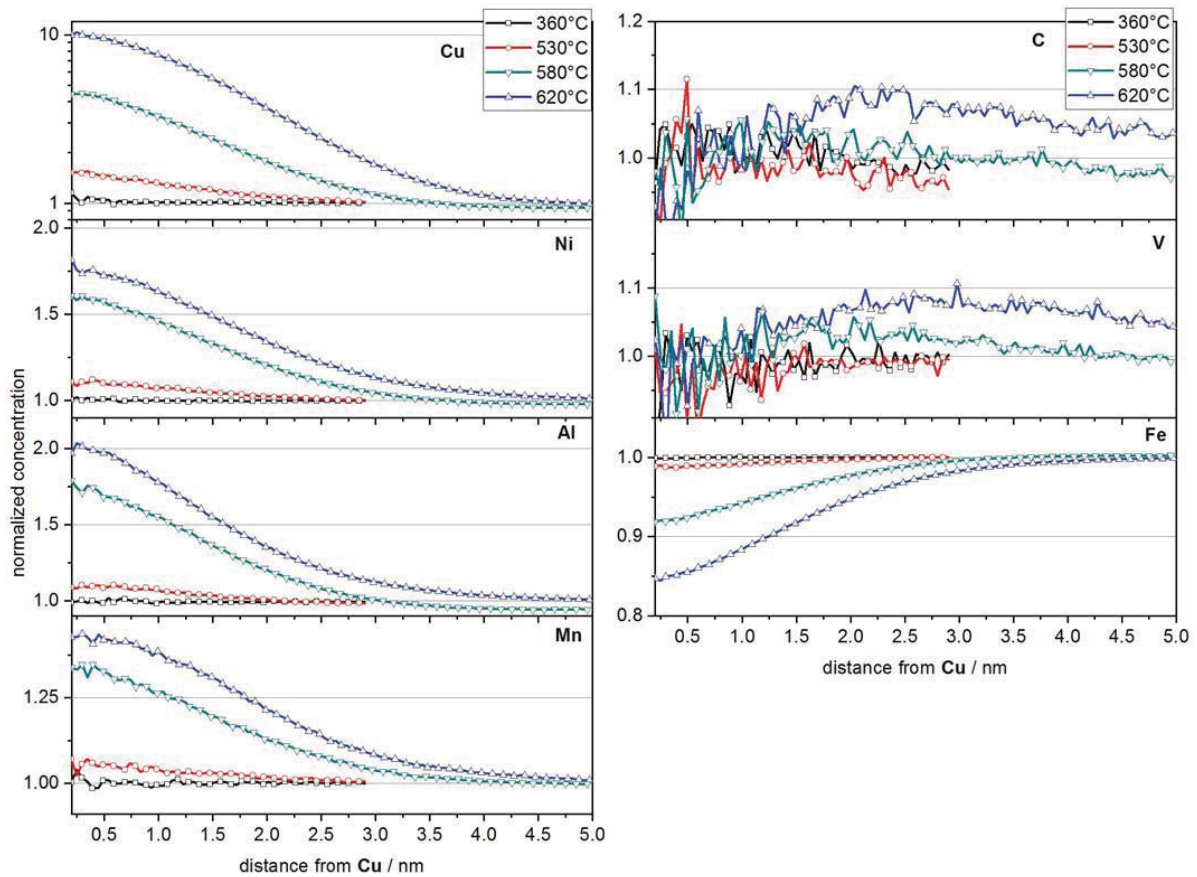


Fig. 3. Radial distribution functions centered around Cu for continuous heating with 20 K min^{-1} to $360 \text{ }^\circ\text{C}$, $530 \text{ }^\circ\text{C}$, $580 \text{ }^\circ\text{C}$ and $620 \text{ }^\circ\text{C}$. Note different ordinate scaling. The Cu-Cu ordinate is scaled logarithmically.

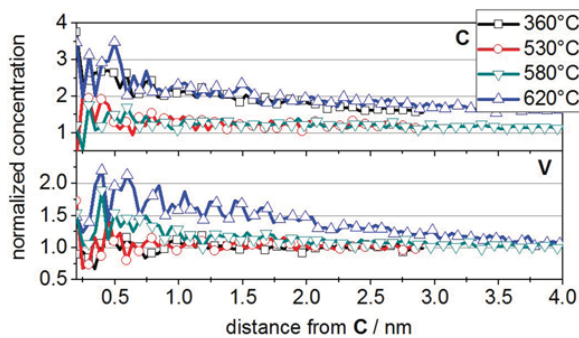


Fig. 4. C-centered radial distribution functions for continuous heating with 20 K min^{-1} to $360 \text{ }^\circ\text{C}$, $530 \text{ }^\circ\text{C}$, $580 \text{ }^\circ\text{C}$ and $620 \text{ }^\circ\text{C}$. Note different ordinate scaling.

visibility. It can be seen that the Cu atoms exhibit a higher amount of clustering in the center of the particle. The enrichment of Ni and Al is constant throughout the entire particle, however showing a larger spatial expansion compared to Cu. This suggests the absence of a core-shell structure or heterogeneous precipitation of NiAl particles, but rather a segregation of Ni and Al towards the Cu clusters, as well as incorporation inside these clusters.

4. Discussion

In this study, we aim to decode the sequence of precipitation in a Cu-Ni-Al alloyed medium carbon dual hardening steel during continuous ageing. The precipitation reactions are discussed with respect to the DSC and hardness curves shown in Fig. 1. From the hardness measurements it is evident that annealing of the dual hardening steel with a constant heating rate of 20 K min^{-1} lead to a maximum hardness of $394 \pm 1 \text{ HV}_{10}$ at $360 \text{ }^\circ\text{C}$. A secondary hardening reaction is visible, however, the achieved hardness of $383 \pm 4 \text{ HV}_{10}$ is slightly lower than in the quenched state, as can be seen in Fig. 1. When solution annealed with the same parameters and isothermally aged at $500 \text{ }^\circ\text{C}$, the investigated dual hardening alloy reaches significantly higher hardness levels. The maximum secondary hardness of 440 HV is obtained after ageing for 8 h.

In contrast to these findings, a dual hardening steel containing an increased amount of C and lacking any Cu investigated by Erlach et al. [3] was found to show a significant hardness increase when isothermally aged for only 60 s at $610 \text{ }^\circ\text{C}$. However, strengthening precipitates could not be detected in this state due to their size being too small to be measured by TEM.

Beside precipitation reactions, other phenomena possibly contributing to the DSC signal shall be addressed first. Influencing factors could be the recovery of dislocations, transformation of retained austenite and carbon redistribution. The occurrence of recovery can be discarded due to the small hardness increase at low annealing

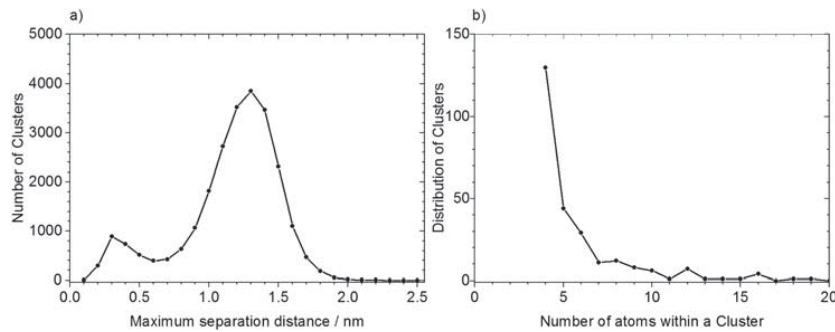


Fig. 5. Cluster analysis of Cu solute atoms of a sample continuously aged to 620 °C. a) Cluster count distribution (step width of 0.1 nm, order of ions = 3 and $N_{\min} = 3$). b) Cluster size distribution (calculated with $d_{\max} = 0.60$ nm and order of ions = 3).

temperatures. The rapid precipitation kinetics (of NiAl) have furthermore been reported to limit recovery during ageing [15]. The APT results obtained in this study showed site dependent inhomogeneous carbon distribution even in the quenched state. The measured microstructural features included dislocations, martensite lath boundaries and retained austenite films, as well as carbon clusters within the iron matrix. However, due to the lack of significant local C enrichments and especially segregation of carbide forming elements (starting only at annealing temperatures of above 550 °C), the contribution of carbon redistribution is assumed to be an ongoing process which already starts during quenching, and therefore no clear signal can be attributed to this phenomenon.

However, it must be noted that the measured C content shows the highest variations throughout the measured volumes, as can be seen in Table 2. Carbon also shows the highest discrepancy with the nominal composition in Table 1. This is attributed to the likely existence of μ m sized secondary carbides or retained austenite films, both enriched in carbon, which have previously been determined in the quenched state [51]. By random sample preparation out of the bulk volume, no information concerning the proximity of such microstructural features and therefore local carbon contents is possible.

In the DSC curve in Fig. 1, an exothermal reaction can be assumed between 250 °C and 360 °C. Considering that the material was quenched from austenitization temperature and no annealing was performed

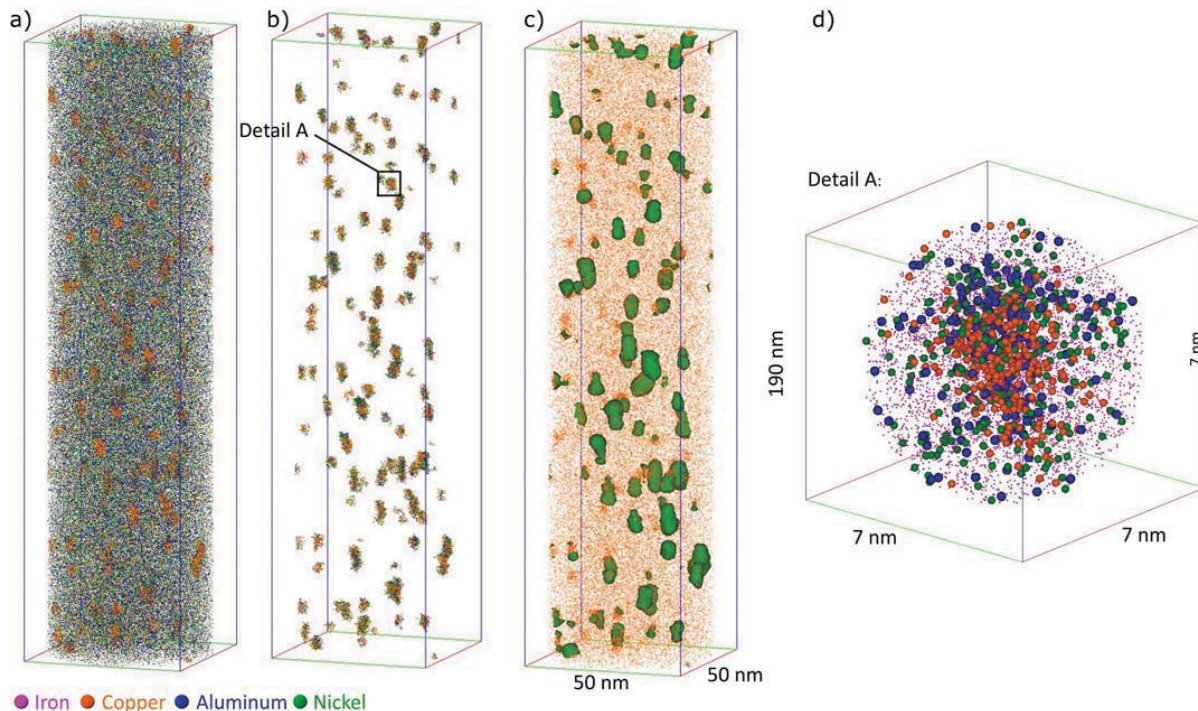


Fig. 6. APT reconstruction of a dual hardening steel continuously aged with 20 K min^{-1} to 620 °C. The presented cylindrical volume contains approximately 14 million atoms. a) Cu (orange), Ni (green) and Al (blue) atoms of the entire analyzed volume. b) Cu clusters distinguished by maximum separation method, with a d_{\max} of 0.60 nm, order of ions of 3, minimum number of ions within a cluster of 12, an envelope of 0.60 nm and an erosion distance of 0.30 nm. Only Ni, Al and Cu atoms are shown. c) Cu atoms and 10 at.% (Ni + Al) isosurfaces. d) Precipitate marked as “Detail A” in 6 b). The Cu, Ni and Al atoms are shown as spheres (not to scale), whereas the Fe atoms are shown as points for improved clarity. (For interpretation of the references to colour in this figure legend, the reader is referred to the web version of this article.)

prior to the DSC measurements, this signal could possibly be attributed to the decomposition of retained austenite. This is further indicated by the hardness evolution, which essentially stays the same after quenching and annealing to 360 °C. The atom probe measurements revealed no clustering of solute elements except carbon and possibly Cu at this annealing state. Cu has been suspected to start precipitation in this temperature range by other researchers but causes no increase in hardness at this point [23,52]. The formation of strengthening precipitates can therefore be ruled out to be responsible for the hardness level. If the martensitic matrix loses strength, as it is expected when annealed, a factor contributing to the hardness of the material could be the transformation of retained austenite. However, the XRD measurements did not detect any austenite in the quenched condition, which is why the austenite phase fraction is below the resolution limit of 2 vol. %. A significant contribution of the transformation to the heat flow during the DSC measurement is therefore unlikely. Another reaction causing the exothermal heat flow could be the formation of intermediate carbides. However, no clear sign of these could be detected in the APT measurements. It remains unclear whether the formation of Cu clusters containing only a few Cu atoms or the transformation of the low amount of retained austenite is responsible for the DSC signal.

The first explicit exothermal reaction is measured around 470 °C and is accompanied by a hardness drop. The APT results evidence cluster formation, as is visible in Figs. 2–3. The hardness drop is therefore assumed to be caused by the loss of matrix super saturation of alloying elements due to the formation of clusters. If this is the case, these clusters must either be too small for being a significant obstacle for dislocations, or the reduction in hardness due to loss of matrix super saturation or recovery of dislocations are the major factors contribution to the lowering of the overall hardness. Al, Ni, Cu and Mn all show positive segregation, with Cu-Cu exhibiting the most significant increase. No preferential Ni-Al or Al-Ni segregation can be detected. Owing to the fact that the highest increase of all solute elements is measured centered around the Cu atoms, it is assumed that formation of only one cluster species has taken place. The RDFs show a constant decreasing amount of segregation with increasing distance; the formation of a core-shell structure [28] can therefore be discarded at this stage. The early clusters contain high amounts of Fe (Table 2), which is in good agreement with literature [9,16,21].

In this condition, no deviation from random distribution can be detected for the carbide forming elements (other than carbon), see Fig. 4. The precipitation of alloying carbides has not yet taken place. This exothermal reaction is thus most likely caused by the formation of Cu (Ni, Al, Mn) clusters. However, it must be stated that Ni and Al are present in higher alloying contents and remain in higher concentrations in the matrix in this condition, see Table 2. This leads to a decreased sensibility of the RDF method for these elements compared to Cu.

The second exothermal maximum is reached at a temperature of 550 °C and results in an increase in hardness, indicating the formation of secondary hardening precipitates. Further ageing to 620 °C results in a hardness drop. The APT results of samples aged to 580 °C, which is still within the temperature range of the second exothermal reaction, indeed show further cluster growth and enrichment of all solute elements. In the following, the RDFs obtained at 580 °C and 620 °C will be compared. The amount of segregation in the Al- and Ni-centered RDFs in Fig. 2 decreases from 580 °C to 620 °C for all solute elements except Cu, which shows an increase. The course of the iron concentration stays the same. In contrast, the solute contents for all elements increase for the Cu-centered RDFs in Fig. 3, whilst the Cu-Fe RDF decreases significantly. This leads to the assumption that from 580 °C to 620 °C, the already built Cu (Ni, Al, Mn) clusters only further increase in Cu, while the content of Al and Ni atoms within these clusters stays the same. As a consequence, the segregation towards the Cu clusters increases for all solute elements as more Cu atoms are included within these clusters. As

the amount of Al and Ni atoms inside the clusters stays the same, no further repulsion of Fe occurs (Al-Fe and Ni-Fe RDFs in Fig. 2). The decrease of other solute elements and exclusive increase of Cu is therefore caused by the increased Cu concentration within the clusters. These results indicate that between 580 °C and 620 °C, Al and Ni segregation comes to an end. A possible explanation could be the transgression of the solvus temperature of the early stage NiAl(Cu) clusters. However, various studies on steels precipitation hardened by NiAl particles report stable precipitates at annealing temperatures of 600 °C [53], 620 °C [5] and even up to 650 °C [54].

At 620 °C, Cu clustering eventually becomes obvious, with the Cu-Cu RDF reaching a value of 10 times the matrix concentration. Literature connects the reaction at roughly 500 °C to compositional changes of Cu precipitates [23,24]. The mentioned core-shell structure [28,29] cannot be detected in this state, as is evident in Fig. 6 d).

The RDFs at 620 °C centered around Al and Ni indicate a continuous decrease with increasing distance, Fig. 2. In contrast, the Cu centered RDFs shown in Fig. 3 display a region of almost constant solute concentrations at small distances, followed by a shift at around 0.5 nm where a linear descent to matrix concentration at roughly 4.5 nm begins. It is assumed that the high relative Cu concentration and distance of almost constant solute concentrations marks the formation of Cu precipitates, which are also visible in Fig. 6. The high and almost constant Ni, Al and Mn concentrations are indicative of an enrichment of these solute elements within the Cu clusters. Furthermore, local enrichments of C and V at distances from 1 to 4 nm can be seen in the Cu-centered RDFs. The enrichment of V at C atoms is also visible in the C-centered RDFs in Fig. 4. We therefore conclude that the Ni, Al and Mn enrichments are still incorporated within the Cu precipitates. Furthermore, it is assumed that the Cu precipitates have reached a size or crystal structure sufficient to induce misfit strain in the surrounding iron matrix, thus creating sites for heterogeneous VC precipitation. Assisted precipitation of carbides has also been observed for NiAl in [3,7,14,15] and for Cu in [22].

The RDF analysis of APT data clearly demonstrates the precipitation sequence to be Cu (Ni, Al, Mn) – VC – NiAl. However, RDF analysis is not suited for high solute matrix contents, which is partially true for Ni and Al. This is why further cluster analysis based on composition was performed for Ni and Al. The separate Cu cluster and NiAl isosurface analyses indeed reveal that the local enrichments overlap, see Fig. 6. Hence no heterogeneous NiAl precipitation at the interfaces between the Cu particles and the iron matrix has taken place yet.

Table 3 gives an overview of the precipitation sequence reported in Cu-Ni-Al alloyed steels as well as the ratio of Cu/Ni and Cu/Al. Most studies report the precipitation sequence as Cu-NiAl. However, this study investigates a Cu-Ni-Al alloyed medium carbon dual hardening steel. The precipitation sequence in this steel appears to be Cu-VC, despite a low alloying ratio of Cu/Ni and Cu/Al, with heterogeneous NiAl precipitation taking place at longer ageing times.

Table 3

Summary of Cu/Ni and Cu/Al ratios and reported sequences of precipitation in various publications.

at.% Cu/at.% Ni	at.% Cu/at.% Al	Sequence	Ref.
1.54	17.14	Cu ^a	[28]
0.46	0.95	Cu-NiAl	[29]
0.68	1.32	Cu-NiAl	[31]
0.46	0.94	Cu-NiAl	[26]
0.69	0.85	Cu-NiAl	[32]
1.93	5.24	Cu-NiAl	[36]
2.46	2.83	Cu ^a	[27]
0.28	0.32	NiAl-Cu	[33]
0.31	0.42	Cu-VC-NiAl	This study

^a Segregation of Ni, Al and Mn at Cu interfaces.

5. Conclusions

On the basis of DSC and APT analysis, the precipitation sequence during continuous ageing of a Cu-Ni-Al medium C alloyed dual hardening steel was decoded. The main findings summarize as follows:

- The DSC measurements revealed two overlapping exothermal peaks, which could successfully be attributed to phase separation, in the temperature range from 460 °C to 620 °C.
- Hardness measurements showed that continuous ageing with 20 K min⁻¹ does not lead to a secondary hardening increase. To reach improved hardness values, longer ageing at intermediate temperatures is needed.
- The RDF analysis shows C clustering after quenching within 5 s from 900 °C to room temperature. First signs of solute clustering were detected for Cu at a temperature of 360 °C.
- The detected clusters were Cu (Ni, Al, Mn) clusters, with Cu showing the highest amount of segregation. At an ageing temperature of 580 °C, these clusters reached a constant Ni and Al concentration. Further enrichments were only detected for Cu. At an ageing temperature of 580 °C, heterogeneous VC precipitation at the interfaces between the Cu clusters and the iron matrix occurred.
- Neither heterogeneous precipitation of NiAl particles nor the formation of a core-shell structure could be detected at the Cu cluster interfaces. The precipitation of NiAl is assumed to take place at longer ageing times.
- The precipitation sequence in the investigated dual hardening steel is Cu-VC-NiAl.

Declaration of competing interest

The authors declare that they have no known competing financial interests or personal relationships that could have appeared to influence the work reported in this paper.

Acknowledgements

Funding of the Austrian BMVIT (846933) in the framework of the program “Production of the future” and the “BMVIT Professorship for Industry” is gratefully acknowledged.

Data availability statement

The raw/processed data required to reproduce these findings cannot be shared at this time as the data also forms part of an ongoing study.

References

- [1] W.M. Garrison, M.S. Bhat, An approach to developing an alternative hot work die steel, *MTA* 19 (1988) 1751–1760, <https://doi.org/10.1007/BF02645143>.
- [2] H. Leitner, M. Bischof, H. Clemens, S. Erlach, B. Sonderegger, E. Kozeschnik, J. Svoboda, F.D. Fischer, Precipitation behaviour of a complex steel, *Adv. Eng. Mater.* 8 (2006) 1066–1077, <https://doi.org/10.1002/adem.200600165>.
- [3] S.D. Erlach, H. Leitner, M. Bischof, H. Clemens, F. Danoix, D. Lemarchand, I. Siller, Comparison of NiAl precipitation in a medium carbon secondary hardening steel and C-free PH13-8 maraging steel, *Mater. Sci. Eng. A* 429 (2006) 96–106, <https://doi.org/10.1016/j.msea.2006.05.071>.
- [4] V. Seetharaman, M. Sundararaman, R. Krishnan, Precipitation hardening in a PH 13-8 Mo stainless steel, *Mater. Sci. Eng. A* 47 (1981) 1–11, [https://doi.org/10.1016/0025-5416\(81\)90034-3](https://doi.org/10.1016/0025-5416(81)90034-3).
- [5] D.H. Ping, M. Ohnuma, Y. Hirakawa, Y. Kadoya, K. Hono, Microstructural evolution in 13Cr–8Ni–2.5Mo–2Al martensitic precipitation-hardened stainless steel, *Mater. Sci. Eng. A* 394 (2005) 285–295, <https://doi.org/10.1016/j.msea.2004.12.002>.
- [6] S.D. Erlach, *Precipitation Behaviour of Ni and Al Alloyed Hot-work Tool Steels and its Effects on Material Properties*, Dissertation Leoben, 2006.
- [7] F. Danoix, R. Danoix, J. Akre, A. Grellier, D. Delagnes, Atom probe tomography investigation of assisted precipitation of secondary hardening carbides in a medium carbon martensitic steels, *J. Microsc.* 244 (2011) 305–310, <https://doi.org/10.1111/j.1365-2818.2011.03537.x>.
- [8] R. Schnitzer, R. Hochfellner, M. Nöhner, M. Schober, H. Clemens, S. Zinner, H. Leitner, Mikrostrukturelle Charakterisierung von PH 13-8 Mo Maraging-Stählen, *PM* 46 (2009) 521–536, <https://doi.org/10.3139/147.110032>.
- [9] E. Povoden-Karadeniz, E. Kozeschnik, Simulation of precipitation kinetics and precipitation strengthening of B2-precipitates in martensitic PH 13–8 Mo steel, *ISIJ Int.* 52 (2012) 610–615, <https://doi.org/10.2355/isijinternational.52.610>.
- [10] R. Schnitzer, G.A. Zickler, E. Lach, H. Clemens, S. Zinner, T. Lippmann, H. Leitner, Influence of reverted austenite on static and dynamic mechanical properties of a PH 13-8 Mo maraging steel, *Mater. Sci. Eng. A* 527 (2010) 2065–2070, <https://doi.org/10.1016/j.msea.2009.11.046>.
- [11] H. Leitner, M. Schober, R. Schnitzer, Splitting phenomenon in the precipitation evolution in an Fe–Ni–Al–Ti–Cr stainless steel, *Acta Mater.* 58 (2010) 1261–1269, <https://doi.org/10.1016/j.actamat.2009.10.030>.
- [12] G.A. Roberts, G. Krauss, R. Kennedy, *Tool steels, fifth. ed.*, ASM International, Materials Park, OH, 2010.
- [13] M. Hofinger, M. Staudacher, M. Ognianov, C. Turk, H. Leitner, R. Schnitzer, Microstructural evolution of a dual hardening steel during heat treatment, *Micron* 120 (2019) 48–56, <https://doi.org/10.1016/j.micron.2019.02.004>.
- [14] M. Perrut, M.-H. Mathon, D. Delagnes, Small-angle neutron scattering of multiphase secondary hardening steels, *J. Mater. Sci.* 47 (2012) 1920–1929, <https://doi.org/10.1007/s10853-011-5982-x>.
- [15] D. Delagnes, F. Pettinari-Sturmell, M.H. Mathon, R. Danoix, F. Danoix, C. Bellot, P. Lamesle, A. Grellier, Cementite-free martensitic steels: a new route to develop high strength/high toughness grades by modifying the conventional precipitation sequence during tempering, *Acta Mater.* 60 (2012) 5877–5888, <https://doi.org/10.1016/j.actamat.2012.07.030>.
- [16] E. Kozeschnik, Thermodynamic prediction of the equilibrium chemical composition of critical nuclei, *Scr. Mater.* 59 (2008) 1018–1021, <https://doi.org/10.1016/j.scriptamat.2008.07.008>.
- [17] R. Monzen, M. Iguchi, M.L. Jenkins, Structural changes of 9R copper precipitates in an aged Fe–Cu alloy, *Philos. Mag. Lett.* 80 (2000) 137–148, <https://doi.org/10.1080/095008300176263>.
- [18] P. Warczok, D. Reith, M. Schober, H. Leitner, R. Podloucky, E. Kozeschnik, Investigation of Cu precipitation in bcc-Fe – comparison of numerical analysis with experiment, *JMR* 102 (2011) 709–716, <https://doi.org/10.3139/146.110524>.
- [19] P.J. Othen, M.L. Jenkins, G.D.W. Smith, W.J. Phythian, Transmission electron microscope investigations of the structure of copper precipitates in thermally-aged Fe–Cu and Fe–Cu–Ni, *Philos. Mag. Lett.* 64 (1991) 383–391, <https://doi.org/10.1080/09500839108215121>.
- [20] P.J. Othen, M.L. Jenkins, G.D.W. Smith, High-resolution electron microscopy studies of the structure of Cu precipitates in α -Fe, *Philosophical Magazine A* 70 (1994) 1–24, <https://doi.org/10.1080/01418619408242533>.
- [21] I. Holzer, E. Kozeschnik, Simulation of copper precipitation in Fe–Cu alloys, *Mater. Sci. Forum* 638–642 (2010) 2579–2584, <https://doi.org/10.4028/www.scientific.net/MSF.638-642.2579>.
- [22] B.L. Tiemens, A.K. Sachdev, R.K. Mishra, G.B. Olson, Three-dimensional (3-D) atom probe tomography of a Cu-precipitation-strengthened, ultrahigh-strength carburized steel, *Metall and Mat Trans A* 43 (2012) 3626–3635, <https://doi.org/10.1007/s11661-012-1178-5>.
- [23] S. Primig, G. Stechauner, E. Kozeschnik, Early stages of Cu precipitation in 15-5 PH maraging steel revisited – part I: experimental analysis, *Steel Research Int* 88 (2017) 1600084, <https://doi.org/10.1002/srin.201600084>.
- [24] G. Stechauner, S. Primig, E. Kozeschnik, Early stages of Cu precipitation in 15-5 PH maraging steel revisited – part II: thermokinetic simulation, *Steel Research Int* 88 (2017) 1600085, <https://doi.org/10.1002/srin.201600085>.
- [25] Z.B. Jiao, J.H. Luan, M.K. Miller, C.Y. Yu, C.T. Liu, Group precipitation and age hardening of nanostructured Fe-based alloys with ultra-high strengths, *Sci. Rep.* 6 (2016), <https://doi.org/10.1038/srep21364>.
- [26] S. Vaynman, D. Isheim, R. Prakash Kolli, S.P. Bhat, D.N. Seidman, M.E. Fine, High-strength low-carbon ferritic steel containing Cu–Fe–Ni–Al–Mn precipitates, *Metall and Mat Trans A* 39 (2008) 363–373, <https://doi.org/10.1007/s11661-007-9417-x>.
- [27] Z.B. Jiao, J.H. Luan, Z.W. Zhang, M.K. Miller, W.B. Ma, C.T. Liu, Synergistic effects of Cu and Ni on nanoscale precipitation and mechanical properties of high-strength steels, *Acta Mater.* 61 (2013) 5996–6005, <https://doi.org/10.1016/j.actamat.2013.06.040>.
- [28] D. Isheim, M.S. Gagliano, M.E. Fine, D.N. Seidman, Interfacial segregation at Curich precipitates in a high-strength low-carbon steel studied on a sub-nanometer scale, *Acta Mater.* 54 (2006) 841–849, <https://doi.org/10.1016/j.actamat.2005.10.023>.
- [29] D. Isheim, R.P. Kolli, M.E. Fine, D.N. Seidman, An atom-probe tomographic study of the temporal evolution of the nanostructure of Fe–Cu based high-strength low-carbon steels, *Scr. Mater.* 55 (2006) 35–40, <https://doi.org/10.1016/j.scriptamat.2006.02.040>.
- [30] K. Osamura, H. Okuda, K. Asano, M. Furusaka, K. Kishida, F. Kurosawa, R. Uemori, SANS study of phase decomposition in Fe–Cu alloy with Ni and Mn addition, *ISIJ Int.* 34 (1994) 346–354, <https://doi.org/10.2355/isijinternational.34.346>.
- [31] R. Prakash Kolli, D.N. Seidman, The temporal evolution of the decomposition of a concentrated multicomponent Fe–Cu-based steel, *Acta Mater.* 56 (2008) 2073–2088, <https://doi.org/10.1016/j.actamat.2007.12.044>.
- [32] M. Kapoor, D. Isheim, G. Ghosh, S. Vaynman, M.E. Fine, Y.-W. Chung, Aging characteristics and mechanical properties of 1600MPa body-centered cubic Cu and B2-NiAl precipitation-strengthened ferritic steel, *Acta Mater.* 73 (2014) 56–74, <https://doi.org/10.1016/j.actamat.2014.03.051>.
- [33] Z.B. Jiao, J.H. Luan, M.K. Miller, C.T. Liu, Precipitation mechanism and mechanical properties of an ultra-high strength steel hardened by nanoscale NiAl and Cu particles, *Acta Mater.* 97 (2015) 58–67, <https://doi.org/10.1016/j.actamat.2015.06.063>.
- [34] H. Leitner, R. Schnitzer, M. Schober, S. Zinner, Precipitate modification in PH13-8

- Mo type maraging steel, *Acta Mater.* 59 (2011) 5012–5022, <https://doi.org/10.1016/j.actamat.2011.04.053>.
- [35] M. Schober, R. Schnitzer, H. Leitner, Precipitation evolution in a Ti-free and Ti-containing stainless maraging steel, *Ultramicroscopy* 109 (2009) 553–562, <https://doi.org/10.1016/j.ultramic.2008.10.016>.
- [36] R.P. Kolli, Z. Mao, D.N. Seidman, D.T. Keane, Identification of a Ni_{0.5}(Al_{0.5} – xMnx) B2 phase at the heterophase interfaces of Cu-rich precipitates in an α -Fe matrix, *Appl. Phys. Lett.* 91 (2007) 241903, <https://doi.org/10.1063/1.2820378>.
- [37] W. Lefebvre-Ulrikson, F. Vurpillot, X. Sauvage (Eds.), *Atom Probe Tomography: Atom Probe Tomography: Put Theory into Practice*, Academic Press, London, 2016.
- [38] R.P. Kolli, D.N. Seidman, Comparison of compositional and morphological atom-probe tomography analyses for a multicomponent Fe-Cu steel, *Microsc. Microanal.* 13 (2007) 272–284, <https://doi.org/10.1017/S1431927607070675>.
- [39] A. Heinrich, T.a. Al-Kassab, R. Kirchheim, Investigation of the early stages of decomposition of Cu–0.7at.% Fe with the tomographic atom probe, *Mater. Sci. Eng. A* 353 (2003) 92–98, [https://doi.org/10.1016/S0921-5093\(02\)00673-1](https://doi.org/10.1016/S0921-5093(02)00673-1).
- [40] M.K. Miller, E.A. Kenik, Atom probe tomography: a technique for nanoscale characterization, *Microsc. Microanal.* 10 (2004) 336–341, <https://doi.org/10.1017/S1431927604040577>.
- [41] M.P. Moody, L.T. Stephenson, A.V. Ceguerra, S.P. Ringer, Quantitative binomial distribution analyses of nanoscale like-solute atom clustering and segregation in atom probe tomography data, *Microsc. Res. Tech.* 71 (2008) 542–550, <https://doi.org/10.1002/jemt.20582>.
- [42] C.K. Sudbrack, K. YOON, R. NOEBE, D.N. Seidman, Temporal evolution of the nanostructure and phase compositions in a model Ni–Al–Cr alloy, *Acta Mater.* 54 (2006) 3199–3210, <https://doi.org/10.1016/j.actamat.2006.03.015>.
- [43] F. de Geuser, W. Lefebvre, D. Blavette, 3D atom probe study of solute atoms clustering during natural ageing and pre-ageing of an Al-Mg-Si alloy, *Philos. Mag. Lett.* 86 (2006) 227–234, <https://doi.org/10.1080/09500830600643270>.
- [44] C.K. Sudbrack, R. Noebe, D.N. Seidman, Direct observations of nucleation in a nondilute multicomponent alloy, *Microsc. Microanal.* 73 (2006) 437, <https://doi.org/10.1103/PhysRevB.73.212101>.
- [45] Y. Dong, A. Etienne, A. Frolov, S. Fedotova, K. Fujii, K. Fukuya, C. Hatzoglou, E. Kuleshova, K. Lindgren, A. London, A. Lopez, S. Lozano-Perez, Y. Miyahara, Y. Nagai, K. Nishida, B. Radiguet, D.K. Schreiber, N. Soneda, M. Thuvander, T. Toyama, J. Wang, F. Sefta, P. Chou, E.A. Marquis, Atom probe tomography interlaboratory study on clustering analysis in experimental data using the maximum separation distance approach, *Microsc. Microanal.* (2019) 1–11, <https://doi.org/10.1017/S1431927618015581>.
- [46] L.T. Stephenson, M.P. Moody, P.V. Liddicoat, S.P. Ringer, New techniques for the analysis of fine-scaled clustering phenomena within atom probe tomography (APT) data, *Microsc. Microanal.* 13 (2007) 448–463, <https://doi.org/10.1017/S1431927607070900>.
- [47] J.R. de Laeter, J.K. Böhlke, P. de Bièvre, H. Hidaka, H.S. Peiser, K.J.R. Rosman, P.D.P. Taylor, Atomic weights of the elements. Review 2000, *Pure and Appl. Chem.* (2003) 683–800.
- [48] A.R. Waugh, E.D. Boyes, M.J. Southon, Investigations of field evaporation with a field-desorption microscope, *Surf. Sci.* 61 (1976) 109–142, [https://doi.org/10.1016/0039-6028\(76\)90411-8](https://doi.org/10.1016/0039-6028(76)90411-8).
- [49] F. Vurpillot, A. Bostel, D. Blavette, Trajectory overlaps and local magnification in three-dimensional atom probe, *Appl. Phys. Lett.* 76 (2000) 3127–3129, <https://doi.org/10.1063/1.126545>.
- [50] L.B. McCusker, R.B. von Dreele, D.E. Cox, D. Louër, P. Scardi, Rietveld refinement guidelines, *J. Appl. Crystallogr.* 32 (1999) 36–50, <https://doi.org/10.1107/S0021889898009856>.
- [51] M. Hofinger, M. Ognianov, C. Turk, H. Leitner, R. Schnitzer, Early stages of precipitate formation in a dual hardening steel, *HTM* 74 (2019) 293–301, <https://doi.org/10.3139/105.110390>.
- [52] S. Primig, H. Leitner, Transformation from continuous-to-isothermal aging applied on a maraging steel, *Mater. Sci. Eng. A* 527 (2010) 4399–4405, <https://doi.org/10.1016/j.msea.2010.03.084>.
- [53] Z.B. Jiao, J.H. Luan, W. Guo, J.D. Poplawsky, C.T. Liu, Effects of welding and post-weld heat treatments on nanoscale precipitation and mechanical properties of an ultra-high strength steel hardened by NiAl and Cu nanoparticles, *Acta Mater.* 120 (2016) 216–227, <https://doi.org/10.1016/j.actamat.2016.08.066>.
- [54] R. Hamano, The effect of the precipitation of coherent and incoherent precipitates on the ductility and toughness of high-strength steel, *MTA* 24 (1993) 127–139, <https://doi.org/10.1007/BF02669610>.